Distribution Agreement

In presenting this thesis or dissertation as a partial fulfillment of the requirements for an advanced degree from Emory University, I hereby grant to Emory University and its agents the non-exclusive license to archive, make accessible, and display my thesis or dissertation in whole or in part in all forms of media, now or hereafter known, including display on the world wide web. I understand that I may select some access restrictions as part of the online submission of this thesis or dissertation. I retain all ownership rights to the copyright of the thesis or dissertation. I also retain the right to use in future works (such as articles or books) all or part of this thesis or dissertation.

Signature:

_____ _____

Sara T. Gebre Date

Effect of Interfacial Interactions on Charge Transfer in QD-Molecular Catalyst Complexes

By

Sara T. Gebre

Doctor of Philosophy
Chemistry

Dr. Tianquan Lian
Advisor

Dr. R. Brian Dyer
Committee Member

Dr. Craig H. Hill
Committee Member

Accepted:

Kimberly Jacob Arriola, Ph.D, MPH
Dean of the James T. Laney School of Graduate Studies

Date

Effect of Interfacial Interactions on Charge Transfer in QD-Molecular Catalyst Complexes

By

Sara T. Gebre
B.S. Haverford College, Haverford, PA, USA, 2016

Advisor: Dr. Tianquan Lian, Ph.D.

An abstract of
A dissertation submitted to the Faculty
of the James T. Laney School of
Graduate Studies of Emory University
in partial fulfillment of the requirements for the degree of
Doctor of Philosophy in Chemistry
2023

Abstract

Effect of Interfacial Interactions on Charge Transfer in QD-Molecular Catalyst Complexes

By Sara T. Gebre

Over the past few decades, the use of fossil fuels has generated greenhouse gases, resulting in increasing deleterious effects on our environment. Recently, research for alternative fuels has increased and has demonstrated positive advances towards processes such as artificial photosynthesis, CO_2 reduction, and water splitting. Photocatalysis for the purpose of converting to these greener fuels is one of the main methods by which the products of these processes are achieved. Many types of materials can be used for this goal, particularly semiconductor nanomaterials and molecular catalysts. Fortunately, semiconductor nanocrystals (NCs), quantum dots (QDs) in particular, have several advantages, making them good materials for photocatalysis. They are efficient light harvesters, size tunable, and their surface chemistry can be manipulated towards improving the performance of the nanocrystal. The surface chemistry (ligands, etc) of QDs can control nanocrystal growth, solvent solubility, and electronic passivation, which dictate charge transfer properties in the NC. This work investigates how different molecules bound to the QD surface affect electron transfer processes with the purpose of CO_2 reduction with a molecular catalyst. The first project details how electron transfer from a Cd_3P_2 QD to a molecular catalyst, *fac*-Re(4,4'-R_2-bpy)$(CO)_3$Cl (bpy=bipyridine; R=COOH) (ReC0A), is changed upon the addition of a hole scavenger, triethylamine (TEA). ReC0A is highly selective and efficient for catalyzing CO_2 reduction under only 400 nm excitation. By using a Cd_3P_2 QD, which can absorb into the near IR, and reducing the ReC0A catalyst, we can extend the range over which CO_2 reduction can occur. The second project describes the Fano resonance (FR) coupling phenomenon that occurs between CdSe QD intraband transitions and ReC0A CO modes as a function of catalyst concentration and QD size. The third work demonstrates the effect of distance on FR coupling using ReCxA catalysts with different chain length linkers and core/shell CdSe/ZnS QDs. Finally, the last project is a collaboration with Hong Kong City University that investigates hot electron transfer in Ag-CdSe heterostructures resulting in high quantum yield. This thesis work demonstrates charge transfer dynamics in NC-molecular catalyst complexes upon ultrafast laser excitation for the application of CO_2 reduction and photocatalysis.

Effect of Interfacial Interactions on Charge Transfer in QD-Molecular Catalyst Complexes

By

Sara T. Gebre
B.S. Haverford College, PA, USA, 2016

Advisor: Tianquan Lian, Ph.D.

A dissertation submitted to the Faculty of the
James T. Laney School of Graduate Studies of Emory University
in partial fulfillment of the requirements for the degree of
Doctor of Philosophy
in Chemistry
2023

Acknowledgements

First, I would like to thank my advisor, Dr. Tianquan Lian, for his support, mentorship, and help throughout my Ph.D. His guidance through the years has molded me into a better scientist and his advice has been invaluable. I would also like to thank the rest of my committee, Dr. Craig Hill and Dr. Brian Dyer for their comments, insights, and encouragement throughout my time here.

I would also like to thank my labmates; Drs. Zed Xu and Jia Song for teaching me how to use the transient absorption setups and Drs. Yawei Liu and Tao Jin for teaching me how to make quantum dots and their discussions with me about my research. I'd like to thank Dr. Laura Kiefer for working with me on the Cd_3P_2-ReC0A project, teaching me about safe laser lab practices, and being a great friend. I would also like to thank the other postdocs in my lab, Dr. Wenxing Yang for his help with the Fano resonance project, his mentorship and friendship, Dr. Nandan Ghorai for always being willing to edit my drafts, giving me career advice, and being a fun person to be around, and Dr. Shengxiang (Joey) Wu, for always being a bright person and for all his help and friendship as well. I'm also grateful for all the rest of my labmates for being great friends, for all our adventures together, and for all the great food they introduced me to: Jinhui Meng, Fengyi Zhao, Sa Suo, Paul Jin, Sheng He, Dr. Brian Breeman, Qiliang Liu, Isaac Tangen, Zhicheng Yang, Dr. Aimin Ge, Dr. Dhritiman Bhattacharya, Dr. Lu Lin, Dr. Qiuyang Li, Dr. Qiongyi Shang, Qiaoli Chen, Yulei Cao, Yawei Yang, Xu Guo, Natalie Uhlikova, Giorgi Petriashvili, Chuchu Qiu, Yiwei Yang, and Bo Dong. I'm especially appreciative of my friends outside the lab, David White, Torie Snider, Yasha Duggal, Anthony Sementelli, Christella Gordon, Youngsun Kim, Ayda Gonzalez, and my old roommates, Ninju and Keethu Kasi for always being willing to listen to me rant about things that were stressful for me and for all the fun times we've had together.

Finally, I would like to thank my family and people in PA for their support: all my cousins, my uncle, and everyone at church for being supportive and encouraging, along with my brother and sister for brightening my day or distracting me from work whenever I was home. Most of all I would like my parents: my mom for her constant encouragement and my dad for being my role model for my education and encouraging me to pursue chemistry.

Table of Contents

List of Figures

List of Tables

List of Abbreviations

BF	bright field
CB	conduction band
CMOS	complementary metal-oxide semiconductor
CSS	charge separated state
CV	cyclic voltammetry
DFT	density functional theory
DOS	density of states
DOSY	diffusion ordered spectroscopy
EVET	electronic-to-vibrational energy transfer
FR	Fano resonance
FTIR	Fourier transform infrared spectroscopy
HAADF-STEM	high angular annular dark field- scanning transmission electron microscopy
HRTEM	high resolution transmission electron microscopy
HSE	Heyd-Scuseria-Ernzerhof
IR	infrared
IRF	instrument response function
LSPR	localized surface plasmon resonance
MCT	mercury cadmium telluride
MeCN	acetonitrile
ML	monolayer
MLCT	metal-to-ligand charge transfer

MOF	metal organic framework
MP	Monckhorst-Pack
$[MV]^{2+}$	methyl viologen
NC	nanocrystal
NM	nanomaterial
NMR	nuclear magnetic resonance
NP	nanoparticle
NR	nanorod
OA	oleic acid
OD	optical density
ODA	octadecylamine
ODE	octadecene
ODPA	octadecylphosphonic acid
OPA	optical parametric amplifier
PAW	project augmented wave
PBE	Perdew-Burke-Ernzerhof
PHET	plasmon induced hot electron transfer
PL	photoluminescence
QD	quantum dot
QE	quantum efficiency
QY	quantum yield
ReC0A	*fac*-Re(bpy-COOH)$(CO)_3$Cl
ReCl	*fac*-Re(bpy)$(CO)_3$Cl
ReS_2	[Re(SS-bpy)$(CO)_3$Cl]

SC	semiconductor
SILAR	successive ion layer adsorption reaction
TA	transient absorption spectroscopy
$TBAPF_6$	tetrabutylammonium hexafluorophosphate
TCSPC	time correlated single photon counting
TEA	triethylamine
$TEAH^+$	triethylammonium
TEM	transmission electron microscopy
TEOA	triethanolamine
TiO_2	Titanium dioxide
TOP	triocylphosphine
TOPO	trioctylphosphine oxide
TRIR	time resolved infrared spectroscopy
VASP	Vienna Ab initio Simulation Packages
VB	valence band
WLC	white light continuum
XB	exciton bleach

Chapter 1. Introduction

1.1 Background and Motivation

Over the past century, greenhouse gas emissions have drastically increased with severe environmental consequences, namely global warming. The onset of the Industrial Revolution during the mid-1700s marked a pivotal moment in history when the utilization of fossil fuels, notably coal and natural gas, became indispensable for driving technological progress. This era witnessed the advent of transformative innovations, such as the steam engine and textile industry, which played a fundamental role in propelling society into a new era of industrialization and advancement. Since the first recording in 1880, the global temperature has increased about 1 ^{o}C, causing increasing heat waves, glaciers melting, and rising sea levels.[1] The greenhouse gas present in the highest concentration is CO_2, which has increased about 90% since 1970.[2] There has been a conscious effort to reduce CO_2 in the atmosphere, resulting in a variety of different approaches to this problem including the use of semiconductors (SCs) and molecular catalysts.

SCs have garnered significant attention and shown immense promise as materials capable of addressing the challenge of reducing CO_2 emissions. Their unique electronic properties and the ability to facilitate various photochemical and photocatalytic processes make them essential players in the pursuit of sustainable solutions for carbon dioxide reduction and environmental remediation.[3-6] They have a band structure that consists of a valence band (VB) and conduction band (CB) whose positions determine the width of the band gap which dictates the material's optical properties.[7] For CO2 reduction purposes, it's essential that the CB position exhibits a sufficiently negative potential to enable the transfer of electrons to the reactant adsorbed on the nanoparticle (NP) surface. To reduce CO_2, at least two electrons and two protons are needed, and the reduction potentials are

different depending on which product will be formed, e.g. CO, methane, formate, etc.[8] Because of this, hole scavengers or other species must be present to replenish an electron to the VB to prevent the products of the reaction from being consumed.[7] In addition, the SC must be able to efficiently separate charges to prevent recombination before the reaction can take place. Titanium dioxide (TiO_2) NPs have garnered extensive research interest due to their stability and low toxicity. Nevertheless, TiO_2 possesses a substantial band gap, which is suboptimal for photocatalytic reduction reactions. Therefore, in addition to surface engineering to improve its photocatalytic ability, doping the NPs[9-12] or using them in conjunction with another SC[10, 13] are alternative methods to further improve the efficiency of CO_2 reduction. For example, oftentimes TiO_2 is used with metal NPs to extract the charge carriers. One study demonstrated that upon UV excitation of Au/Pt/TiO_2 nanofibers, there was a large enhancement in H_2 production and CO_2 reduction due to the surface plasmon resonance (SPR) effect of the Au and the ability of Pt to prevent fast charge recombination in the TiO_2.[7, 13]

Chalcogenide SCs have also been used in conjunction with other nanomaterials (NMs) and catalysts to reduce CO_2 or generate H_2. For example, CdS and a metal organic framework (MOF) Co-ZIF-9 has been used with CdS as a cocatalyst, while CdS acted as the photocatalyst, due to its efficient light harvesting ability.[14] Chalcogenide heterostructures have also been used with proteins for this purpose. White *et al.* used CdSe/CdS shelled nanorods in conjunction with a carbon monoxide dehydrogenase, [NiFe] CODH II, and achieved a quantum yield (QY) of up to 19%.[15] In addition, CdS nanorods have also been shown to generate H_2 with [FeFe] hydrogenase[16] and have also been used for water reduction with Pt NPs[17], demonstrating the wide range of uses of chalcogenide NMs in photocatalytic applications.

Molecular catalysts are yet another area where there has been significant work in attempting and succeeding at achieving CO_2 reduction.[18-20] Many of these catalysts have transition metal centers

where the reaction occurs and can be used photocatalytically[21] and/or electrochemically[22]. These include cyclam, porphyrin (macrocyclics), bipyridine, and phosphine ligand-based catalysts.[8] For example, electrochemically, Ni-cyclam[22-23] was found to have a CO faradaic efficiency of 96%[24] while $Rh(dppe)_2(Cl)$ (dppe: 1,2-bis(diphenylphosphino)ethane) were able to form formate from CO_2 with current efficiencies between 22 and 42%[25]. In addition, Fe porphyrins were shown to reduce CO_2 to CO in the presence of Mg^+ or weak Bronsted acids while retaining their stability (porphyrins alone would degrade).[8, 26-27] There are many other molecular catalysts with transition metal centers that include Co, Re, Ru, Pd, Ir, W, and Mn.[18, 28] From here, we focus on a specific Re based molecular catalyst.

One of the most popular catalysts and one that is used throughout this dissertation, is the rhenium based tricarbonyl bipyridyl catalysts ($Re(bpy)(CO)_3X$).[19-20, 28-29] This type of molecular complex, first synthesized by Lehn *et al.*[29], can catalyze CO_2 reduction and H_2 production, however, it is almost exclusively selective towards CO_2 reduction, with 98% current efficiency electrochemically. These complexes are also photocatalysts. They generally have a metal-to-ligand charge transfer (MLCT) state centered around 400 nm with the π to π^* transition of the bipyridine group in the UV region (~310 nm).[21] While this catalyst is also electrochemically active, we will only discuss the photocatalytic pathway as is pertinent to this dissertation. The photocatalysis of this complex has been reproduced in Figure 1.1 with three possible products: $HCOO^-$, CO, and HCO_3^-.

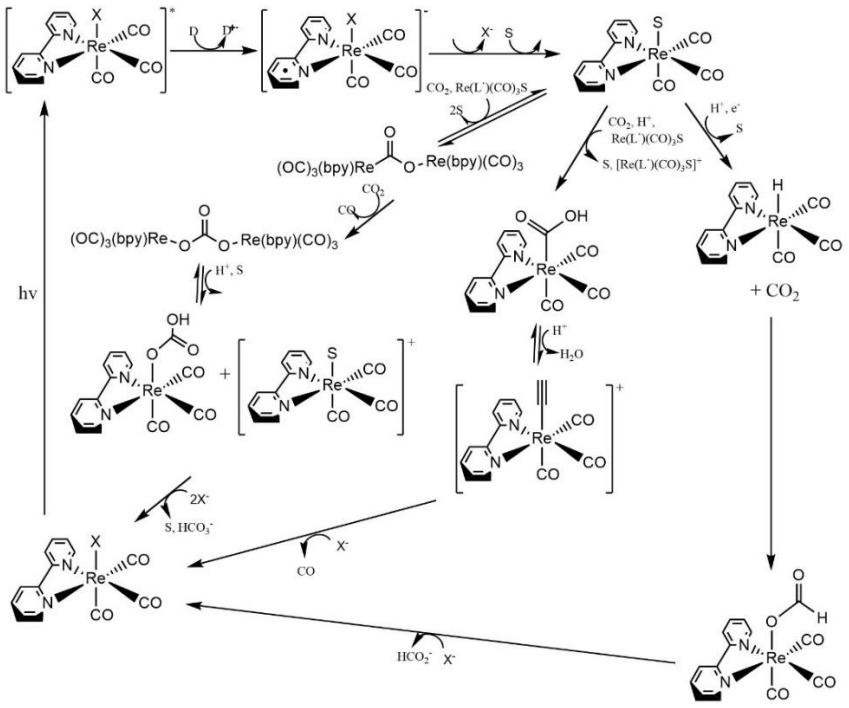

Figure 1.1. Proposed photocatalytic mechanism of the rhenium catalyst reducing CO_2 (D: donor, X: coordinated halide (Cl, Br, I), S: solvent).[18] Adapted with permission from Ref 18. Copyright {2009} American Chemical Society.

When the $Re(bpy)(CO)_3X$ is directly excited with 400 nm light, a MLCT state is formed, leading to the bipyridine anion radical. A sacrificial electron donor reduces the excited complex, and the chloride ligand dissociates, allowing for a solvent molecule to coordinate to the rhenium metal center. From the $[Re(bpy)(CO)_3S]^-$ state (S=solvent), there are three distinct CO_2 -coordinating pathways: forming a CO_2 bridged $[Re(bpy)(CO)_3]$ dimer, coordination of the CO_2 through bonding of the CO_2 carbon, or coordination through the CO_2 oxygen. Each of these yield various reduction products with fairly high efficiency and regenerates the original $Re(bpy)(CO)_3X$ complex. Due to this catalyst's high efficiency, selectivity for CO_2 reduction, and distinct infrared absorptions, we use this complex throughout this dissertation. Since the MLCT state can only be generated under 400 nm excitation, we aim to extend its catalytic activity across the entire visible spectrum using quantum

dots (QDs), which we discuss in the next section.

1.2 Quantum Dots and Their Surface Composition

SC nanocrystals (NCs) have become widely used for various applications some of which include solar fuel generation[30-34], lasing[35-40], and use in light emitting diodes[41-44]. In particular, QDs have been widely studied and are particularly useful due to their size tunability (band gap engineering), broad absorption in the visible spectrum, and the ability to tune their morphology.[45-47] QDs are NPs smaller than its Bohr radius, having unique optical and electronic properties different than the bulk materials. In comparison to bulk materials, the small size of these particles results in the formation of discrete energy levels within the valence (ground state) and conduction (excited state) bands due to quantum confinement of the particle. Their optical properties can be tuned by changing the size of the particle, changing the surface of the quantum dots, and by doping the particles. Their manipulation allows for their applicability in several technological areas including bioimaging and photovoltaic devices.[32]

The surface chemistry of QDs plays a significant role in the performance of the nanomaterial. This is mainly dictated by the ligands on the QD surface.[48] These ligands can affect solubility of the QDs in different solvents, play an important role in relaxation of excited nanoparticles, as well as control nanocrystal growth.[48-49] In addition to this, there can be surface trap states that are generated due to undercoordination of the surface atoms because of steric hindrance of the native ligands.[50] Trap states are often detrimental to the lifetime of a charge separated state (CSS) within the nanomaterial because they generate mid gap states which then create a competing nonradiative relaxation pathway and results in a shorter-lived CSS. To remedy this, the surfaces of these materials are passivated, oftentimes by the growth of a shell around the core nanocrystal or by

using different surface ligands through ligand exchange, which can extend the exciton lifetime.[51-52] There are mainly three different types of ligands: L-type, X-type, and Z-type, labeled for the number of electrons that can be donated to the nanocrystal structure (two, one, or none, respectively).[53] Examples of each ligand type include amines (L-type), carboxylates and thiolates (X-type), and Cd-oleate (Z-type). Depending on the surface chemistry, exciton relaxation can proceed through Auger recombination, electron phonon coupling, and electronic to vibrational energy transfer (EVET) through ligand vibrations, all which are nonradiative.[48, 54] Electron and hole trapping and radiative recombination also compete with nonradiative relaxation. Some surface ligands, such as oleic acid, have high frequency IR modes (carboxylate) that can be directly probed with NIR, as Leger et al has done with 1.3 nm InP QDs.[55] Inorganic ligands have also been shown to affect vibrational relaxation pathways associated with the electronic excited state of the nanoparticle through acoustic phonon damping.[56] In addition to these, there has been a wide array of studies investigating the importance of QD surfaces for various applications and this thesis aims to add to the current understanding of QD interfacial interactions.

In this dissertation, while attempting to achieve CO_2 reduction with various chalcogenide QDs and the *fac*-Re(bpy-COOH)$(CO)_3$Cl (ReC0A) catalyst and some of its variations, we have revealed several interesting interactions between triethylamine and the QDs, as well as the Re complex and QD surfaces. We systematically investigate these interfacial interactions (surface binding, electron donation, and electronic vibrational (Fano) coupling) and their implications on the application of QD-molecular catalyst complexes in CO_2 reduction. These types of interactions have the potential to and do affect the QD's optical properties as we demonstrate in Chapters 3-5. These studies highlight the importance of QD surface chemistry and how it might affect QD performance in several different applications, most specifically photocatalysis.

1.3 Effect of Surface on Plasmon Induced Hot Electron Transfer in Plasmonic Nanomaterials

Plasmonic NMs have been extensively studied for use in photovoltaics[57-58], photodetectors[59-60], and photocatalysis[58, 61-62]. Usually, these NMs are metal nanoparticles (NPs) which have large absorption cross sections and localized surface plasmon resonances (LSPR) that can enhance the degree of light that can be absorbed.[61] Oftentimes, plasmonic metal NPs are used in conjunction with semiconductors, some of which include TiO_2 and chalcogenides like CdS or CdSe.[63-66] For example, Mubeen *et al.* fabricated a solar water splitting device using gold (Au) nanoarrays; one side capped with TiO_2 and Pt NPs grown on the semiconductor, and the other with a Co oxygen evolution catalyst.[67] They were able to simultaneously use hot electrons and hot holes from the plasmon excitation to serve two different purposes. When immersed in water and excited, hot electrons were injected into TiO_2 and transferred to Pt, which acted as the reaction site for producing H_2, while hot holes were transferred to the Co catalyst to generate O_2. Yet another case involves Ag-TiO_2 films, where after LSPR excitation, hot electrons were transferred with a quantum efficiency (QE) of up to 53% depending on Ag NP size.[68] This type of efficient electron extraction can be very useful for photovoltaic devices.

This type of electron extraction depends on the LSPRs of the NPs. Plasmons are collective oscillations of free charge carriers within a metal NP.[62] Upon excitation of the LSPR band, hot carriers are generated, which can then be transferred into the semiconductor. This process is called plasmon induced hot electron transfer (PHET) and usually occurs on the order of femtoseconds. There have been several studies investigating PHET as the timescale on which hot electron generation and transfer is important for application in different devices. It is essential for electron injection to occur before charge recombination[58], otherwise the efficiency of the heterostructure in

photovoltaics and photocatalysis would suffer greatly.

The size and morphology of plasmonic NPs and the metal-semiconductor interface also greatly affects charge carrier behavior.[69-70] As described previously, in a Ag size dependent study, Song *et al.* observed an increase in PHET from 28% to 53% when decreasing NP size from 5.9 to 1.7 nm.[68] In addition, different shapes of plasmonic nanomaterials will affect the position of the LSPR and change the charge carrier transfer efficiency. For example, Au nanorods (NRs) on single crystal TiO_2 exhibit two characteristic bands instead of one LSPR absorption seen in spherical NPs.[64] The metal semiconductor heterostructure interface can also affect charge injection efficiencies. Yuan *et al.* were able to monitor the Au-TiO_2 interface for CO oxidation using *in situ* environmental transmission electron microscopy and, by changing gas and temperature conditions, were able to observe an epitaxial rotation of the Au during the reaction.[71] In addition, it has been demonstrated that with TiO_2 epitaxially grown on Au nanostars and under near-IR excitation, Atta *et al.* were able to enhance the photocatalytic activity of H_2 production when increasing the crystallinity of TiO_2.[72] This demonstrates the importance of the metal-SC interface for photocatalysis.

In Chapter 6 of this dissertation, in collaboration with Dr. Zhang's group at Hong Kong City University, we investigate PHET in epitaxially grown Ag-CdS an Ag-CdSe nano-heterostructures using ultrafast spectroscopy. These heterostructures were synthesized by our collaborators and had a lattice mismatch of 40%, incredibly high in comparison to typical epitaxial heterostructures and using ultrafast spectroscopy, under excitation of the LSPR we achieved an electron injection QY of 18.1%.

1.4 References

1. World of Change: Global Temperatures. https://earthobservatory.nasa.gov/world-of-change/global-temperatures (accessed October 2).
2. Global Greenhouse Gas Emissions Data. https://www.epa.gov/ghgemissions/global-greenhouse-gas-emissions-data#Reference%201 (accessed October 2).
3. Marszewski, M.; Cao, S.; Yu, J.; Jaroniec, M., Semiconductor-based photocatalytic CO2 conversion. *Materials Horizons* **2015,** *2* (3), 261-278.
4. Park, Y. H.; Murali, G.; Modigunta, J. K. R.; In, I.; In, S.-I., Recent Advances in Quantum Dots for Photocatalytic CO2 Reduction: A Mini-Review. *Frontiers in Chemistry* **2021,** *9*.
5. Li, H.; Cheng, C.; Yang, Z.; Wei, J., Encapsulated CdSe/CdS nanorods in double-shelled porous nanocomposites for efficient photocatalytic CO2 reduction. *Nature Communications* **2022,** *13* (1), 6466.
6. Arcudi, F.; Đorđević, L.; Nagasing, B.; Stupp, S. I.; Weiss, E. A., Quantum Dot-Sensitized Photoreduction of CO2 in Water with Turnover Number > 80,000. *Journal of the American Chemical Society* **2021,** *143* (43), 18131-18138.
7. Li, K.; Peng, B.; Peng, T., Recent Advances in Heterogeneous Photocatalytic CO2 Conversion to Solar Fuels. *ACS Catalysis* **2016,** *6* (11), 7485-7527.
8. Benson, E. E.; Kubiak, C. P.; Sathrum, A. J.; Smieja, J. M., Electrocatalytic and homogeneous approaches to conversion of CO2 to liquid fuels. *Chemical Society Reviews* **2009,** *38* (1), 89-99.
9. Li, K.; An, X.; Park, K. H.; Khraisheh, M.; Tang, J., A critical review of CO2 photoconversion: Catalysts and reactors. *Catalysis Today* **2014,** *224*, 3-12.
10. Ma, Y.; Wang, X.; Jia, Y.; Chen, X.; Han, H.; Li, C., Titanium Dioxide-Based Nanomaterials for Photocatalytic Fuel Generations. *Chemical Reviews* **2014,** *114* (19), 9987-10043.
11. Das, S.; Wan Daud, W. M. A., A review on advances in photocatalysts towards CO2 conversion. *RSC Advances* **2014,** *4* (40), 20856-20893.
12. Yui, T.; Kan, A.; Saitoh, C.; Koike, K.; Ibusuki, T.; Ishitani, O., Photochemical Reduction of CO2 Using TiO2: Effects of Organic Adsorbates on TiO2 and Deposition of Pd onto TiO2. *ACS Applied Materials & Interfaces* **2011,** *3* (7), 2594-2600.
13. Zhang, Z.; Wang, Z.; Cao, S.-W.; Xue, C., Au/Pt Nanoparticle-Decorated TiO2 Nanofibers with Plasmon-Enhanced Photocatalytic Activities for Solar-to-Fuel Conversion. *The Journal of Physical Chemistry C* **2013,** *117* (49), 25939-25947.
14. Wang, S.; Wang, X., Photocatalytic CO2 reduction by CdS promoted with a zeolitic imidazolate framework. *Applied Catalysis B: Environmental* **2015,** *162*, 494-500.
15. White, D. W.; Esckilsen, D.; Lee, S. K.; Ragsdale, S. W.; Dyer, R. B., Efficient, Light-Driven Reduction of CO2 to CO by a Carbon Monoxide Dehydrogenase–CdSe/CdS Nanorod Photosystem. *The Journal of Physical Chemistry Letters* **2022,** *13* (24), 5553-5556.
16. Wilker, M. B.; Shinopoulos, K. E.; Brown, K. A.; Mulder, D. W.; King, P. W.; Dukovic, G., Electron Transfer Kinetics in CdS Nanorod–[FeFe]-Hydrogenase Complexes and Implications for Photochemical H2 Generation. *Journal of the American Chemical Society* **2014,** *136* (11), 4316-4324.
17. Liu, Y.; Yang, W.; Chen, Q.; Cullen, D. A.; Xie, Z.; Lian, T., Pt Particle Size Affects Both the Charge Separation and Water Reduction Efficiencies of CdS–Pt Nanorod Photocatalysts for Light Driven H2 Generation. *Journal of the American Chemical Society* **2022,** *144* (6), 2705-2715.
18. Morris, A. J.; Meyer, G. J.; Fujita, E., Molecular Approaches to the Photocatalytic Reduction of Carbon Dioxide for Solar Fuels. *Accounts of Chemical Research* **2009,** *42* (12), 1983-1994.

19. Grills, D. C.; Fujita, E., New Directions for the Photocatalytic Reduction of CO2: Supramolecular, scCO2 or Biphasic Ionic Liquid−scCO2 Systems. *The Journal of Physical Chemistry Letters* **2010,** *1* (18), 2709-2718.
20. Grice, K. A.; Kubiak, C. P., Chapter Five - Recent Studies of Rhenium and Manganese Bipyridine Carbonyl Catalysts for the Electrochemical Reduction of CO2. In *Advances in Inorganic Chemistry*, Aresta, M.; van Eldik, R., Eds. Academic Press: 2014; Vol. 66, pp 163-188.
21. Takeda, H.; Koike, K.; Morimoto, T.; Inumaru, H.; Ishitani, O., Photochemistry and photocatalysis of rhenium(I) diimine complexes. In *Advances in Inorganic Chemistry*, Eldik, R. v.; Stochel, G., Eds. Academic Press: 2011; Vol. 63, pp 137-186.
22. Beley, M.; Collin, J. P.; Ruppert, R.; Sauvage, J. P., Electrocatalytic reduction of carbon dioxide by nickel cyclam2+ in water: study of the factors affecting the efficiency and the selectivity of the process. *Journal of the American Chemical Society* **1986,** *108* (24), 7461-7467.
23. Collin, J. P.; Jouaiti, A.; Sauvage, J. P., Electrocatalytic properties of (tetraazacyclotetradecane)nickel(2+) and Ni2(biscyclam)4+ with respect to carbon dioxide and water reduction. *Inorganic Chemistry* **1988,** *27* (11), 1986-1990.
24. Beley, M.; Collin, J.-P.; Ruppert, R.; Sauvage, J.-P., Nickel(II)-cyclam: an extremely selective electrocatalyst for reduction of CO2 in water. *Journal of the Chemical Society, Chemical Communications* **1984,** (19), 1315-1316.
25. Slater, S.; Wagenknecht, J. H., Electrochemical reduction of carbon dioxide catalyzed by Rh(diphos)2Cl. *Journal of the American Chemical Society* **1984,** *106* (18), 5367-5368.
26. Bhugun, I.; Lexa, D.; Savéant, J.-M., Catalysis of the Electrochemical Reduction of Carbon Dioxide by Iron(0) Porphyrins: Synergystic Effect of Weak Brönsted Acids. *Journal of the American Chemical Society* **1996,** *118* (7), 1769-1776.
27. Hammouche, M.; Lexa, D.; Momenteau, M.; Saveant, J. M., Chemical catalysis of electrochemical reactions. Homogeneous catalysis of the electrochemical reduction of carbon dioxide by iron("0") porphyrins. Role of the addition of magnesium cations. *Journal of the American Chemical Society* **1991,** *113* (22), 8455-8466.
28. Apaydin, D. H.; Schlager, S.; Portenkirchner, E.; Sariciftci, N. S., Organic, Organometallic and Bioorganic Catalysts for Electrochemical Reduction of CO2. *ChemPhysChem* **2017,** *18* (22), 3094-3116.
29. Hawecker, J.; Lehn, J.-M.; Ziessel, R., Electrocatalytic reduction of carbon dioxide mediated by Re(bipy)(CO)3Cl (bipy = 2,2'-bipyridine). *Journal of the Chemical Society, Chemical Communications* **1984,** (6), 328-330.
30. Kamat, P. V., Quantum Dot Solar Cells. Semiconductor Nanocrystals as Light Harvesters. *The Journal of Physical Chemistry C* **2008,** *112* (48), 18737-18753.
31. Wu, K.; Lian, T., Quantum confined colloidal nanorod heterostructures for solar-to-fuel conversion. *Chemical Society Reviews* **2016,** *45* (14), 3781-3810.
32. Pietryga, J. M.; Park, Y.-S.; Lim, J.; Fidler, A. F.; Bae, W. K.; Brovelli, S.; Klimov, V. I., Spectroscopic and Device Aspects of Nanocrystal Quantum Dots. *Chemical Reviews* **2016,** *116* (18), 10513-10622.
33. Li, Q.; Zhao, F.; Qu, C.; Shang, Q.; Xu, Z.; Yu, L.; McBride, J. R.; Lian, T., Two-Dimensional Morphology Enhances Light-Driven H2 Generation Efficiency in CdS Nanoplatelet-Pt Heterostructures. *Journal of the American Chemical Society* **2018,** *140* (37), 11726-11734.
34. Wang, C., Chapter 9 - Quantum Dots for Visible-Light Photocatalytic CO2 Reduction. In *Novel Materials for Carbon Dioxide Mitigation Technology*, Shi, F.; Morreale, B., Eds. Elsevier: Amsterdam, 2015; pp 269-295.
35. Zhou, C.; M. Pina, J.; Zhu, T.; H. Parmar, D.; Chang, H.; Yu, J.; Yuan, F.; Bappi, G.; Hou, Y.; Zheng, X.; Abed, J.; Chen, H.; Zhang, J.; Gao, Y.; Chen, B.; Wang, Y.-K.; Chen, H.; Zhang, T.;

Hoogland, S.; Saidaminov, M. I.; Sun, L.; Bakr, O. M.; Dong, H.; Zhang, L.; H. Sargent, E., Quantum Dot Self-Assembly Enables Low-Threshold Lasing. *Advanced Science* **2021,** *8* (20), 2101125.
36. Lim, J.; Park, Y.-S.; Klimov, V. I., Optical gain in colloidal quantum dots achieved with direct-current electrical pumping. *Nature Materials* **2018,** *17* (1), 42-49.
37. Hsieh, Y.-H.; Hsu, B.-W.; Peng, K.-N.; Lee, K.-W.; Chu, C. W.; Chang, S.-W.; Lin, H.-W.; Yen, T.-J.; Lu, Y.-J., Perovskite Quantum Dot Lasing in a Gap-Plasmon Nanocavity with Ultralow Threshold. *ACS Nano* **2020,** *14* (9), 11670-11676.
38. Jung, H.; Ahn, N.; Klimov, V. I., Prospects and challenges of colloidal quantum dot laser diodes. *Nature Photonics* **2021,** *15* (9), 643-655.
39. Guan, J.; Sagar, L. K.; Li, R.; Wang, D.; Bappi, G.; Wang, W.; Watkins, N.; Bourgeois, M. R.; Levina, L.; Fan, F.; Hoogland, S.; Voznyy, O.; de Pina, J. M.; Schaller, R. D.; Schatz, G. C.; Sargent, E. H.; Odom, T. W., Quantum Dot-Plasmon Lasing with Controlled Polarization Patterns. *ACS Nano* **2020,** *14* (3), 3426-3433.
40. Whitworth, G. L.; Dalmases, M.; Taghipour, N.; Konstantatos, G., Solution-processed PbS quantum dot infrared laser with room-temperature tunable emission in the optical telecommunications window. *Nature Photonics* **2021,** *15* (10), 738-742.
41. Chen, H.-C.; Shabir, A.; Tan, C. M.; Singh, P.; Lin, J.-H., Degradation dynamics of quantum dots in white LED applications. *Scientific Reports* **2021,** *11* (1), 24153.
42. Shirasaki, Y.; Supran, G. J.; Bawendi, M. G.; Bulović, V., Emergence of colloidal quantum-dot light-emitting technologies. *Nature Photonics* **2013,** *7* (1), 13-23.
43. Onal, A.; Eren, G. O.; Sadeghi, S.; Melikov, R.; Han, M.; Karatum, O.; Ozer, M. S.; Bahmani Jalali, H.; Dogru-Yuksel, I. B.; Yilgor, I.; Metin, Ö.; Nizamoglu, S., High-Performance White Light-Emitting Diodes over 150 lm/W Using Near-Unity-Emitting Quantum Dots in a Liquid Matrix. *ACS Photonics* **2022,** *9* (4), 1304-1314.
44. Bang, S. Y.; Suh, Y.-H.; Fan, X.-B.; Shin, D.-W.; Lee, S.; Choi, H. W.; Lee, T. H.; Yang, J.; Zhan, S.; Harden-Chaters, W.; Samarakoon, C.; Occhipinti, L. G.; Han, S. D.; Jung, S.-M.; Kim, J. M., Technology progress on quantum dot light-emitting diodes for next-generation displays. *Nanoscale Horizons* **2021,** *6* (2), 68-77.
45. Alivisatos, A. P., Semiconductor Clusters, Nanocrystals, and Quantum Dots. *Science* **1996,** *271* (5251), 933-937.
46. Smith, A. M.; Nie, S., Semiconductor Nanocrystals: Structure, Properties, and Band Gap Engineering. *Accounts of Chemical Research* **2010,** *43* (2), 190-200.
47. Jasieniak, J.; Califano, M.; Watkins, S. E., Size-Dependent Valence and Conduction Band-Edge Energies of Semiconductor Nanocrystals. *ACS Nano* **2011,** *5* (7), 5888-5902.
48. Peterson, M. D.; Cass, L. C.; Harris, R. D.; Edme, K.; Sung, K.; Weiss, E. A., The Role of Ligands in Determining the Exciton Relaxation Dynamics in Semiconductor Quantum Dots. *Annual Review of Physical Chemistry* **2014,** *65* (1), 317-339.
49. Boles, M. A.; Ling, D.; Hyeon, T.; Talapin, D. V., The surface science of nanocrystals. *Nature Materials* **2016,** *15* (2), 141-153.
50. Hines, D. A.; Kamat, P. V., Recent Advances in Quantum Dot Surface Chemistry. *ACS Applied Materials & Interfaces* **2014,** *6* (5), 3041-3057.
51. Katsiev, K.; Ip, A. H.; Fischer, A.; Tanabe, I.; Zhang, X.; Kirmani, A. R.; Voznyy, O.; Rollny, L. R.; Chou, K. W.; Thon, S. M.; Carey, G. H.; Cui, X.; Amassian, A.; Dowben, P.; Sargent, E. H.; Bakr, O. M., The Complete In-Gap Electronic Structure of Colloidal Quantum Dot Solids and Its Correlation with Electronic Transport and Photovoltaic Performance. *Advanced Materials* **2014,** *26* (6), 937-942.
52. Kirkwood, N.; Monchen, J. O. V.; Crisp, R. W.; Grimaldi, G.; Bergstein, H. A. C.; du Fossé, I.; van der Stam, W.; Infante, I.; Houtepen, A. J., Finding and Fixing Traps in II–VI and III–V Colloidal

Quantum Dots: The Importance of Z-Type Ligand Passivation. *Journal of the American Chemical Society* **2018,** *140* (46), 15712-15723.
53. Giansante, C., Library Design of Ligands at the Surface of Colloidal Nanocrystals. *Accounts of Chemical Research* **2020,** *53* (8), 1458-1467.
54. Kennehan, E. R.; Munson, K. T.; Grieco, C.; Doucette, G. S.; Marshall, A. R.; Beard, M. C.; Asbury, J. B., Exciton–Phonon Coupling and Carrier Relaxation in PbS Quantum Dots: The Case of Carboxylate Ligands. *The Journal of Physical Chemistry C* **2021,** *125* (41), 22622-22629.
55. Leger, J. D.; Friedfeld, M. R.; Beck, R. A.; Gaynor, J. D.; Petrone, A.; Li, X.; Cossairt, B. M.; Khalil, M., Carboxylate Anchors Act as Exciton Reporters in 1.3 nm Indium Phosphide Nanoclusters. *The Journal of Physical Chemistry Letters* **2019,** *10* (8), 1833-1839.
56. Schnitzenbaumer, K. J.; Dukovic, G., Comparison of Phonon Damping Behavior in Quantum Dots Capped with Organic and Inorganic Ligands. *Nano Letters* **2018,** *18* (6), 3667-3674.
57. Atwater, H. A.; Polman, A., Plasmonics for improved photovoltaic devices. *Nature Materials* **2010,** *9* (3), 205-213.
58. Clavero, C., Plasmon-induced hot-electron generation at nanoparticle/metal-oxide interfaces for photovoltaic and photocatalytic devices. *Nature Photonics* **2014,** *8* (2), 95-103.
59. Knight, M. W.; Sobhani, H.; Nordlander, P.; Halas, N. J., Photodetection with Active Optical Antennas. *Science* **2011,** *332* (6030), 702-704.
60. and, S. L.; El-Sayed, M. A., Optical Properties and Ultrafast Dynamics of Metallic Nanocrystals. *Annual Review of Physical Chemistry* **2003,** *54* (1), 331-366.
61. Brongersma, M. L.; Halas, N. J.; Nordlander, P., Plasmon-induced hot carrier science and technology. *Nature Nanotechnology* **2015,** *10* (1), 25-34.
62. Zhang, Y.; He, S.; Guo, W.; Hu, Y.; Huang, J.; Mulcahy, J. R.; Wei, W. D., Surface-Plasmon-Driven Hot Electron Photochemistry. *Chemical Reviews* **2018,** *118* (6), 2927-2954.
63. Wu, K.; Chen, J.; McBride, J. R.; Lian, T., Efficient hot-electron transfer by a plasmon-induced interfacial charge-transfer transition. *Science* **2015,** *349* (6248), 632-635.
64. Nishijima, Y.; Ueno, K.; Yokota, Y.; Murakoshi, K.; Misawa, H., Plasmon-Assisted Photocurrent Generation from Visible to Near-Infrared Wavelength Using a Au-Nanorods/TiO2 Electrode. *The Journal of Physical Chemistry Letters* **2010,** *1* (13), 2031-2036.
65. Linic, S.; Chavez, S.; Elias, R., Flow and extraction of energy and charge carriers in hybrid plasmonic nanostructures. *Nature Materials* **2021,** *20* (7), 916-924.
66. Wolff, C. M.; Frischmann, P. D.; Schulze, M.; Bohn, B. J.; Wein, R.; Livadas, P.; Carlson, M. T.; Jäckel, F.; Feldmann, J.; Würthner, F.; Stolarczyk, J. K., All-in-one visible-light-driven water splitting by combining nanoparticulate and molecular co-catalysts on CdS nanorods. *Nature Energy* **2018,** *3* (10), 862-869.
67. Mubeen, S.; Lee, J.; Singh, N.; Krämer, S.; Stucky, G. D.; Moskovits, M., An autonomous photosynthetic device in which all charge carriers derive from surface plasmons. *Nature Nanotechnology* **2013,** *8* (4), 247-251.
68. Song, J.; Long, J.; Liu, Y.; Xu, Z.; Ge, A.; Piercy, B. D.; Cullen, D. A.; Ivanov, I. N.; McBride, J. R.; Losego, M. D.; Lian, T., Highly Efficient Plasmon Induced Hot-Electron Transfer at Ag/TiO2 Interface. *ACS Photonics* **2021,** *8* (5), 1497-1504.
69. Zhang, H.; Govorov, A. O., Optical Generation of Hot Plasmonic Carriers in Metal Nanocrystals: The Effects of Shape and Field Enhancement. *The Journal of Physical Chemistry C* **2014,** *118* (14), 7606-7614.
70. Brown, A. M.; Sundararaman, R.; Narang, P.; Goddard, W. A., III; Atwater, H. A., Nonradiative Plasmon Decay and Hot Carrier Dynamics: Effects of Phonons, Surfaces, and Geometry. *ACS Nano* **2016,** *10* (1), 957-966.

71. Yuan, W.; Zhu, B.; Fang, K.; Li, X.-Y.; Hansen, T. W.; Ou, Y.; Yang, H.; Wagner, J. B.; Gao, Y.; Wang, Y.; Zhang, Z., In situ manipulation of the active Au-TiO₂ interface with atomic precision during CO oxidation. *Science* **2021,** *371* (6528), 517-521.
72. Atta, S.; Pennington, A. M.; Celik, F. E.; Fabris, L., TiO2 on Gold Nanostars Enhances Photocatalytic Water Reduction in the Near-Infrared Regime. *Chem* **2018,** *4* (9), 2140-2153.

Chapter 2. Experimental Methods

2.1 Time Resolved Spectroscopy Techniques

2.1.1 Transient Infrared Absorption Spectroscopy

A Coherent Systems Astrella Ti:Sapphire regenerative amplifier system laser system was used (800 nm, 5 W power output, 35 fs pulse width, 1 kHz repetition rate) with infrared (IR) and visible optical parametric amplifiers (OPAs) and an Helios Fire transient absorption spectrometer (Ultrafast Systems LLC) to do transient infrared experiments. The visible pump beams were generated from the visible OPA by sum frequency generation of the signal and by second harmonic generation of the signal through a BBO crystal, respectively. The pump beams were chopped at a rate of 500 Hz to obtain a ΔA spectrum and were also directed onto a motorized delay stage to get transient results. From the IR OPA, the signal and idler were mixed in an AgGaAs DFG crystal to form the 5000 nm IR probe**.** An iHR 320 Horiba spectrometer (component of Helios Fire setup) was used with a 50 grooves/mm grating. A nitrogen cooled 128 x 128 pixel mercury cadmium telluride (MCT) detector was used.

2.1.2 Visible Femtosecond Transient Absorption

A Coherent Systems Ti:Sapphire regenerative amplifier system (800 nm fundamental, 2 W power output, 150 fs pulse width, 1 kHz repetition rate) with a Helios spectrometer (Ultrafast Systems LLC) was used for the visible picosecond experiments. This setup is further described in a related study by Wu *et al.*[1] The 800 nm fundamental laser output was split to generate the pump and probe beams. The fundamental beam was frequency doubled through a BBO crystal to get the 400 nm pump.

The beam was focused at the sample and a chopper was used, at a rate of 500 Hz. The second half of the 800 nm beam was focused onto a sapphire window to generate a white light continuum (WLC) as the probe. To get a ΔA spectrum, the WLC was split to form reference and signal beams and were focused into fiber coupled multichannel spectrometer with a complementary metal-oxide semiconductor (CMOS) for detection.

2.1.3 Time Correlated Single Photon Counting

A mode-locked Ti:Sapphire laser (Tsunami oscillator pumped by a Spectra Physics 10 W Millenia Pro) was used with a fundamental output beam of 800 nm (~100fs, 80 MHz). The 800 nm beam traveled through a pulse picker (Conoptics, USA) and was then frequency doubled to generate the 400 nm excitation beam that would pass through the 1 cm cuvette containing the sample (right angle geometry). For detection, a microchannel plate photomultiplier tube (Hamamatsu R3809U-51) was used, and the analysis done by a TCSPC board (Becker & Hickel SPC 600). Samples were transferred to 1 cm cuvettes.

2.2 Quantum Dot Syntheses

2.2.1 Cd_3P_2 QDs

Cd_3P_2 QDs were synthesized according to the procedure described by Wu *et al.*[1] A mixture of CdO (77 mg), oleic acid (OA, 0.4 mL), and octadecene (ODE, 9 mL) was vented using a Schlenk line and alternated between being put under vacuum and argon for 1 min each, five times at approximately 75 °C. The temperature was then raised to 230 °C under Ar until the solution appeared clear. The temperature was raised once again to 250 °C and tris(trimethylsilyl)phosphine in ODE (0.2 mmol, 0.5 mL) was added, allowed to react for 35 sec, and removed from heat. The flask

was put into a water bath to cool and stop the reaction from proceeding further. A small amount of toluene was added to the reaction mixture and transferred to 2 15 mL falcon tubes. An excess of ethanol was added to each falcon tube to help precipitate out the QD. The sample was centrifuged for 5 min at 5500 rpm three times, each time removing the supernatant and adding a small amount of toluene and a large volume of ethanol. The sample was dissolved in the solvent of choice, chloroform, and centrifuged one last time after which the supernatant was collected, and UV-Vis taken to determine the absorption of the QD. The diameter of the QDs are about 3 nm from TEM (Figure 2.1) and the UV-vis absorption peak lies at 760 nm.

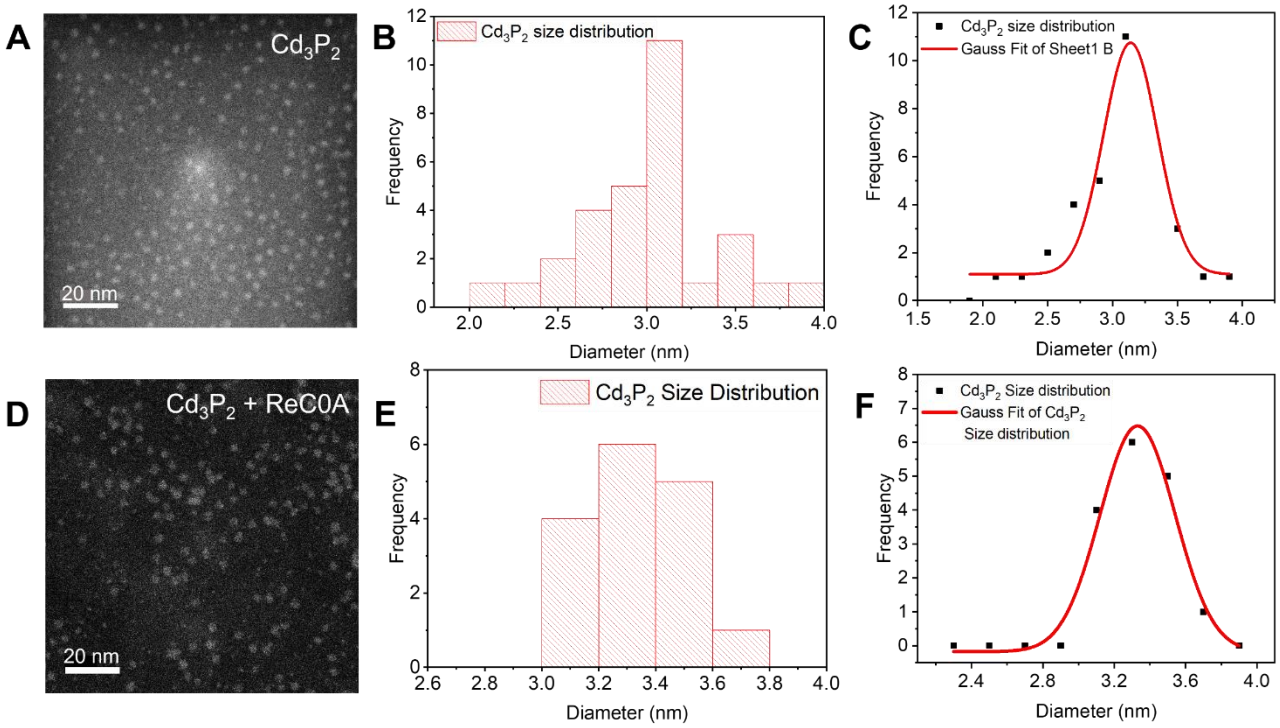

Figure 2.1. A) HR TEM image of Cd_3P_2, B) Histogram of size distribution of Cd_2P_3 QDs, C) Gaussian fit of histogram in (B) showing a size distribution of 3.14 ± 0.208 nm, C) HR TEM image of Cd_3P_2 with ReC0A on it, E) Histogram of size distribution of QDs in (D), F) Gaussian fit of histogram in (E) showing a size distribution of 3.33 ± 0.211 nm.

2.2.2 TOPO Capped CdSe QD Syntheses

Several varying sizes of CdSe QDs were synthesized for this dissertation according to previous procedure described by Hanifi *et al.* with some changes.[2] Generally, the larger CdSe QDs were synthesized by mixing trioctylphosphine oxide (TOPO, 3 g), octadecylphosphonic acid (ODPA, 400 mg) and CdO (60 mg) in a three necked round bottomed flask. While stirring, the mixture was heated to 150 ºC and left under vacuum for 30 min. After switching to argon, the heat was increased to 350 ºC to dissolve the CdO. Once the solution became transparent, trioctylphosphine (TOP) was added (1.5 g) and the temperature raised to 370 ºC. Meanwhile, selenide powder was dispersed in TOP (58 mg Se into 360 mg TOP) and sonicated to dissolve it. Once the mixture reached the desired temperature, the selenide solution was added to the reaction mixture. The reaction was allowed to proceed for varying amounts of time while observing color changes depending on the desired size. The larger sizes (580-620 nm) were obtained by waiting for the solution to turn an extremely dark brown color. The middle sizes (545-550 nm) were obtained by waiting for the solution to turn a very dark red color. Once the corresponding color was observed, 3mL ODE was injected to stop the reaction and the round bottomed flask was cooled with a stream of air, then a water bath. The smallest sizes of CdSe (490-525 nm) were synthesized with the same procedure except the amount of ODPA added was 280 mg and the reaction was stopped once the solution turned from an orange to darker orange color. For each QD, once the reaction stopped, the color of the solution reverted to a lighter version. In order of size (smallest to largest), the QDs were generally yellow, bright red, and dark red colored. Once cooled, a small amount of toluene was added to flask, after which the QD solution was split between two 15 mL falcon tubes. An excess amount of ethanol was added to each tube to aid in the precipitation of the QDs. The solution in both falcon tubes was centrifuged for 5 min at 5500 rpm. Once finished, the

supernatant was disposed of and the precipitated QDs were redispersed in ~ 2 mL of toluene with excess ethanol added afterwards. This centrifugation procedure was performed three times to obtain washed QDs. After the last centrifugation and removal of supernatant, the pellet was dissolved in hexanes and centrifuged one last time. The resultant supernatant was comprised of QDs and were removed and transferred to a vial, avoiding any pellets that had formed. The resultant CdSe QDs used throughout this dissertation had exciton absorptions at 490 nm (yellow), 505 nm (dark yellow) 545/550 nm (bright red), and 580/582/620 nm (dark red to dark brownish) corresponding to diameters ranging from 2.3 nm to 5.6 nm.

2.2.2 Oleate Capped CdSe QD Syntheses

Oleic acid (OA) capped CdSe quantum dots were synthesized according to the procedure by Lai *et al.* with a few modifications.[3] Briefly, CdO (78 mg), OA (0.8 mL), and ODE (10 mL) were added into a three necked round bottomed flask. The flask was put under vacuum for 30 min, after which it was argon purged under stirring. The temperature was set to 260 ^{o}C to dissolve the CdO. During the heating process, a Se suspension (0.1 M) was made by dispersing 79 mg Se powder into 10 mL ODE and sonicating for several minutes. Once the reaction mixture appeared transparent, 2 mL of the Se suspension was injected into the flask and allowed to react for 8 min at 250 ^{o}C. Afterwards, between 0.05 to 0.1 mL was slowly injected into the flask and the mixture was allowed to react for 4 min. The injection/4 min reaction cycles were repeated until the desired QD size was achieved. During the reaction, aliquots of the sample were removed to check the exciton band position. At the end of the reaction, the mixture was separated into four 15 mL falcon tubes and 5 mL chloroform, 5 mL acetone, and 2.5 mL methanol added. The tubes were centrifuged for 3 min at 5300 rpm to precipitate out the QDs. The resultant pellet was saved, and the supernatant discarded. This process was repeated twice more. After the final centrifugation cycle, the pellet was

dissolved in hexanes and centrifuged once more. The solution was then transferred to a vial for future use. The acquired size had an exciton absorption at 550 nm.

2.2.4 CdSe/ZnS Core Shell Structures

CdSe/ZnS core shell structures were synthesized according to Zhu et al[4] and Li et al[5] with several modifications. The ZnS shell was grown using the successive ion layer adsorption and reaction (SILAR) method. The zinc precursor solution (0.08 M) was made by dissolving 64 mg of ZnO into 2.5 mL OA and 7 mL ODE. The solution was heated to 300 °C to get it to be colorless after which the temperature was lowered to 100 °C and maintained there. The sulfur solution (0.08 M) was prepared by dissolving 25 mg sulfur powder in 10 mL ODE and sonicating until the solution was clear. The oleic acid capped CdSe in hexanes (100 nmol) was added to a three necked round bottomed flask with ODA (1.5 g) and ODE (6.4 mL). The flask was put under vacuum for 30 min at 75 °C to remove the hexanes and subsequently Ar purged. The shells were grown one at a time and the amounts of precursor for each shell growth was determined using the method described in Reiss *et al.*[6] The temperature was raised to 210 °C where the Zn precursor was injected first, and after 10 min, the desired amount of sulfur was added. The reaction was allowed to proceed for 20 min. This made up one growth cycle. The growth cycles were repeated until the desired number of ZnS layers was achieved. Here we made CdSe/ZnS QDs with 0, 1, 3, and 6 monolayers (ML), each ML corresponding to a growth cycle. The sizes of the QDs were determined by TEM (Figures 2.2 and 2.3); the CdSe core had a diameter of 3.16 nm, while 1ML was 3.79 nm, 3ML, 3.92 nm, and 6ML was 4.9 nm. They will be referred to as CdSe, CdSe/$ZnS_{0.64}$, CdSe/$ZnS_{0.77}$, and CdSe/$ZnS_{1.75}$ throughout Chapter 5 of this dissertation.

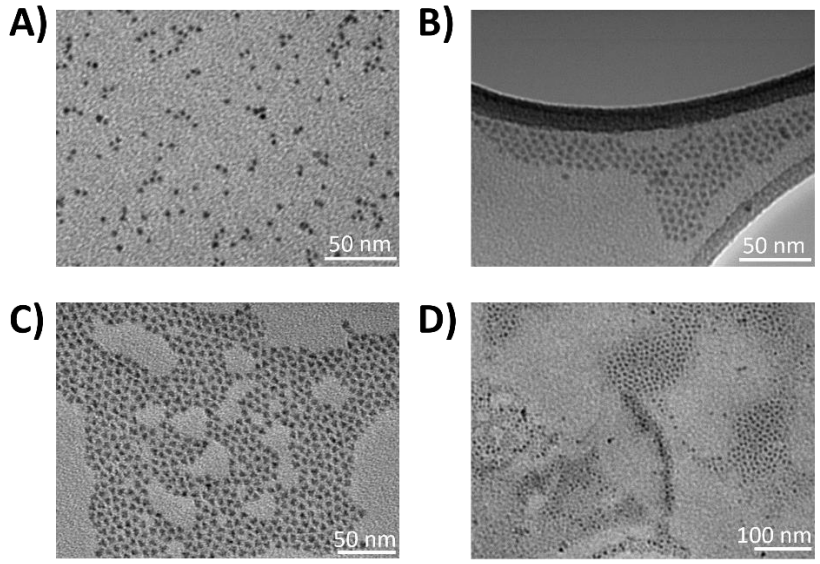

Figure 2.2. TEM images of CdSe core and CdSe/ZnS core shell structures. A) CdSe core. B) $CdSe/ZnS_{0.64}$ which underwent 1 growth cycle, believed to be 1 ML of ZnS. C) $CdSe/ZnS_{0.77}$ which was created with 3 growth cycles, believed to be 3 ML. D) $CdSe/ZnS_{1.75}$ which used 6 growth cycles, expected to be 6 ML.

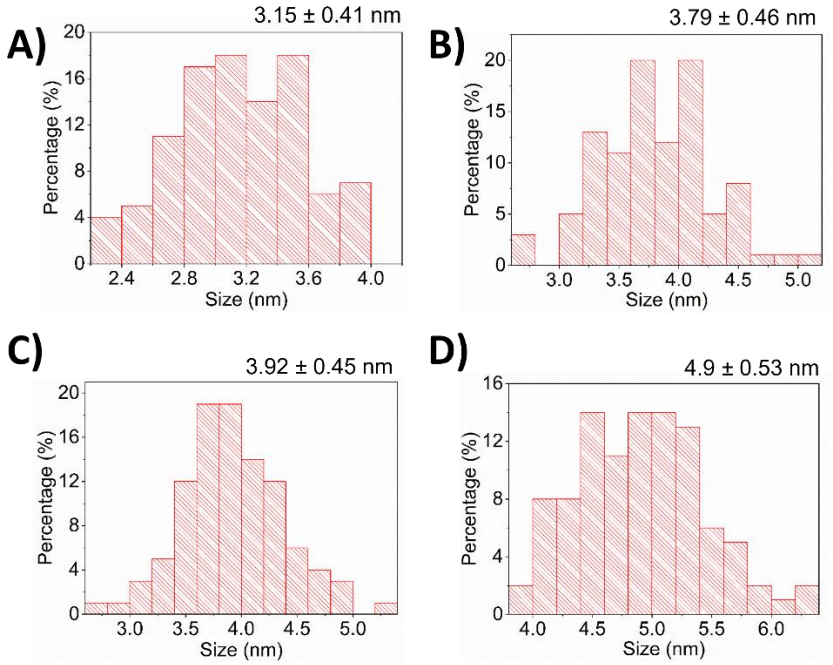

Figure 2.3. Size distributions of CdSe and CdSe/ZnS QDs. A) CdSe core. B) $CdSe/ZnS_{0.64}$ C) $CdSe/ZnS_{0.77}$ D) $CdSe/ZnS_{1.75}$.

2.3 Sample Preparation

2.3.1 Cd_3P_2-ReC0A complexes

Previous methods of adsorbing molecules to QD surfaces involve adding an excess of the molecule and sonicating in a solvent (heptane) in which the quantum dot is soluble, but not the molecule. Instead, the samples were freshly prepared on the day experiments were performed by adding ReC0A in MeCN (2 mL) to a volume of Cd_3P_2 in chloroform (~0.33 mL, 75 μM) corresponding to a UV-Vis absorbance of 0.3 optical density (OD) for both in a 1:1 ratio of ReC0A (400 nm) to Cd_3P_2 (exciton, ~700 nm). The sample was rotary evaporated, dissolved in 1 mL of heptane to result in a final QD concentration of 25 μM, and sonicated for 3 hours to allow the ReC0A to bind to the QD. We added ReC0A to the QD solution and determined through FTIR spectral analysis that approximately 60% of the ReC0A added bound to the surface, resulting in a final concentration of 0.52 mM and an average of 21 Re complexes per QD. All samples were transferred into a 1 mm optical glass cuvette obtained from Starna and stirred for experiments. For experiments with the hole scavenger, 10% TEA was added to the already prepared Cd_3P_2-ReC0A samples in the dark and were wrapped in aluminum foil when transporting the cuvette. All chemicals were used as purchased and the ReC0A was synthesized by the Kubiak group at University of California San Diego. The TA experiments were compared with and without Ar purging and no difference was evident.

2.3.2 CdSe-ReC0A complexes

Samples for both transient absorption and time resolved IR were prepared the same way, with a difference of solvents. The day before experiments were performed, ReC0A in MeCN was rotary evaporated depending on the desired concentration. The QD in hexanes was then added to

the same vial on top of the dried ReC0A and rotary evaporated once again. The dried samples were stored overnight. On the experiment day, the dried sample was redissolved in 1 mL of either heptane (TA) or hexanes (TRIR) and sonicated for 2 hours. The amount of QD rotary evaporated corresponded to an OD of 0.3 determined from UV-Vis. Four concentrations of ReC0A were added to each QD: 0.25x, 0.5x, 1x, and 2x. The volumes of ReC0A used corresponded to the desired amount of catalyst adsorbed to the surface. For example, if 1xRe was desired, 1 mL of ReC0A in MeCN (0.18 OD at 400 nm) was used to obtain a ~ 1:2 ratio of ReC0A to QD according to a 0.3 OD absorbance in the UV-Vis. For TA experiments, the prepared samples were transferred to Starna 1 mm optical glass cuvettes and stirred for experiments. For TRIR, samples were injected into a Harrick FTIR cell with a spacer of 950 um and stirred as well. Both UV-Vis (Agilent) and FTIR (ThermoFisher Nicolet is50) were taken before each TRIR experiment, and UV-Vis before TA.

2.3.3 CdSe-ReCxA complexes

Samples for both transient absorption and time resolved IR were prepared the similar to what is described in 2.3.1. The desired concentration of ReCxA and ReS_2 in MeCN (~0.3 OD in UV-Vis and 0.7 OD in FTIR, respectively) was mixed with the QD in hexanes and the solvent removed by rotary evaporation. The dried samples were redissolved in 1 mL of hexanes and sonicated for 2 hours. The amount of QD rotary evaporated corresponded to an OD of 0.3 determined from UV-Vis while the concentrations for ReCxA that were used also corresponded to an OD of 0.3. The concentration of ReS_2 that was used had an absorption of 0.7 OD in FTIR. For TA experiments, the prepared samples were transferred to Starna 1 mm optical glass cuvettes and stirred for experiments. For TRIR, CdSe-ReCxA samples were injected into a Harrick FTIR cell with a spacer of 950 um and stirred as well.

2.3.4 CdSe/ZnS-ReS_2-TiO_2 films

For CdSe-ReS_2 and CdSe/ZnS-ReS_2, after sonicating, the samples were deposited onto a TiO_2 film. The TiO_2 films were prepared by using commercially available TiO_2 paste and using the doctor blade method to create thin films on sapphire windows. The films were then annealed in an oven at 500 ºC for an hour. The oven was then turned off and samples left overnight. A small volume (30 μL) of the QD-ReS_2 complexes was spin coated onto the films at 200 rpm for 15 seconds and 50 rpm for 10 sec. Afterwards, the rest of the samples were drop casted onto the films until each sample has a strong absorption in the IR. Both UV-Vis and FTIR (ThermoFisher Nicolet is50) were taken before each TRIR experiment, and UV-Vis (Agilent) before TA.

2.4 Other Characterization Methods

2.4.1 Electrochemistry and Cyclic Voltammetry

Reproduced from Gebre, S. T.; Kiefer, L. M.; Guo, F.; Yang, K. R.; Miller, C.; Liu, Y.; Kubiak, C. P.; Batista, V. S.; Lian, T., Amine Hole Scavengers Facilitate Both Electron and Hole Transfer in a Nanocrystal/Molecular Hybrid Photocatalyst. *Journal of the American Chemical Society* **2023,** *145* (5), 3238-3247.

Solvents were obtained from Fisher Scientific. Acetonitrile was degassed with argon, dried over alumina, and dispensed by a custom-made solvent system. Reagents obtained from commercial sources; pentacarbonylchlororhenium, decamethylferrocene (Fc*), and 2,2'-bipyridine from Sigma Aldrich, 2,2'-bipyridine-4,4'-dicarboxylic acid from Alfa Aesar, Tetrabutylammonium hexafluorophosphate ($TBAPF_6$, Aldrich, 98%) was recrystallized twice from methanol and dried at

90°C overnight. Triethylamine (Sigma ≥ 99%) was distilled from CaH_2 and stored over 3Å sieves in a N_2 glovebox prior to use. Experiments were performed on a BASi Epsilon potentiostat. Experiments were run in 0.1 M $TBAPF_6$ in 5 mL acetonitrile (MeCN) with 1 mM catalyst for control experiments. Experiments involving TEA were run in 0.1 M $TBAPF_6$ in 4.5 mL MeCN and 0.5 mL TEA with 1mM catalyst. Decamethyferrocene (1 mM) was used as an internal standard for all scans. The reported potentials were converted to NHE using literature values.[7-8] A 20 mL scintillation vial with a custom cap was used for all CV experiments. A 3 mm diameter glassy carbon working electrode, Pt wire counter electrode, and Ag/AgCl reference electrode (separated from solution in a glass tube filled with 0.1 M $TBAPF_6$ in MeCN and fitted with a CoralPor tip). The glassy carbon electrode was polished with 15, 3, and 1 micron diamond successively then thoroughly rinsed with methanol and dried before use. The platinum wire was flame-treated with a butane torch before use. Ar and "bone dry" CO_2 were run through Drierite columns and then through a sealed vial of dry MeCN filled with 3Å sieves. An oven dried cannula was used to transfer the MeCN saturated solution from the vial to the electrochemical set up. Electrochemical set-ups were sparged for at least 10 minutes prior to electrochemical experiments. Gas flow was continued over the solution during experiments. Ohmic drop was corrected for by using the iR-compensation tool of the potentiostat. The tool corrected for between 90-100% of the measured resistance.

2.4.2 High Resolution Transmission Electron Microscopy (HR-TEM)

HR TEM experiments for Chapter 3 were conducted at Oakridge National Laboratory. Aberration-corrected high-angle annular dark-field (HAADF) and bright-field (BF) image pairs were obtained on a Nion UltraSTEM U100 operated at 100kV. Samples were deposited on lacey carbon grids and baked at 80°C overnight under high vacuum to minimize hydrocarbon contamination.

2.5 References

1. Wu, K. F.; Liu, Z.; Zhu, H. M.; Lian, T. Q., Exciton Annihilation and Dissociation Dynamics in Group II-V Cd3P2 Quantum Dots. *Journal of Physical Chemistry A* **2013,** *117* (29), 6362-6372.
2. Hanifi, D. A.; Bronstein, N. D.; Koscher, B. A.; Nett, Z.; Swabeck, J. K.; Takano, K.; Schwartzberg, A. M.; Maserati, L.; Vandewal, K.; van de Burgt, Y.; Salleo, A.; Alivisatos, A. P., Redefining near-unity luminescence in quantum dots with photothermal threshold quantum yield. *Science* **2019,** *363* (6432), 1199-1202.
3. Lai, R.; Liu, Y.; Luo, X.; Chen, L.; Han, Y.; Lv, M.; Liang, G.; Chen, J.; Zhang, C.; Di, D.; Scholes, G. D.; Castellano, F. N.; Wu, K., Shallow distance-dependent triplet energy migration mediated by endothermic charge-transfer. *Nature Communications* **2021,** *12* (1), 1532.
4. Zhu, H.; Song, N.; Lian, T., Controlling Charge Separation and Recombination Rates in CdSe/ZnS Type I Core−Shell Quantum Dots by Shell Thicknesses. *Journal of the American Chemical Society* **2010,** *132* (42), 15038-15045.
5. Li, J. J.; Wang, Y. A.; Guo, W.; Keay, J. C.; Mishima, T. D.; Johnson, M. B.; Peng, X., Large-Scale Synthesis of Nearly Monodisperse CdSe/CdS Core/Shell Nanocrystals Using Air-Stable Reagents via Successive Ion Layer Adsorption and Reaction. *Journal of the American Chemical Society* **2003,** *125* (41), 12567-12575.
6. Reiss, P.; Protière, M.; Li, L., Core/Shell Semiconductor Nanocrystals. *Small* **2009,** *5* (2), 154-168.
7. Connelly, N. G.; Geiger, W. E., Chemical Redox Agents for Organometallic Chemistry. *Chemical Reviews* **1996,** *96* (2), 877-910.
8. Pavlishchuk, V. V.; Addison, A. W., Conversion constants for redox potentials measured versus different reference electrodes in acetonitrile solutions at 25°C. *Inorganica Chimica Acta* **2000,** *298* (1), 97-102.

Chapter 3. Amine Hole Scavengers Facilitate both Electron and Hole Transfer in a Nanocrystal/Molecular Hybrid Photocatalyst

This chapter is reproduced from a previous paper: Gebre, S. T.; Kiefer, L. M.; Guo, F.; Yang, K. R.; Miller, C.; Liu, Y.; Kubiak, C. P.; Batista, V. S.; Lian, T., Amine Hole Scavengers Facilitate Both Electron and Hole Transfer in a Nanocrystal/Molecular Hybrid Photocatalyst. *Journal of the American Chemical Society* **2023,** *145* (5), 3238-3247.

3.1 Introduction

Photoreduction of CO_2 is a promising way to mitigate the environmental impact of CO_2 and generate solar fuels.[1-2] Many CO_2 reduction catalysts are not photoactive or require high energy photons from the solar spectrum.[3] A common way of circumventing this issue is utilizing a sensitizer that can absorb light and deliver electrons to the catalyst. Quantum dots (QDs) are excellent sensitizer candidates as they absorb broad ranges of light, their absorption and emission spectra are size tunable, they can offer stability and also provide a source of electrons.[4-8] Ideal QD sensitizers must be strongly quantum confined, have absorption in the visible and near IR regions and have a conduction band edge with high enough energy for the catalyst reduction.[9] Cd_3P_2 is such a QD, having a conduction band potential of -1.32 V vs NHE for particles with a band gap of 650 nm.[10]

In this study we investigate photoinduced electron transfer from Cd_3P_2 to the tricarbonyl CO_2 reduction catalyst Re(4,4'-R_2-bpy)$(CO)_3$Cl (bpy=bipyridine; R=COOH) (ReC0A). Rhenium tricarbonyl catalysts have shown high selectivity and efficiency in reducing CO_2.[11-16] However, when used as a photocatalyst, ReC0A exhibits poor absorption of solar light since it requires photons with wavelength shorter than 400 nm to generate a ^{1}MLCT state before it can be reduced. Here, we bind

the ReC0A catalyst to Cd_3P_2 QDs, so the QDs can both absorb visible light and transfer the photoexcited electrons to the ReC0A adsorbate for catalysis.

A sacrificial electron donor must replenish the QD to sustain the CO_2 reduction.[1, 17] We have chosen triethylamine (TEA) which is a well-studied hole scavenger. However, like other amines, TEA is known to have complicated effects on quantum dots because it can function as a hole scavenger and as a capping ligand.[18-19] It has also been shown to function as a passivating ligand to remove hole traps at small concentrations,[20] and shift the conduction band edge to more negative potentials.[21] In this study, we investigate how the presence of TEA affects photoinduced electron transfer from Cd_3P_2 QDs to ReC0A. We show that while TEA functions as a hole scavenger, it also serves as a base to modify the surface charge of Cd_3P_2 QDs, thus increasing the electron transfer rate from the QD to the catalyst.[21-22]

3.2 Results and Discussion

3.2.1 Sample Preparation and Characterization

Cd_3P_2 QDs are particularly suitable for our study since they have a highly reductive conduction band potential and their absorption onset is red shifted relative to the absorption of the Re catalyst, enabling selective excitation of the QD in the visible range.[10, 23] Recent advances in synthesis methods have enabled the preparation of Cd_3P_2 QDs with narrow size distributions under safe conditions.[24-26] The Cd_3P_2 synthesis used in this study is described in detail in Chapter 2.2.1. Previous studies reported efficient electron transfer from Cd_3P_2 QDs to Rhodamine B, an electron acceptor with a reduction potential of -0.55 V vs NHE, for Cd_3P_2 nanoparticles of bandgaps up to ~1140 nm.[27] Because the photocatalyst, ReC0A (Figure 3.1a), has a much more negative reduction potential[28] (first: -1.06 V vs NHE, second: -1.66V vs NHE, Figure S3.17), only QDs with a 1S exciton band shorter than 800 nm

are estimated to have a sufficiently high conduction band (CB) edge position to reduce the catalyst. Thus, by incorporating Cd_3P_2, the spectral range over which the QD-ReC0A hybrid photocatalyst can be excited extends from ~400 nm to ~800 nm. The QDs in this study show 1S exciton bands at 650nm – 720 nm, which correspond to diameters of ~2.6 nm to 3.1 nm (Figure S3.1) using a previously published empirical relationship between the QD size and 1S exciton peak position (see Section 3.4.1 for details).[10, 23] Compared to a bulk exciton radius of 18 nm, these QDs are highly quantum confined.[10, 23] The CB edge electron ($1S_e$) and valence band (VB) edge hole ($1S_h$) energies for this size Cd_3P_2 nanoparticle are estimated to be ~ -1.34 V and 0.60 V vs. NHE, respectively .[29-31] The procedure for preparing QD/catalyst complexes in heptane solution is described in Section 2.3.1. The ReC0A catalyst coordinates to the Cd^{2+} sites through the deprotonated carboxylic acid groups[32], with either one or two COO^- groups bound to the surface depending on the ReC0A concentration. Though each COO^- can bind through one or both O atoms, the resulting change in frequency between the two binding motifs is not large enough to be observed.[33] When the ReC0A is bound to the QD, a blue shift of up to 40 nm is observed in the QD 1S exciton band (Figure 3.1b). One possibility for this drastic blue shift is the etching of the QD surface caused by catalyst binding. The observed blue shift would correspond to a decrease in the QD diameter by 0.5 nm, due to the strong quantum confinement. High resolution transmission electron microscope (HRTEM) experiments were conducted on Cd_3P_2 and ReC0A bound Cd_3P_2 to see if etching was indeed occurring. The images (Figure 2.1) were analyzed using ImageJ software and results indicate that the Cd_3P_2 (~720 nm) has a size distribution of 3.1 ± 0.2 nm and the Cd_3P_2-ReC0A has a size distribution of 3.3 ± 0.2 nm. We find that the addition of ReC0A does not result in smaller Cd_3P_2 QDs. Another possible explanation for the observed blue shift could be that these strongly quantum confined particles may be sensitive to the change in surface ligand environment. Replacing the native oleic acid (OA) ligands on the QD surface by ReC0A, which has a large dipole moment (~8.1 Debye)[34] and a relatively small HOMO-

LUMO gap, may alter the confinement potential and hence the confinement energy.[10] We did not observe this blue shift when ReC0A was bound to CdS or CdSe QDs (Figure S3.4), which are both less quantum confined than Cd_3P_2. We attempted to determine if the blue shifting can be reversed by adding an excess of oleic acid capping ligand (20% by volume) to the QD/ReC0A solution at room temperature, which unfortunately significantly degraded the samples and did not lead to conclusive findings. This experiment was performed again at slightly elevated temperatures. The OA stock was heated to 57 and 108 °C, and upon addition of OA (1 to 20% by volume) to the QD-ReC0A and QD only samples, there was a continual blue shift of the UV-Vis spectrum with increasing amounts of OA added for both samples (Figure S3.2). It seems that adding excess amount of OA cannot reverse the observed blue shift. It is likely that OA cannot displace adsorbed ReC0A complexes because they are not soluble in the heptane solution. The most likely reason for the observed shift is the strong interaction of the QD with the adsorbate, forming mixed energy levels.[35] This effect is strengthened with the addition of more molecules to the QD surface, which is observed with ReC0A (Figure S3.3). Furthermore, with this effect, the direction of the shift may depend on the relative energy level of the QD and the adsorbate. We have previously observed that the addition of Rhodamine B and methyl viologen can result in both blue and red shifts of the Cd_3P_2 exciton band, respectively. Although these observations are consistent with this model, it requires further investigation and theoretical modelling, which is ongoing and will no longer be discussed here.

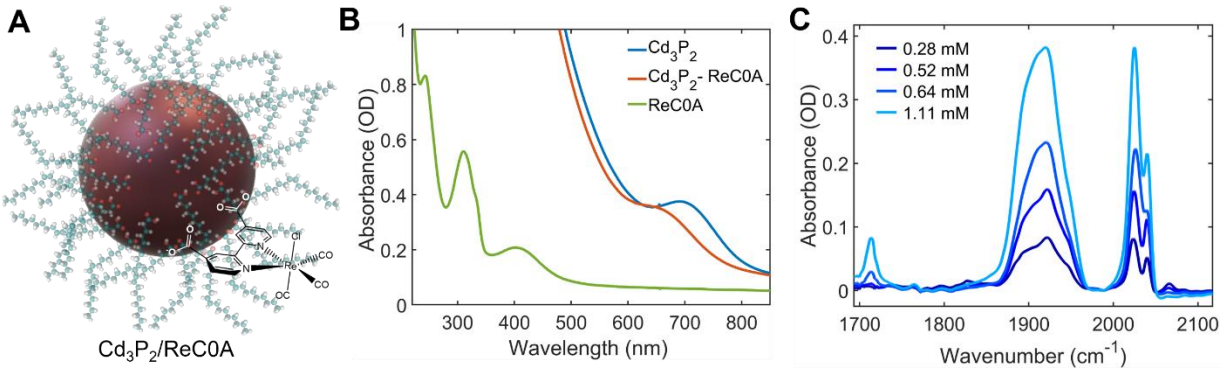

Figure 3.1. (A) The structure of the catalyst ReC0A; (B) UV-Vis spectra of the ReC0A in acetonitrile (green), Cd_3P_2 in $CHCl_3$ (blue) and Cd_3P_2-ReC0A in heptane (red). A blue shift occurs when the ReC0A is bound to the QD; (C) FTIR of the three carbonyl stretching bands of ReC0A on Cd_3P_2, the two high frequency modes result from coupling due to aggregation. At higher concentrations of ReC0A, protonated COOH groups appear ~ 1715 cm^{-1}.

Our DFT analysis of binding modes provide a first principles interpretation of the FTIR spectra of ReC0A bound to Cd_3P_2 surfaces (Figure 3.2) as compared to the spectrum of ReC0A in acetonitrile where the catalyst exhibits three carbonyl stretching modes in the 2000 cm^{-1} region corresponding to an out of phase symmetric stretch (1905 cm^{-1}), an asymmetric stretch (1922 cm^{-1}) and an in phase symmetric stretch (2025 cm^{-1}). When the ReC0A is bound to the Cd_3P_2, two bands appear for the symmetric stretch at 2025 cm^{-1} and 2040 cm^{-1} (Figure 3.1c). It was previously reported that this band splitting is the result of coupling of the carbonyl stretches due to aggregation, specifically with two bands in the dimer and three bands in a trimer.[33, 36] This is a reasonable assumption for the ReC0A on Cd_3P_2, since the average ReC0A per QD is relatively high, at 21 molecules for a concentration of 0.49 mmol ReC0A. Since the Re compound is not soluble in heptane, all complexes observed in the FTIR spectra are assumed to be bound to the QD. With this number of Re molecules on the surface, it is possible that some of the oleic acid (OA) ligands are removed during the adsorption process. Our

computational modeling of the interaction between capping oleic acid (OA) ligands and Cd_3P_2 suggests that the carboxyl groups of OA are deprotonated and protons prefer to bind to the surface P sites. The same binding motif is observed when ReC0A molecules are adsorbed to Cd_3P_2 surfaces. At low concentrations of ReC0A, both carboxyl groups of ReC0A bind to surface Cd^{2+} site in the deprotonated form. Therefore, no IR peak is observed around 1715 cm^{-1} for ReC0A at concentrations of 0.28 mM and 0.54 mM. As the concentration of ReC0A increases, due to the limited Cd_3P_2 surface area, ReC0A molecules begin to bind to the Cd_3P_2 surface through a single carboxyl group, with the other protonated COOH group pointing away from Cd_3P_2 QDs, giving rise to the characteristic IR peak at ~1715 cm^{-1} (Figure 3.2). According to the energetics of the adsorbate obtained by DFT calculations, the estimated minimum concentration of ReC0A necessary for transition from a bi-carboxylate binding mode to a mono-carboxylate binding motif is 0.7 mM (See 3.4.14). This confirms that the appearance of the IR peak at ~1715 cm^{-1} (at high concentrations of ReC0A) is due to that transition. Binding of carboxyl groups to Cd^{2+} sites is concerted with deprotonation of the carboxylic acid group.

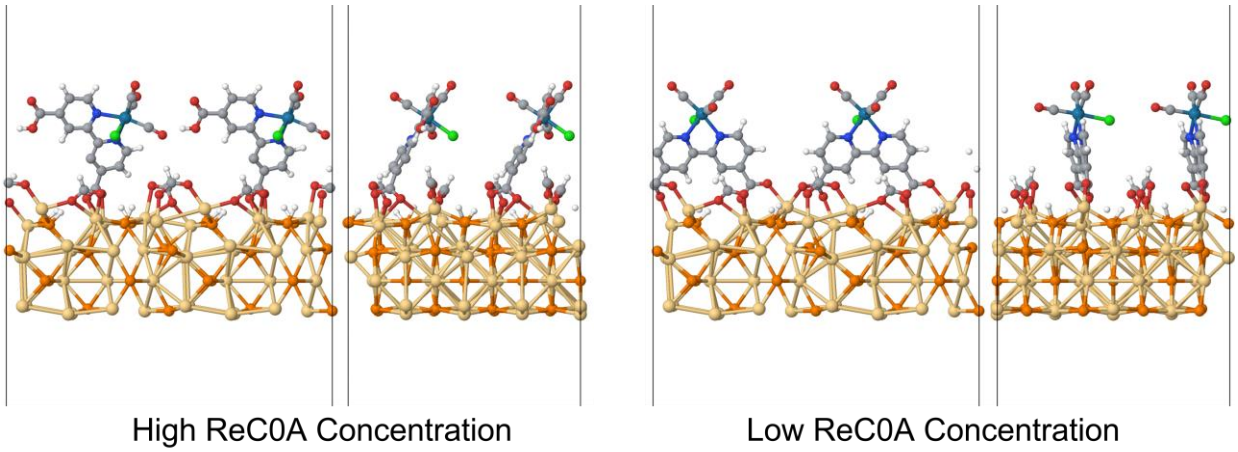

Figure 3.2. DFT models of the ReC0A catalyst adsorbed on the Cd_3P_2 (100) surface at different concentrations. The left panel shows binding modes at high concentration of ReC0A adsorbed on the surface through a single carboxyl group. The right panel shows that for low concentrations, ReC0A adsorbed on the surface through both carboxyl groups. The binding of the second carboxyl group is responsible for the disappearance of the 1700 cm^{-1} peak in experimental absorbance spectrum when lowering the ReC0A concentration (seen in Figure 3.1).

Cyclic voltammetry (CV) experiments were conducted on the ReC0A and ReC0A/TEA systems to determine their respective reduction potentials. In a solution without TEA, the first reduction, which is known to be bipyridine based[37], is at -1.06 V vs NHE. Upon addition of TEA, the first reduction of the ReC0A is pushed more negative to -1.14 V vs NHE and a new, small peak appears at -1.29 V vs NHE (Figure S3.17). The shift in the first reduction potential is due to the acid-base chemistry between TEA and the bpy-C0A ligand. The new peak corresponds to the reduction of the formed triethylammonium ($TEAH^+$). The second reduction of the complex, which is known to be metal based,[37] has the same potential (-1.66 V vs NHE) for both the protonated and deprotonated ReC0A species. This is also true for the 3rd reduction at -2.20 V vs NHE. To determine if the origin

of the shift of the first reduction, and of the new peak at -1.29 V vs NHE, resulted from acid-base chemistry of the ligand with TEA, control experiments were run using $Re(bpy)(CO)_3Cl$ (ReCl) (Figure S3.16). The first reduction of ReCl remained the same (-1.16 vs NHE) regardless of the presence of TEA in solution and there was no appearance of a peak between the first and second reduction of the complex. TEA did not bind to the Re metal center because of its weaker coordinating ability when compared to the chloride ion.[38]

Figure 3.3 shows the energy level diagram obtained by combining the values determined from the CV experiments, including energetically allowed electron and hole transfer events.

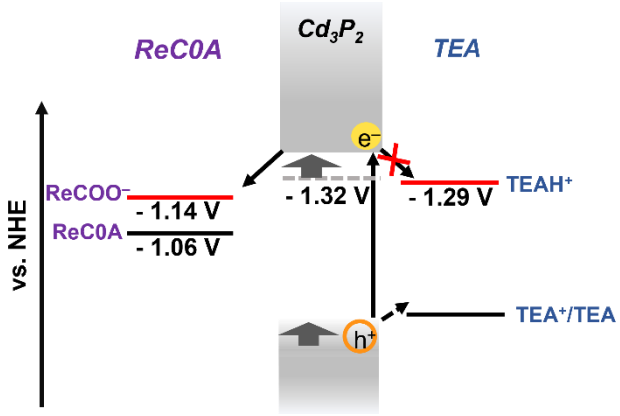

Figure 3.3. Energy level diagram including energetically allowed electron/hole transfer events. The potentials for ReC0A and TEA come directly from the CV experiments in Figure S3.17, while the potential for Cd_3P_2 comes from the calculation mentioned earlier in this manuscript.

3.2.2 Addition of Hole Scavenger TEA to QD

We investigated whether TEA could function as a hole scavenger for Cd_3P_2 QDs since Cd_3P_2 QDs have not been extensively studied as a photosensitizer. Previous studies using CdSe have reported that adding low concentrations of TEA enhances the QD fluorescence. The enhancement

occurs as a result of the hole traps being filled upon binding of TEA.[39] At higher concentrations, TEA scavenges the holes, causing photoluminescence (PL) quenching.[40-41] We observed the same effect on Cd_3P_2 over a range of concentrations. Time-correlated single photon counting (TCSPC) experiments with TEA concentrations of 7.1 mM-710 mM (0.1% Vol to 10% Vol) were conducted by exciting the QD with 400 nm light and detecting its PL at 780 nm. These experiments show that at low concentrations of TEA (up to 35 mM), there is a slight PL enhancement (Figure S3.12b). The TEA concentration that results in enhancement is much higher with Cd_3P_2 than with CdS or Cd_2As_3 for which PL enhancement has been reported with up to 1 mM TEA.[42] At higher concentrations of TEA, the initial amplitude of the Cd_3P_2 PL is lower than that of the free QD (Figure S3.12c). In all cases above 35 mM, TEA quenched the PL (decay rate of 87.6 ± 4.59 ns), confirming that TEA does indeed behave as a hole scavenger in this system (Figure 3.4a, S3.12c).

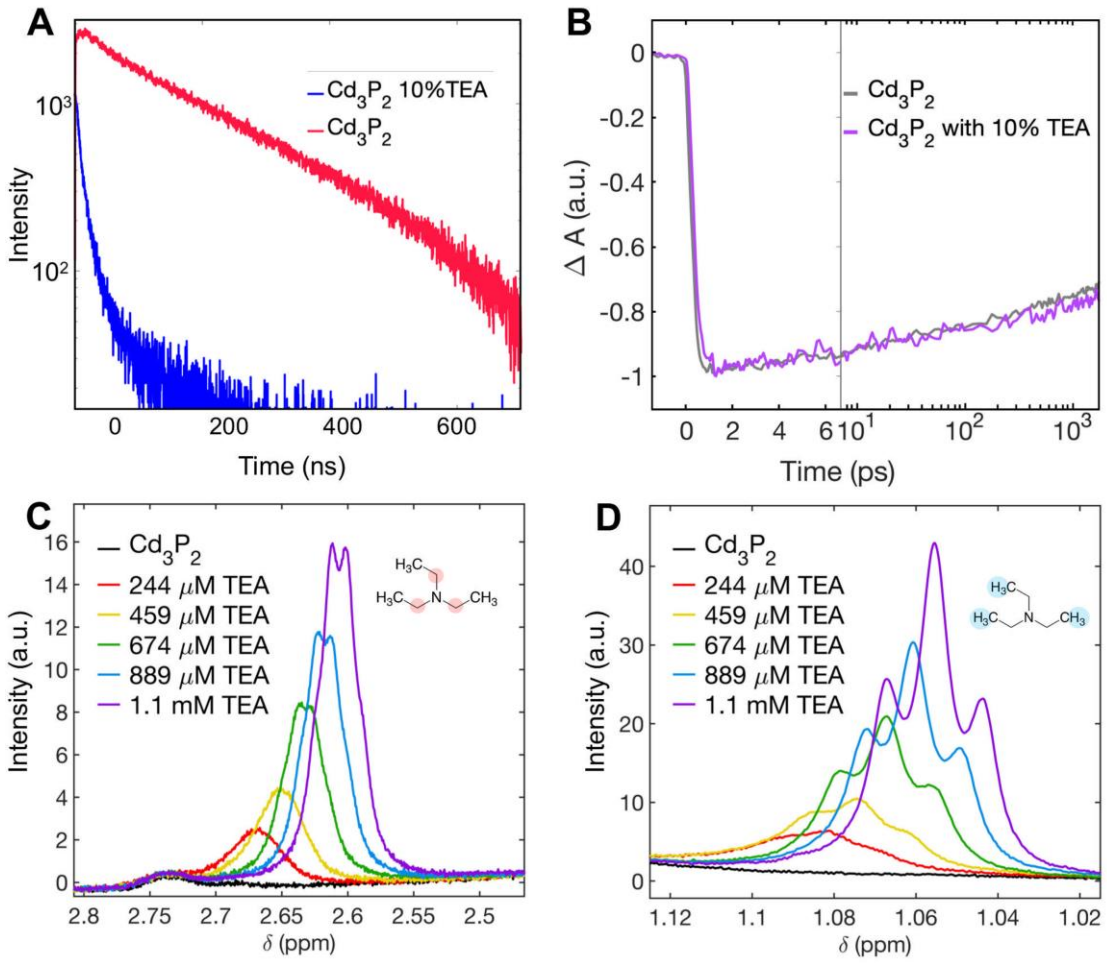

Figure 3.4. (A) Time resolved photoluminescence collected at 780 nm showing the decay of the Cd_3P_2 and how the photoluminescence is quenched by the TEA, (B) Kinetic traces of 1S exciton bleach of Cd_3P_2 with and without 10% TEA, (C) ^{1}H NMR spectra of the ethyl (~ 2.6 ppm) and (D) methyl (~ 1.06 ppm) regions of the TEA and how the chemical shifts change as a function of TEA concentration.

It is difficult to quantify by PL quenching how much TEA is on the QD surface since the two effects on PL intensity occur at varying concentrations of TEA. It is well known that primary amines bind to QD surfaces and they are often used as capping ligands,[19] but it remains uncertain whether tertiary amines also bind directly to the QD surface. When TEA was introduced for ligand exchange on CdSe, using ^{13}P NMR, Scaiano *et al* observed the removal of the capping ligand, trioctylphosphine

oxide (TOPO), suggesting that TEA binds to the surface.[40] Our DFT computational analysis suggests that TEA does not replace the capping groups since it is energetically unfavorable. However, the deprotonation of the surface P–H groups by TEA is energetically favorable (Figure 3.5). During synthesis, it is possible for the oleic acid capping ligands to become deprotonated, after which those protons can bind to the P groups within the QD surface structure. It is these P-H groups from which TEA can abstract protons. We conducted ^{1}H NMR titration experiments on the Cd_3P_2 in $CDCl_3$, adding consecutive amounts of TEA to reach different concentrations to possibly observe a similar loss of the capping ligand (Figure S3.13a). Surprisingly, we observed a concentration dependent deshielding of the CH_2 and CH_3 protons of the TEA (at 2.6 ppm and 1.06 ppm, respectively), with the highest degree of deshielding occurring at low concentrations, compared to the ^{1}H NMR spectrum of free TEA in $CDCl_3$ (Figure 3.4C, D). This suggests that either TEA is preferentially solvating the QD[43] or that TEA is loosely bound to the QD and exchanges at a rate faster than the experimental resolution without displacing the native OA, consistent with DFT calculations. The former case implies that at the smallest concentrations of TEA, the environment experiences the largest perturbance (for the smallest concentrations, all TEA are protonated by the surface P–H groups, leading to a larger chemical shift of CH_2 and CH_3 protons). As more TEA is added, the environment gradually changes towards that of the free TEA, and thus becomes more shielded in the NMR experiments. In the latter case, as more TEA is added, while fast exchange still occurs, there is a higher fraction of unbound species, shifting the average to favor the direction of free TEA NMR peaks. The NMR experiments did not determine whether the protons are being extracted from the surface, possibly due to the high concentration of TEA compared to the QD capping ligands (surface P–H groups as a result of surface ligand deprotonation are likely to be the proton source according to our computational modeling) and the limited sensitivity of the instrument, though it is known that TEA is routinely used for surface proton removal in QD synthesis.[22] While preferential solvation and proton

abstraction are most likely occurring, we also observe changes in the OA peaks upon addition of TEA. At the lowest concentrations of added TEA (244 and 459 μM), we observe broadening on the more deshielded side of the OA bands (5.3 ppm and 1.25ppm for the CH and CH_3 groups respectively (Figure S3.13b, c), that recover when more TEA is added. This suggests that when there is little TEA present, it seeks out the QDs and deprotonates the surface P–H groups, positioning itself near the hydrophilic surface rather than being in the nonpolar heptane environment. As more TEA is added, the protonated TEA form ($TEAH^+$) is better solvated by the excess TEA molecule, therefore it enters the bulk solution and leaves the QD surface, explaining the disappearance of the broadening of the OA peaks. It could also mean that preferential solvation occurs at low concentrations of TEA, as broadening is an indication of a different solvation environment,[44] and the broadening occurs only at lower TEA concentrations. There is not sufficient evidence that there is strongly bound TEA since there is no permanent peak assigned for such a species. It may also be possible to investigate the protonation chemistry of the QD surface with and without TEA by adding increasing concentrations of OA after synthesis to act as a proton source. Unfortunately, we were unable to perform this experiment, however, the concentration of OA titrated would need to be controlled in such a way as to not promote etching of the QD surface (<20% by volume, Figure S3.2).

NMR studies based on diffusion ordered spectroscopy (DOSY) were performed to further analyze the nature of the interaction between TEA and QD in these systems. DOSY NMR determines the diffusion coefficients of compounds in solution, allowing for a clearer identification of species in solution than possible with proton or carbon NMR (details in SI). Comparing Cd_3P_2 with and without TEA, the diffusion coefficients of oleate in each sample were similar (1.10 $\mu m^2/s$ vs 1.14 $\mu m^2/s$ with TEA) indicating no oleate ligands were displaced from the surface (Figure S3.14). In the case of TEA, DOSY was performed on TEA by itself and with the QD, where a difference in coefficients (3.82 $\mu m^2/s$ vs 2.94 $\mu m^2/s$ respectively), suggesting that some of the hole scavenger may be closely

associated or bound to the surface at a low concentration of 0.49 mM (Figure S3.15). We are not able to explicitly distinguish between bound and free TEA since only one peak is observed. Therefore, it is important to note that the smaller diffusion coefficient we observe upon addition of TEA to the QD represents both free and bound TEA populations undergoing fast chemical exchange.

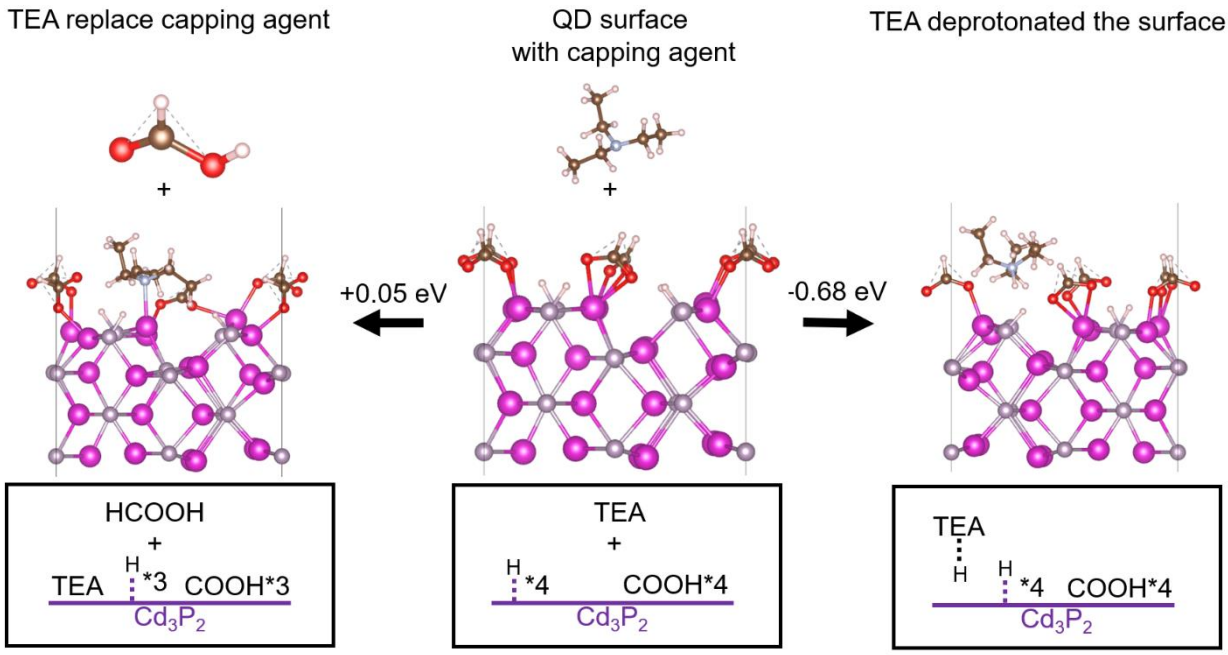

Figure 3.5. Two possible reaction pathways after adding a TEA molecule: 1) the TEA molecule deprotonates a surface-bound proton; 2) the TEA molecule replaces a capping agent (HCOOH) molecule.

Before attempting to observe electron transfer with ReC0A, transient absorption experiments were performed to confirm that in the case of TEA, the hole has a negligible contribution to the exciton bleach kinetics. Using a mixture of Cd_3P_2 in a 10% TEA/90% heptane solution, no difference was observed between the exciton bleach kinetics of the mixture and that of the free QD within 1 ns, indicating that there is a negligible hole contribution to the 1S exciton bleach (XB) signal (Figure 3.4b),

consistent with a previous report.[10] Furthermore, we conclude that electron transfer to the $TEAH^+$ species has not been observed since electron transfer would result in a faster 1S exciton bleach recovery. Although this process is energetically favorable (Figure 3.3), the interaction of $TEAH^+$ species with the QD surface is likely too weak to enable electron transfer. As shown in Figure 3.5, computation modeling indicates that upon deprotonation, the new $TEAH^+$ species diffuses away from the surface and into the bulk solution, consistent with our hypothesis from ^1H NMR studies.

3.2.3 Electron Transfer in Cd_3P_2/ReC0A Complexes

Visible transient absorption (TA) spectra of QD-ReC0A complexes were first measured with wavelengths less than the energy needed to electronically excite the ReC0A (500 nm and 700 nm) to establish that electron transfer from the QD to the complex occurs (Figure 3.6a). All excitation wavelengths resulted in similar QD 1S exciton bleach kinetics. We elected to use 400 nm for the majority of the experiments because it does not interfere with our QD bleach kinetics measurements. Although the estimated concentration of QD is 21 times smaller than ReC0A (25 μM vs 525 μM), its molar extinction coefficient of ε_{400nm} = 530,477 L mol^{-1} cm^{-1} at 400 nm (ε_{650nm} = 124,700 L mol^{-1} cm^{-1} at the band gap), is 156 times larger than that of ReC0A (ε_{400nm} ~3400 L mol^{-1} cm^{-1}).[10, 45] As a result, ReC0A is expected to absorb a negligible amount of light due to the much larger absorptance of the QD. The TA spectra of free QDs (Figure 3.6b) show a bleach of QD 1S exciton band (XB) centered at ~680 nm and a photoinduced absorption band at a longer wavelength. It has been shown previously that the XB in Cd_3P_2 QDs is dominated by the state filling signal of the $1S_e$ level and can be used to follow the kinetics of the CB edge electron.[10] The TA spectra of QD-ReC0A complexes (Figure 3.6c) show similar TA spectra features as free QDs at early delay time, but the decay of the XB signal is much faster, indicating shorter lived CB electrons due to electron transfer to the adsorbed ReC0A. This is consistent with the observation of TA spectra at ~ 520 nm, just over the Cd_3P_2 photoinduced

absorption (Figure 3.6C), which can be assigned to the reduced ReC0A species (Figure S3.5b).[46] However, the signal at ~520 nm is overshadowed by the continuously growing charge separated state signal (electron in ReC0A, hole in VB) which also red shifts as it grows in.[47] In the charge separated state, the exciton transition energy changes due to its interaction with the separated charge, giving rise to derivative feature with shifted exciton bleach in the TA spectra, which has been observed previously.[48-51] Additional spectra of Cd_3P_2 with methyl viologen excited at 400 nm confirms that this red shifting signal corresponds to the growth of the charge separated state (Figure S3.6). While it is also possible that this signal may correspond to the QDs in solution that have the largest amount of catalyst on the surface (due to the blue shift of UV-Vis spectrum), and therefore contributes to the faster bleach recovery at higher energy, the growth of the CSS is likely the main cause of the red shift. Both effects can contribute to fast bleach recovery. To corroborate the growth of the reduced ReC0A species in the TA spectra, a separate experiment where a mixture of ReC0A and triethanolamine (TEOA) in MeCN was pumped at 400 nm to generate the excited MLCT and singly reduce the complex (Figure S3.5b). As a result, at around 1 μs once the MLCT state has decayed away, there is a small peak at ~505 nm corresponding to the reduced ReC0A. Control experiments without TEOA are shown in Figure S3.5a.

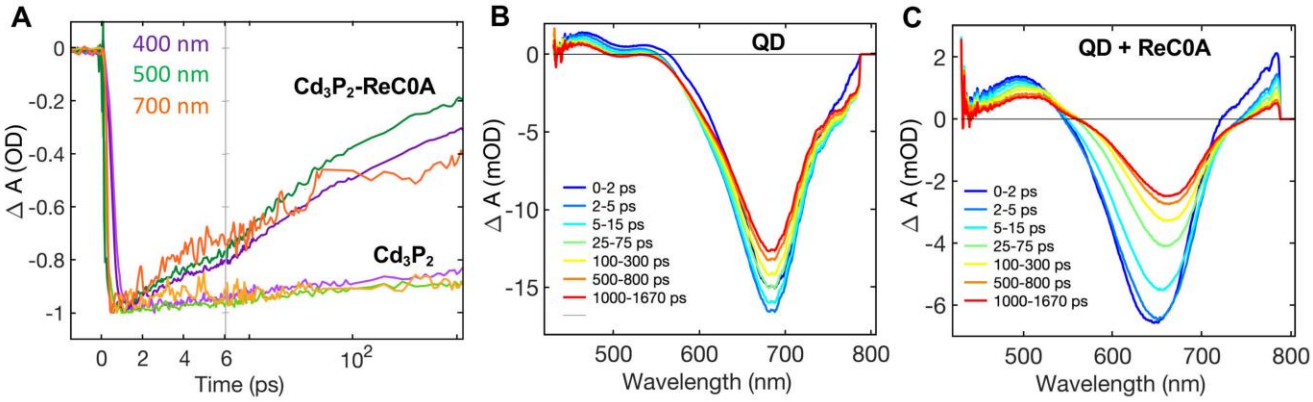

Figure 3.6. (A) Kinetic traces of the 1S exciton bleach of the QD with and without ReC0A attached.

The traces show similar kinetics for excitation wavelengths of 700 nm (orange), 500 nm (green) and 400 nm (purple); TA spectra at multiple time delays of (B) Cd_3P_2 and (C) ReC0A bound to Cd_3P_2.

There is an initial loss of XB amplitude with Cd_3P_2-ReC0A, compared to Cd_3P_2, on a timescale faster than the instrument response, which is ~ 250 fs. This loss can be seen comparing the peak depths of Figures 3.6b and c, where the ReC0A bound QD has a depth of just under half of that of the free QD, where both have the same concentrations of QDs. This fast amplitude loss can be caused by either ultrafast electron transfer or electron trapping on defect sites introduced by the adsorption of the ReC0A. With regards to the ultrafast ET, comparing the bleach amplitudes of the QD and QD-ReC0A samples upon excitation at 400, 500, and 700 nm will provide insight into whether this process occurs. Figure S3.9 shows unnormalized kinetics for each sample at each excitation wavelength. Pumping at 400 and 560 nm shows the clearest difference in bleach amplitude, where 50 to 60% of the amplitude has disappeared. At 700 nm excitation, the bleach amplitude loss is less, about 30%. Both 400 and 560 nm pumps are at higher energy than the QD CB edge, so ultrafast ET is more likely to occur, whereas, at 700 nm, there is a more direct excitation to the CB edge. However, since there is still bleach amplitude loss for each wavelength, it is likely that the significant cause is due to electron trapping with a possible small degree of ultrafast ET. Upon catalyst adsorption, if ReC0A replaces native OA due the large volume of ReC0A binding, that will generate surface defects, which can act as electron traps. Both these possibilities contribute to the loss in bleach amplitude, with electron trapping being the main cause. We will further examine this phenomenon in future studies with RhB and will not further discuss it here. Transient IR spectra of the CO stretching mode shows a large positive feature that is consistent with the formation of Fano resonance (FR) signals (Figure S3.7).[52] These TRIR experiments were done with Cd_3P_2 and varying amounts of ReC0A (0.25x, 1x, and 2xRe) in hexanes under 500 nm excitation at high pump fluence to investigate. At this experiment's smallest

concentration, 0.25xRe, the FR, a large positive peak, can be observed at approximately 2025 cm^{-1}. Upon the addition of more ReC0A (1x and 2xRe), the FR signal decays faster than the 0.25xRe case. Also, there is a growth of the singly reduced species peak at ~2005 cm^{-1} and a ground state bleach at ~2029 cm^{-1}. As more ReC0A is added (1x vs 2x), the amplitudes of both the bleach and singly reduced peak become larger (Figure S3.7d) and there is faster decay of the QD electron and FR signals. Both these TRIR and TA experiments demonstrate that Cd_3P_2 is indeed able to reduce the catalyst.

A concentration dependence study was conducted to determine how the electron transfer would be affected as the number of ReC0A molecules on the surface increased. We first observed that as the concentration increases, so does the blue shift of the 1S exciton band (Figure S3.10), as well as a greater loss of initial bleach amplitude. Some of the increased loss of the bleach is attributed to scattering as there is an average of 44 ReC0A on the surface for the highest concentration, making Cd_3P_2 more susceptible to aggregation in heptane. The concentration study revealed that as the concentration increased linearly, the bleach recovery rate constant also increased linearly (Figure 3.7a) with concentrations of 0.28 mM, 0.52 mM, 0.64 mM, 1.1 mM having half-lives of 1.74 ns, 438.6 ps, 138.5 ps, and 55.6 ps, respectively (Table 3.1). The average number of ReC0A complexes per QD are 11, 21, 26, and 44, respectively, and are thought to adsorb according to a Poisson distribution, as observed. The FTIR spectra (Figure 3.1c) show that at the two lowest concentrations of ReC0A on the QD, there is no band at ~ 1700 cm^{-1}, indicating that all the carboxylic acids are deprotonated.[53] As the concentration is increased, a band at 1715 cm^{-1} appears and grows as a function of ReC0A concentration (Figure 3.1c, far left). After the surface can no longer accommodate the ReC0As, the ones that are either partially bound (mono-carboxylate) or not bound at all are drawn to the ReC0As on the surface, due to their large dipole moment and lack of solubility in heptane. This possible unbound ReC0A environment is drastically different than that of the oleic acids and may affect the reorganization energy for interfacial electron transfer.

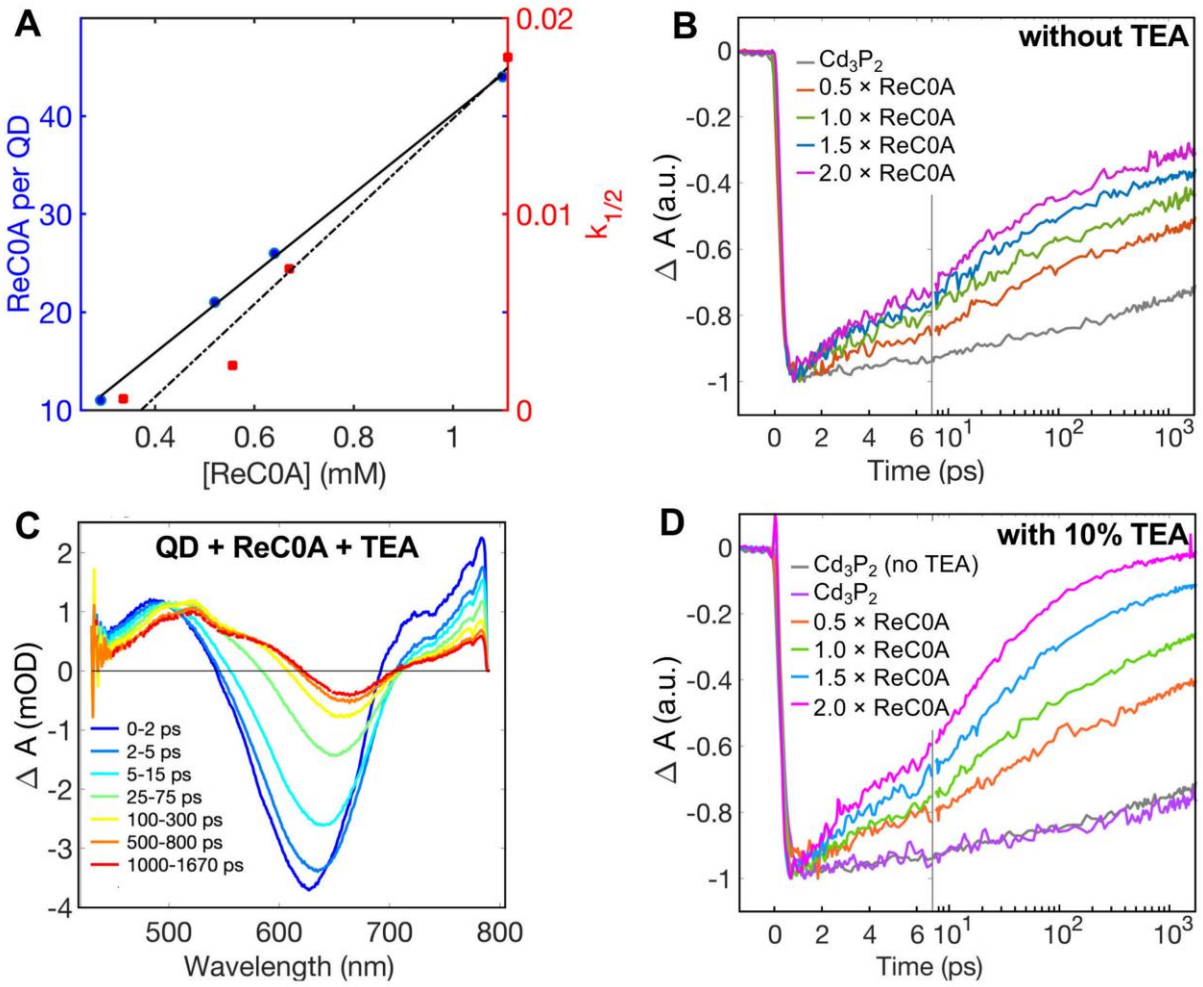

Figure 3.7. (A) The half-lives of the bleach decays of ReC0A on Cd_3P_2 and amount of ReC0A per QD plotted vs ReC0A concentration clearly show a linear relationship. TA spectra at multiple time delays of (B) Cd_3P_2, (C) ReC0A bound to Cd_3P_2 and (D) ReC0A bound to Cd_3P_2 with the addition of 10% TEA. The lower panels show the kinetics of the 1S exciton bleach of Cd_3P_2 with multiple concentrations of ReC0A (B) without TEA and (D) with 10% TEA. The addition of TEA shows an enhanced electron transfer rate from the Cd_3P_2 to the ReC0A.

3.2.4 Effect of TEA on ET in Cd_3P_2/ReC0A

Upon addition of the TEA to the Cd_3P_2-ReC0A system, an increase in electron transfer rate

was observed. TEA (10% by volume) was added to each concentration of ReC0A on the QD and the rate of exciton bleach recovery half time decreases (Table 3.1), indicating fast ET rates from the QD to ReC0A. The 1S exciton bleach recovery half-lives for the ReC0A concentrations of 0.28 mM, 0.52 mM, 0.64 mM, 1.10 mM after adding TEA are 348 ps, 73.5ps, 28.5 ps, and 12.5 ps, respectively. We observe the presence of a larger reduced ReC0A peak in the TA spectra (~ 520 nm) for the experiment containing TEA, indicating more reduced ReC0A is formed over the same experimental time, consistent with a faster electron transfer to the ReC0A in the presence of TEA (Figure 3.7b-d; Figure S3.10). TRIR data show that the amplitudes of reduced ReC0A and the ground state bleach increase with increasing concentrations of ReC0A, providing further evidence for this trend (Figure S3.7d). Figure S3.8a and b compare the 520 nm amplitudes for samples without and with TEA, respectively, demonstrating a clear difference in the growth of that absorption between the types of samples.

Table 3.1. Exciton bleach recovery half-lives in ReC0A-Cd_3P_2 with and without TEA

[ReC0A] (mM)	ReC0A-QD	ReC0A-QD + 10%TEA
	$\tau_{1/2,no\ TEA}$	$\tau_{1/2,\ TEA}$
0.28	1740.0 ± 11.9 ps	348.0 ± 16.5 ps
0.52	439.0 ± 12.6 ps	73.5 ± 8.0 ps
0.64	139.0 ± 9.3 ps	28.5 ± 6.4 ps
1.1	55.6 ± 12.1 ps	12.5 ± 0.4 ps

Many factors involving TEA may contribute to the observed increased in ET rate, including: TEA shifts the conduction band edges of QDs to a more negative potential by binding to the surface, donating electron density as it is an L-type ligand, as reported previously by Morgan *et al*;[21] the TEA

deprotonates the QD surface since it is a strong, non-nucleophilic base; and TEA may preferentially solvate the QD resulting in a slightly different electrostatic environment, as suggested by the NMR experiments. Our computational modeling is more consistent with the picture that TEA deprotonates the QD surface, resulting in negatively charged QD surfaces thus shifting the conduction band edge to more negative potentials (Figure 3.8). All these factors can possibly change the energetics of the QD towards a more negative conduction band edge and favor faster single electron transfer to the acceptor.

To attempt to confirm the shifting of the CB edge, we performed a TEA concentration dependent study with Cd_3P_2-0.5xReC0A, the smallest concentration we use throughout our study. At 0.5xRe, upon addition of 0.5%, 1%, and 5% TEA, it is clear that the ET to ReC0A is accelerated (Figure S3.11). As more TEA is added, it may continue to shift the CB edge further as a result. The higher the concentration of TEA added, the more TEA there would be to possibly alter the QD surface charge by deprotonation, preferentially solvate the QD, and bind to the surface to donate electron density. This serves as more potential evidence that TEA may shift the CB edge to facilitate faster ET to ReC0A. The half-lives of QD-0.5xRe with TEA were plotted and show a linear relationship similar to the ReC0A concentration dependent study.

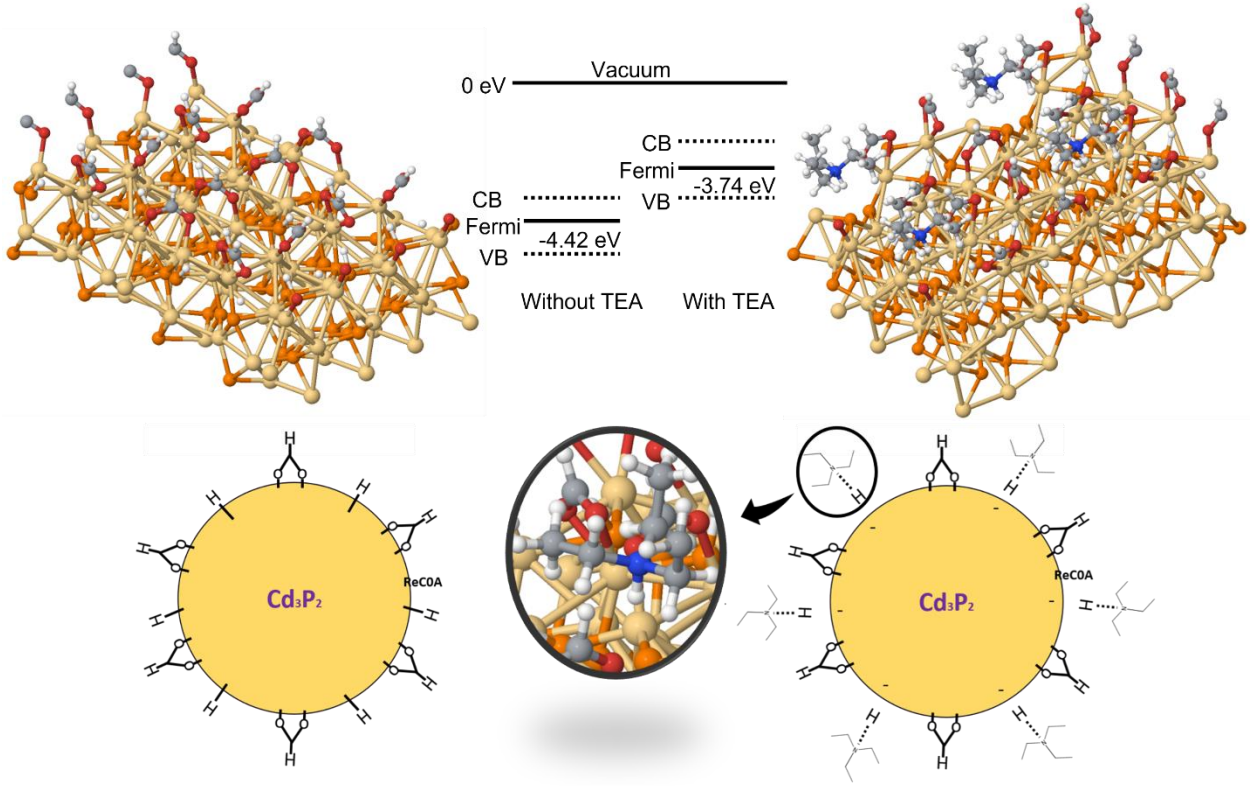

Figure 3.8. The shift of the Fermi level of Cd_3P_2 upon TEA addition to the surface. The addition of TEA abstracts protons from the Cd_3P_2 surface, resulting in a negatively charged surface, thus shifting up the Fermi level of the Cd_3P_2 quantum dot.

For completeness, we have tested whether the effect of TEA addition on other electron transfer systems, including CdS-ReC0A, CdSe-ReC0A, CdS with methyl viologen, and Cd_3P_2 with 4,4'-bipyridine. Each of these systems has different surface structures due to their different chemical compositions as well as different capping ligands and various electron acceptors. Though the conditions for each case varied, a similar enhanced electron transfer rate was observed for all of those systems (Figure S3.18), indicating that the properties of TEA could be changing the conduction band edge through a combination of proton extraction, L-type ligand binding and preferential solvation is generalizable to other systems leading to enhanced electron transfer to electron acceptors in various

systems beyond Cd_3P_2.

3.3 Conclusions

We have shown that full consideration of the effects of incorporation of hole scavengers in catalytic systems must be considered. In particular, we have found through our combined computational and experimental analysis that the hole scavenger TEA may have the ability to change the conduction band potential of the QD through multiple possible mechanisms, including surface proton abstraction since it is a strong non-nucleophilic base. Binding of TEA to the surface and passivating surface traps is predicted to be less likely according to our computational modeling due to the steric hindrance. The possible favorable change in the conduction band potential enhances the rate of electron transfer reactions from Cd_3P_2, an effect that is generalizable to other systems (e.g., CdS-ReC0A, CdSe-ReC0A, CdS-methyl viologen, etc). Preferential solvation of the nanoparticle complex may contribute to small changes in the immediately surrounding electrostatic environment. Aggregation of the electron acceptor, or an excess of the hole scavenger, are expected to lower the electron transfer barrier from the QD to the catalyst. These findings thus suggest that other hole scavengers might also have a double role as observed for TEA by not only supplying electrons to the nanoparticle-catalyst system but also potentially changing the energetics of the system, making it more favorable towards ligand reduction.

3.4 Supporting Information

3.4.1 Cd_3P_2 Size Determination

Using exciton band gap and TEM data from Wu et al, we fitted the band gap vs. size to the polynomial:

$$D = (0.00001258)\lambda_{BG}^2 - (0.01319)\lambda_{BG} + 5.806$$

where D is the nanoparticle diameter and λ_{BG} is band gap, both in nm.[10, 23]

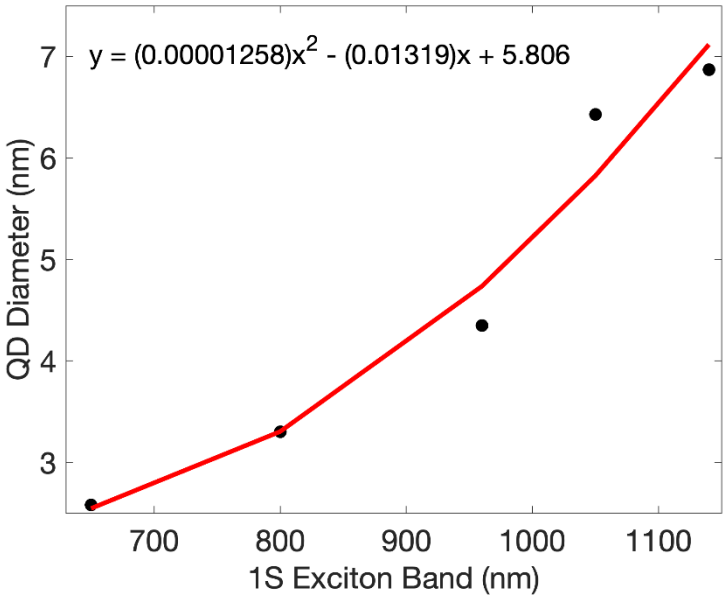

Figure S3.1. Polynomial of Cd_3P_2 band gap vs diameter.

3.4.2 Attempting to Reverse Exciton Band Blue Shifting

To reverse the blue shifting of the exciton band upon catalyst adsorption, 20% oleic acid (by volume) was added to the Cd_3P_2-ReC0A samples. Unfortunately, these results were inconclusive due to significant degradation of the QD. This experiment was repeated at two elevated temperatures, 57 and 108 °C, for both Cd_3P_2 and Cd_3P_2-ReC0A samples. After addition of ReC0A, there is a 20 nm blue shift that occurs and we found that this effect was not reversible upon addition of varying concentrations of OA (1 to 20%) and that there was a continual blue shift of up to 15 nm for both

the QD and QD-ReC0A samples. We attribute the blue shift upon catalyst adsorption to strong electronic coupling of the catalyst and a change in the QD surface dipole as Cd_3P_2 is strongly quantum confined and more sensitive to its surface environment. This is suggested by a continual blue shift with increasing amounts of ReC0A shown below and we will further investigate this at a later date.

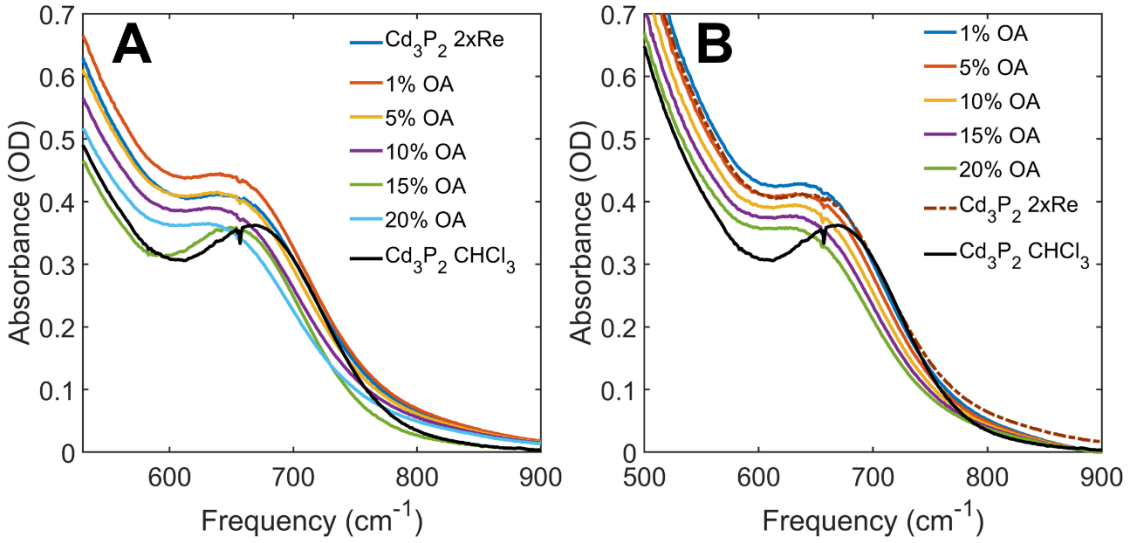

Figure S3.2. UV-Vis spectra after addition of oleic acid to Cd_3P_2-ReC0A samples at 57 (A) and 108 °C (B). Both spectra show that the exciton band further blue shifts upon addition of OA.

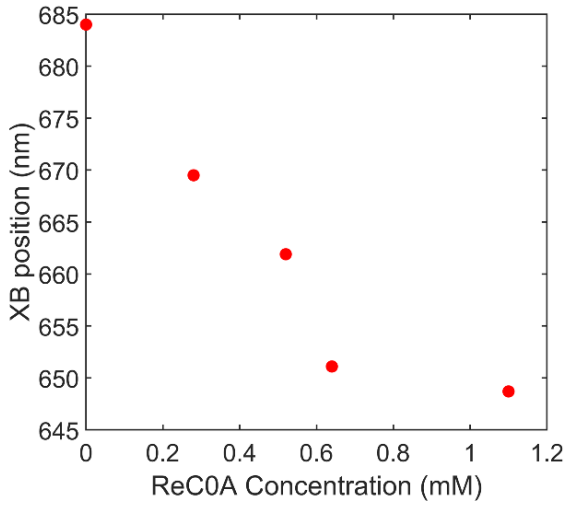

Figure S3.3. Plot of the exciton bleach shifting as a function of increasing ReC0A concentration. The

more ReC0A bound to the surface of the QD, the farther the exciton band blue shifts.

3.4.3 UV-Vis of ReC0A on CdS and CdSe

UV-Visible spectra for CdSe and CdSe-ReC0A in heptane and CdS and CdS-ReC0A in $CHCl_3$ and heptane, respectively. Note that there is no blue shift of the 1S exciton band upon addition of the ReC0A to either CdSe or CdS that was observed with Cd_3P_2. We attribute this to Cd_3P_2 being more quantum confined than the former QDs and more susceptible to surface dipole effects.

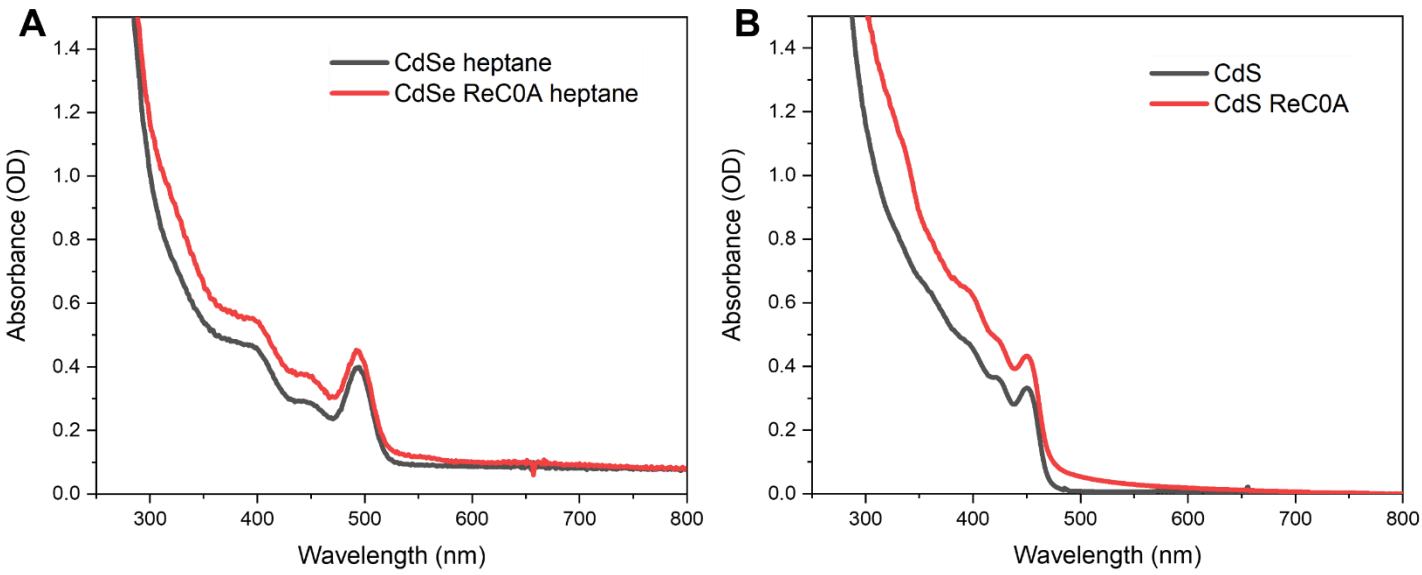

Figure S3.4. UV-Vis spectra of A) CdSe and CdSe-ReC0A (in heptane) and B) CdS (in $CHCl_3$) and CdS-ReC0A (in heptane).

3.4.4 TA Spectra of ReC0A + TEOA and QD + Methyl Viologen

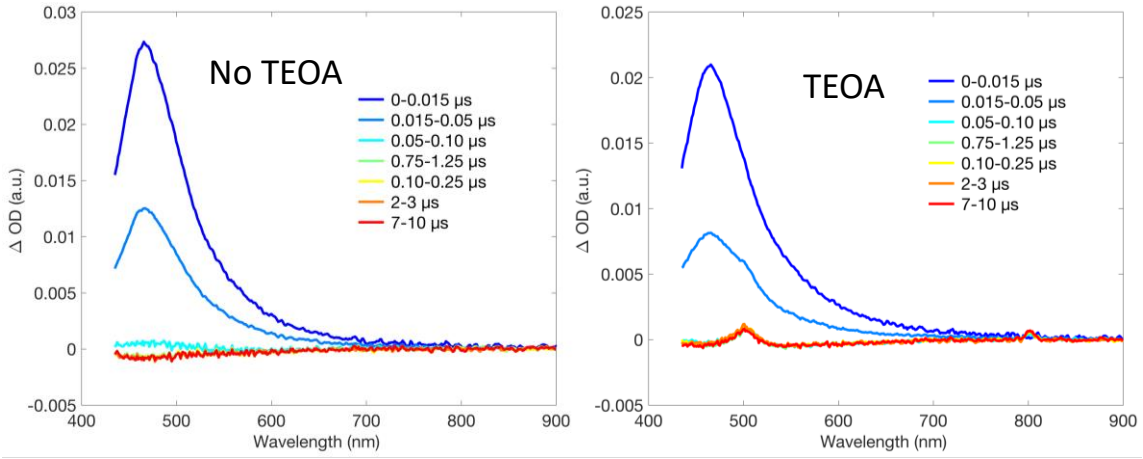

Figure S3.5. Nanosecond TA spectra of ReCl with and without TEOA. Upon excitation of the MLCT state at 400 nm, we observe the decay of the excited state (left). Once TEOA is added and the sample excited, the excited MLCT decays and at approximately 50-100 ns, a small absorption corresponding to the reduced ReCl species appears around 510 nm (right panel).

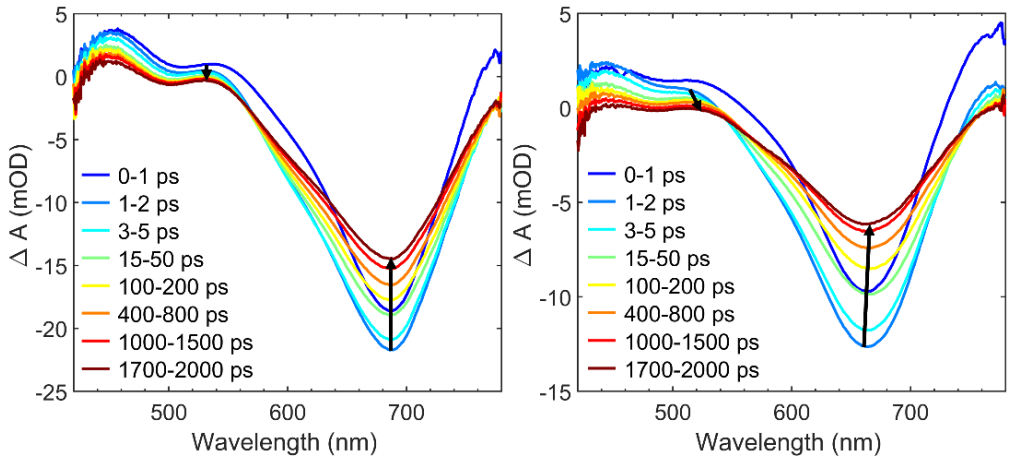

Figure S3.6. Cd_3P_2 without (left) and with (right) methyl viologen. After excitation with 400 nm pump of the QD-methyl viologen sample, there is a red shift of both the photoinduced absorption around 500 nm and the bleach at 680 nm. This is due to the growth of the charge separated state.

3.4.5 Transient IR Spectra of ReC0A on Cd_3P_2

We performed transient IR (TRIR) experiments using 500 nm and 600 nm pump light, both outside of the ReC0A absorption range, and used ~ 2000 cm^{-1} centered broadband probe. The results show the ReC0A does indeed receive an electron from the Cd_3P_2, and at an ultrafast rate (Figure S3.7). The reduced Re species peak appears at a frequency ~20 cm^{-1} lower than that of the original species' bleach and within a 300 fs delay time. Others have also reported an ultrafast electron transfer, but have not speculated on the cause.[54]

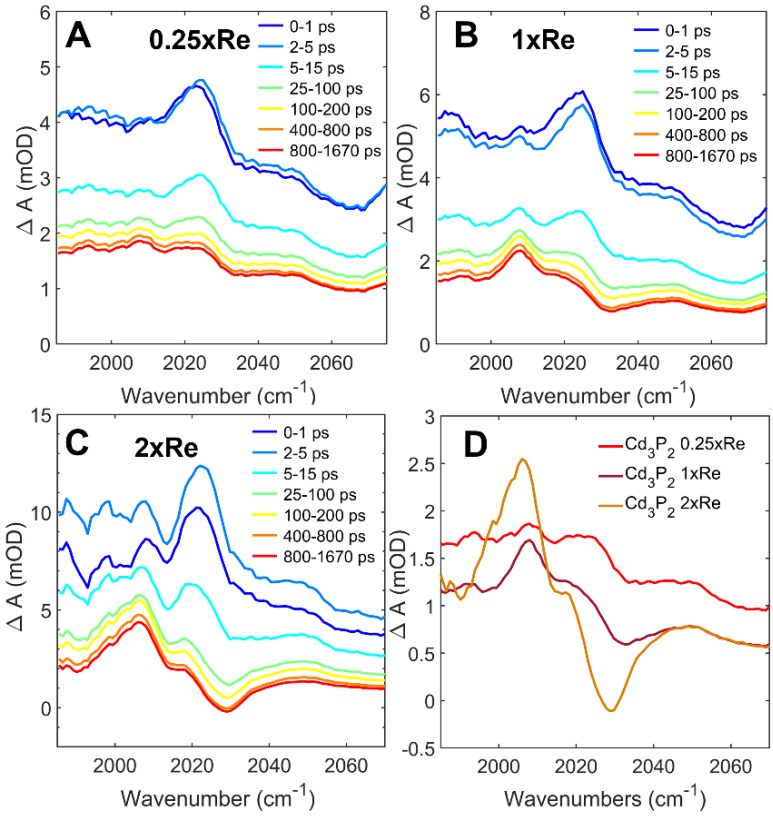

Figure S3.7. Transient IR spectra of ReC0A on Cd_3P_2 pumped with 500 nm at very high pump fluence showing that the Fano resonance signal forms almost immediately withing 0-1 ps. The offset is due to the excited electron signal in the quantum dot. A) Cd_3P_2-0.25xRe shows only a positive feature at 2025 cm^{-1} corresponding to the Fano resonance signal. B) Cd_3P_2-1xRe where Fano resonance can also be observed at early time, however, at ~2005 cm^{-1} there is a small absorption

corresponding to the growth of the reduced ReC0A species. At later time, as the FR decays, that absorption becomes more pronounce and the ground state blaech of the complex is also observed at 2029 cm^{-1}. C) Cd_3P_2-2xRe. Similar features are observed here as part B, however, the decay of the FR is faster due to more ReC0A on the QD surface and there is also a larger reduced ReC0A signal corresponding to more reduced complex. D) Latest time delay (800-1670 ps) spectra overlayed for each sample after scaling 1x and 2xRe early time amplitudes to 0.25xRe data. As more ReC0A is added to the QD surface, there is more reduced ReC0A that appears faster.

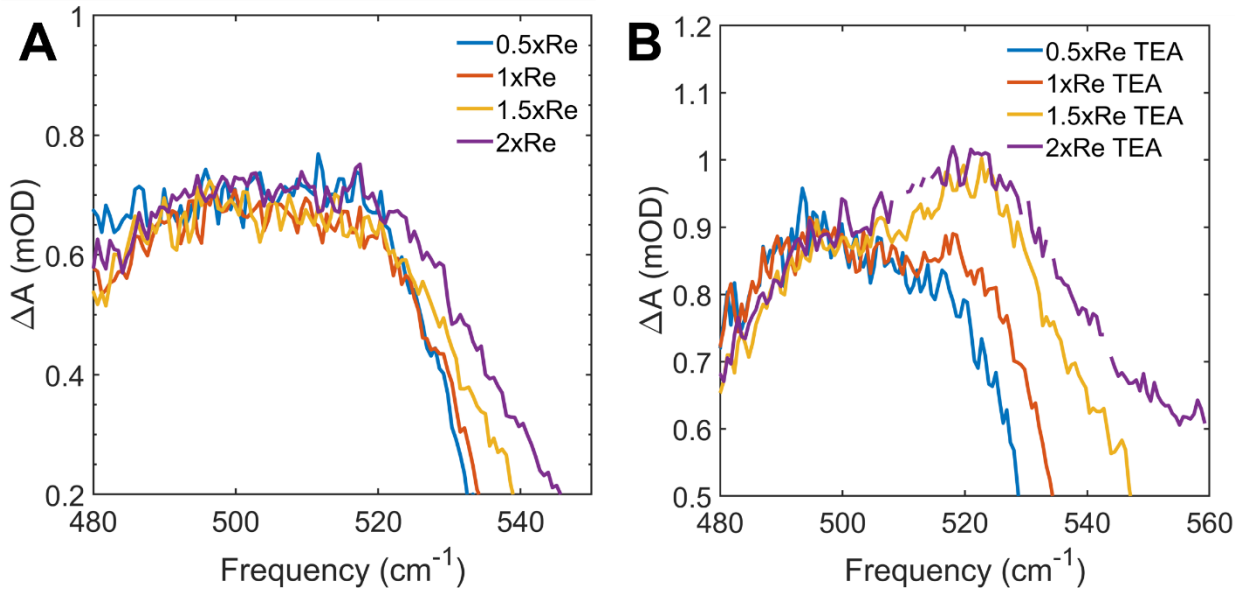

Figure S3.8. (A) and (B) show TA spectra at 1000-1670 ps for samples of each ReC0A concentration without and with TEA, respectively, zoomed into the 520 nm peak corresponding to reduced ReC0A seen in Figures 3.6c and 3.7c. Upon addition of TEA and faster bleach recovery, the reduced ReC0A signal becomes more visible.

3.4.6 Loss of Bleach Amplitude

The loss of bleach amplitude we observe is most likely due to defect states as a result of OA

likely being replaced upon ReC0A adsorption and ultrafast ET. With regards to the ultrafast ET, we can compare the unnormalized bleach amplitudes for Cd_3P_2 and Cd_3P_2-ReC0A at three different pump wavelengths: 400, 560, and 700 nm. Pumping at higher energy (400 and 560 nm) shows a bleach amplitude loss of almost half, while at 700 nm excitation, the bleach amplitude is essentially the same for both samples. Both 400 and 560 nm pumps are at higher energy than the QD CB edge, so ultrafast ET is more likely to occur, whereas, at 700 nm, the same energy as the QD exciton band, there is most likely direct excitation to the CB edge. These results along with our hypothesis that electron trapping due to ReC0A adsorption occurs likely both contribute to the loss in bleach amplitude.

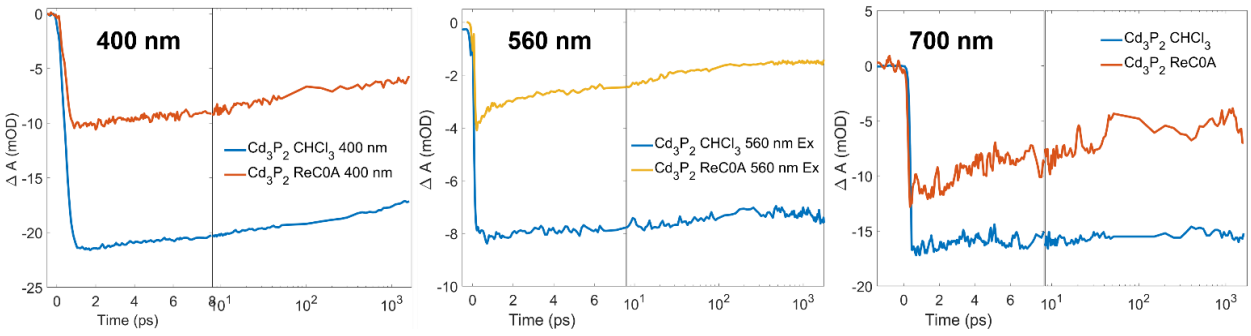

Figure S3.9. Unnormalized kinetics of Cd_3P_2 and Cd_3P_2-ReC0A at A) 400 nm, B) 560 nm, and C) 700 nm excitation. The higher energy pump wavelengths result in ultrafast electron transfer due to exciting much higher than the conduction band edge, while pumping at 700 nm likely results in direct band edge excitation.

3.4.7 TA Spectra of Cd_3P_2 and Different Concentrations of ReC0A on Cd_3P_2 with and without TEA

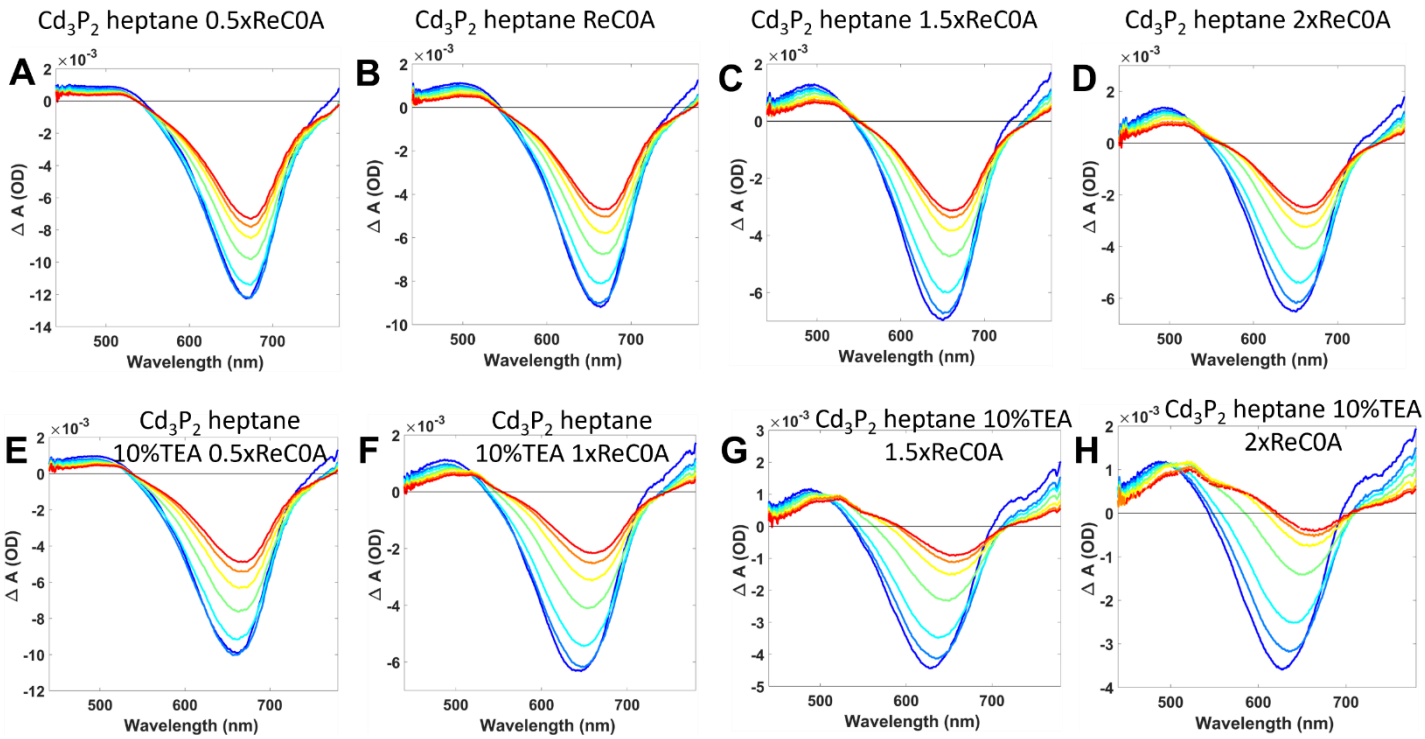

Figure S3.10. Transient absorption spectra of (A) 0.5xReC0A on Cd_3P_2, (B) 1xReC0A on Cd_3P_2, (C) 1.5xReC0A on Cd_3P_2, (D) 2xReC0A on Cd_3P_2 in heptane, and of (E) 0.5xReC0A on Cd_3P_2 with 10%TEA, (E) 1xReC0A on Cd_3P_2 with 10%TEA, (G) 1.5xReC0A on Cd_3P_2 with 10%TEA, (H) 2xReC0A on Cd_3P_2 with 10%TEA all in heptane. [Legend: dark blue: 0-2 ps; blue: 2-5 ps; light blue: 5-15 ps; green: 25-75 ps; yellow: 100-300 ps; orange: 500-800 ps; red: 1000-1670 ps;]

The top four panels of Figure S3.10 show the evolution of TA spectra over time for the various concentrations of ReC0A on the Cd_3P_2 in heptane. As more ReC0A is added, the band blue shifts. While a blue shift often occurs from degradation of the QD, our TEM data shows that degradation is not occurring, as the size is slightly larger with the ReC0A. The bottom four panels show the same exciton bands after addition of 10% TEA. They show an even further blue shift. In both sets of panels,

the 1.5x and 2x ReC0A concentrations show a clear charge separated state emerging over time with a derivative shape, the positive feature approximately between 400 nm and 650 nm and a negative feature between 650 nm and 720 nm.

3.4.8 TA Spectra of Cd_3P_2 + ReC0A with Different Concentrations of TEA

We performed TA experiments of Cd_3P_2-0.5xReC0A with varying concentrations of TEA to observe the effect on ET. We found that as you increase TEA concentration, ET also increases, shown in the figure below.

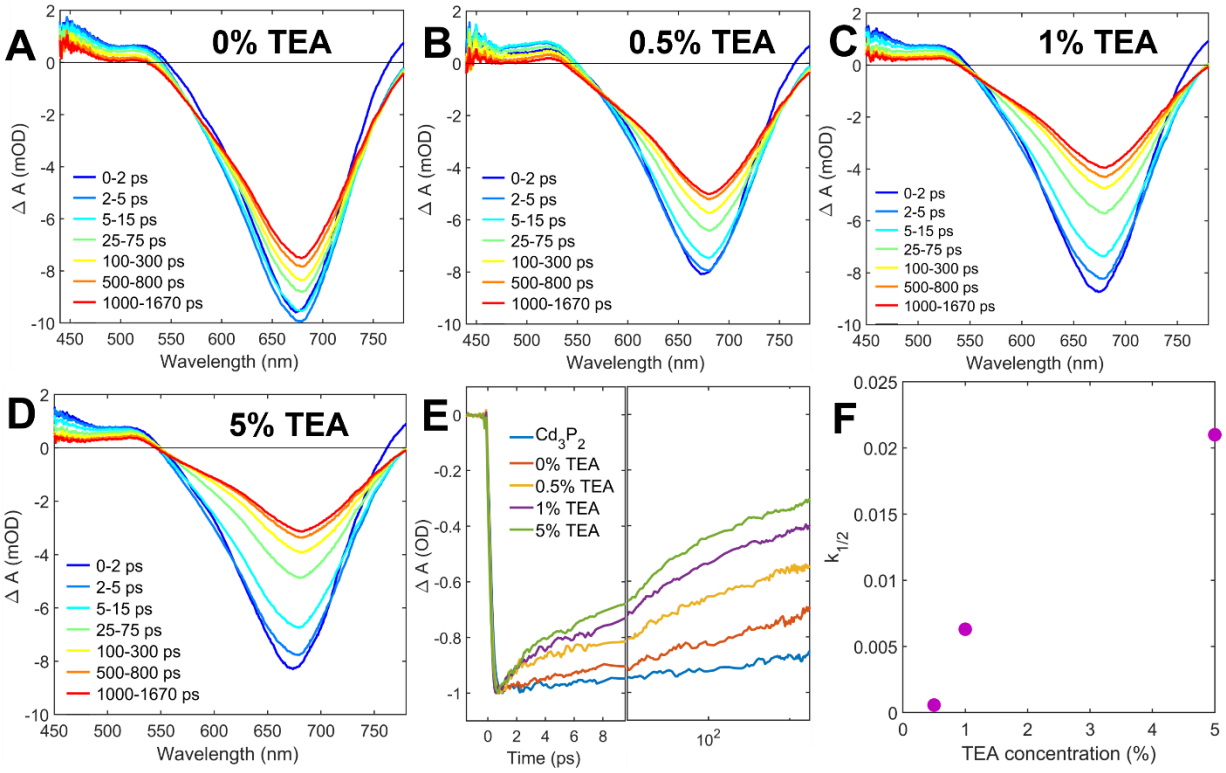

Figure S3.11. TA spectra with varying concentrations of TEA (by volume) with constant ReC0A concentration held at 0.5xRe (0.28mM) bound to Cd_3P_2. A) 0% TEA (Cd_3P_2-0.5xReC0A), B) 0.5% TEA, C) 1% TEA, D) 5% TEA, E) kinetics for each of these samples including Cd_3P_2 only, and F) plot of half-life with increasing TEA concentration.

3.4.9 Time Correlated Single Photon Counting

The absorption and fluorescence spectra were taken of the Cd_3P_2 (Figure S3.12a). The fluorescence spectrum was used to determine a suitable wavelength for collection for time-correlated single photon counting experiments, which were conducted using 400 nm to excite and detected at 780 nm. Time-correlated single photon counting experiments were performed with various concentrations of TEA, showing that at less than or equal to 17.7 mM, the TEA slightly enhanced the fluorescence (Figure 3.12b), and at concentrations that were higher, the TEA behaved as a hole scavenger (Figure S3.12c), quenching the photoluminescence.

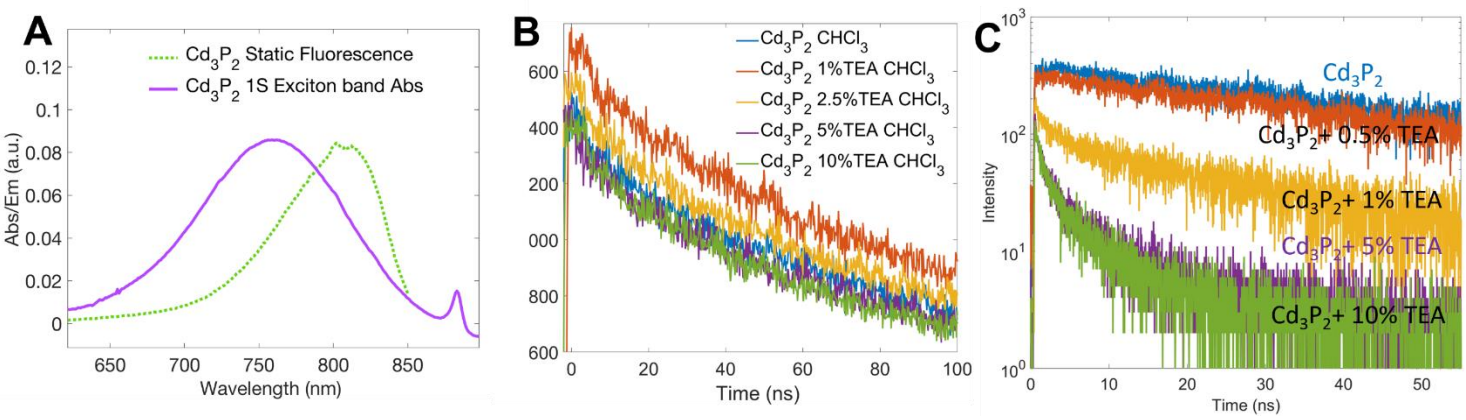

Figure S3.12. A) UV-Vis and Fluorescence of Cd_3P_2 in $CHCl_3$, B) TCSPC of Cd_3P_2 with varying low concentrations of TEA (in order: 7.1 mM, 17.7 mM, 35.5 mM, and 70.9 mM) and C) TCSPC of Cd_3P_2 with varying high concentrations of TEA.

3.4.10 ^{1}H NMR and DOSY of Cd_3P_2 and TEA

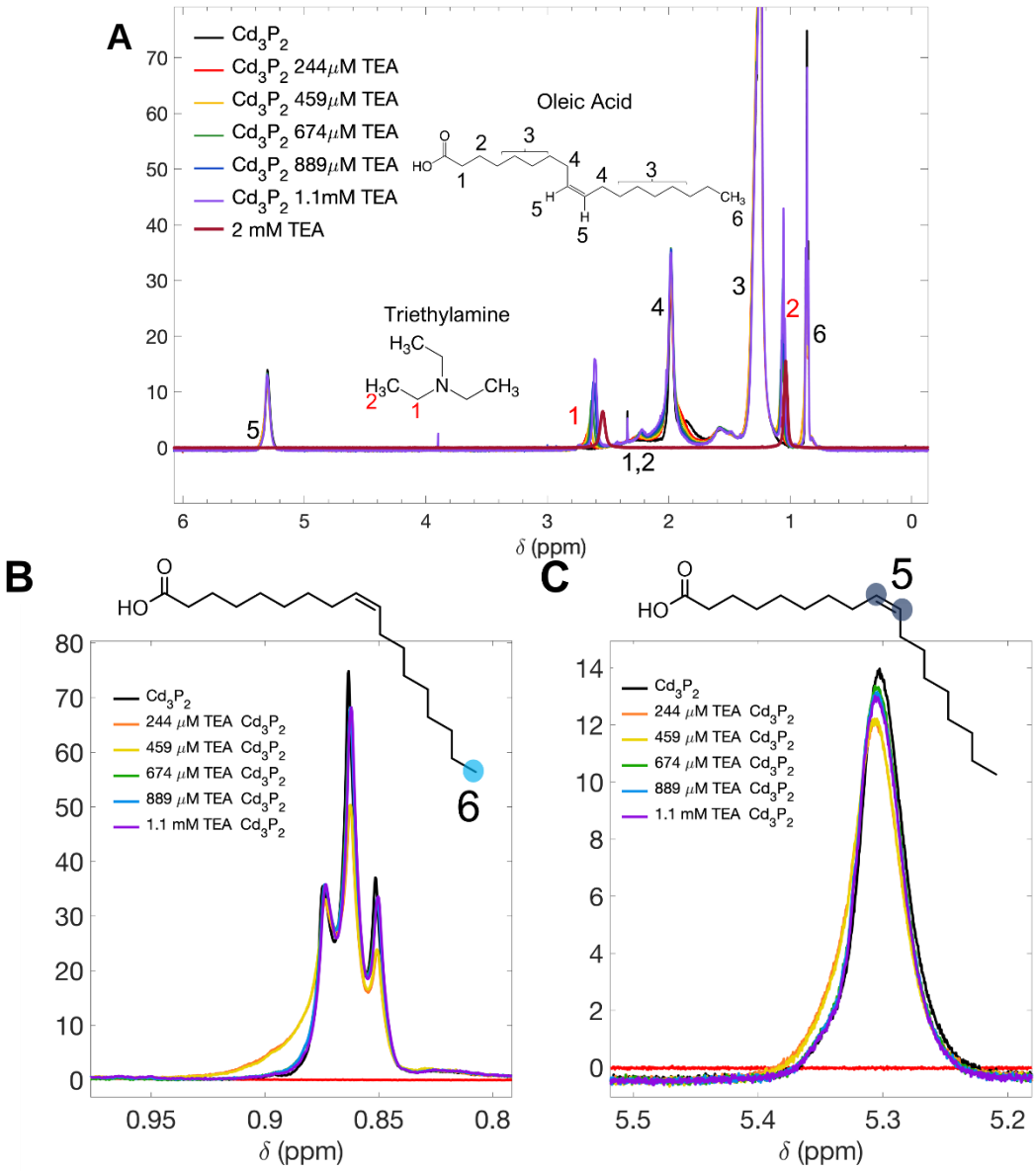

Figure S3.13. A) NMR spectra of Cd_3P_2 in $CDCl_3$ with varying concentrations of TEA B) CH_3 Oleic acid peaks and C) CH_2 Oleic acid peaks show broadening with addition of low concentrations of TEA and return to original peak width with higher concentrations.

Samples were prepared by rotary evaporating the Cd_3P_2, chloroform, and redissolving in $CDCl_3$ obtained from Sigma Aldrich (99.96% D atom). The concentration of the QD was calculated

to be ~ 25 μM and varying concentrations, from 259 μM to 1.1 mM of TEA in $CDCl_3$ were added to the sample for the titration. For ^1H NMR studies, a Bruker Ascend 600 MHz spectrometer was used (frequency: 600.18 MHz). It also included a prodigy cryoprobe that was cooled with liquid nitrogen. Figure S3.13 shows H NMR spectra of Cd_3P_2 in $CDCl_3$ with various amounts of TEA added.

DOSY NMR was performed on the same instrument described above with a TEA concentration of 459 μM (second lowest concentration). A gradient was applied increasing from 2 to 95% with 25 points taken. These points were then fit to the following equation to obtain the diffusion coefficient:

$$I = I_0 e^{-(\gamma g \delta)^2 * D(\Delta - \frac{\delta}{3})} \quad \text{Eq. 1}$$

where I is the intensity, I_0 is the intensity at zero gradient strength, γ is the gyromagnetic ratio, g is the gradient strength, δ and Δ are the delays between pulses, and D is the diffusion coefficient.[55]

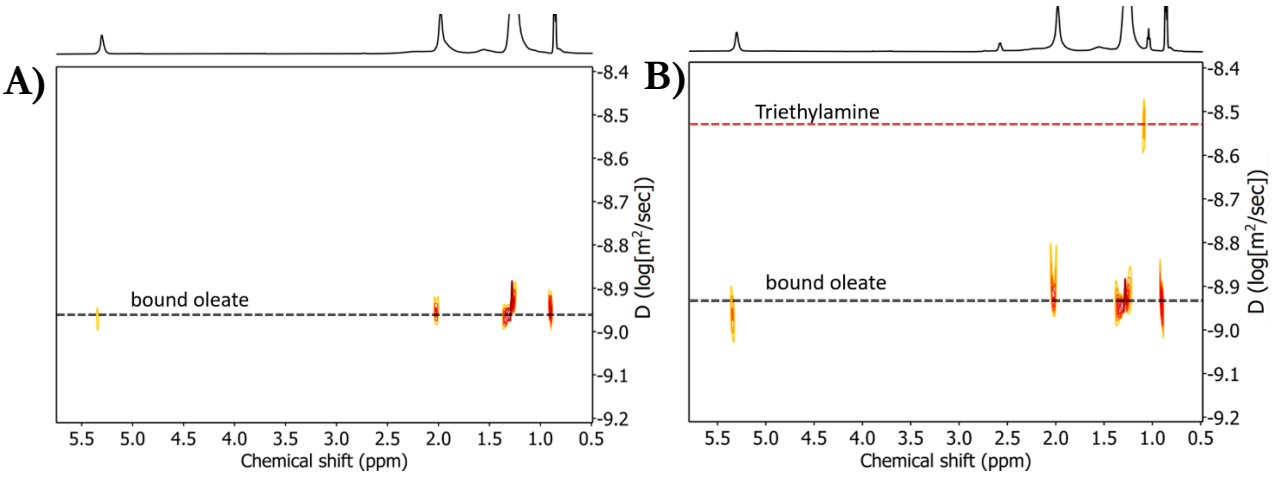

Figure S3.14. DOSY NMR spectra of a) Cd_3P_2 and b) Cd_3P_2 with TEA.

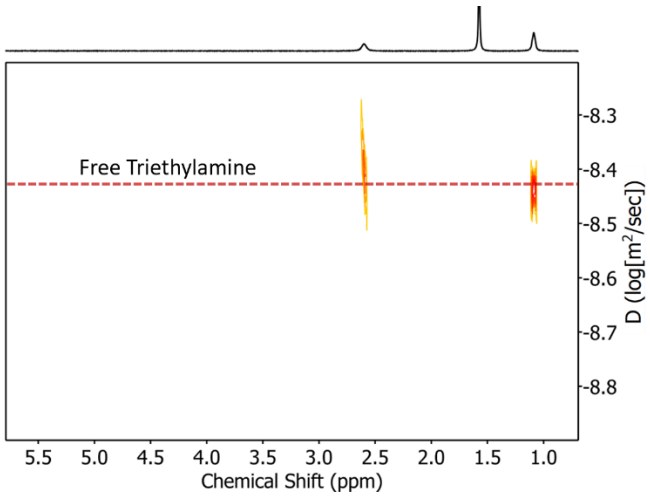

Figure S3.15. DOSY NMR spectra of TEA in $CDCl_3$ provides a diffusion coefficient of 3.62 $\mu m^2/s$.

3.4.11 Cyclic Voltammetry of ReC0A and TEA

CV experiments were conducted on $Re(bpy)(CO)_3Cl$ (ReCl) in MeCN as a control. The first reduction of ReCl remains the same (-1.16 vs NHE) regardless of TEA's presence in solution and there is no appearance of a peak between the first and second reduction of the complex.

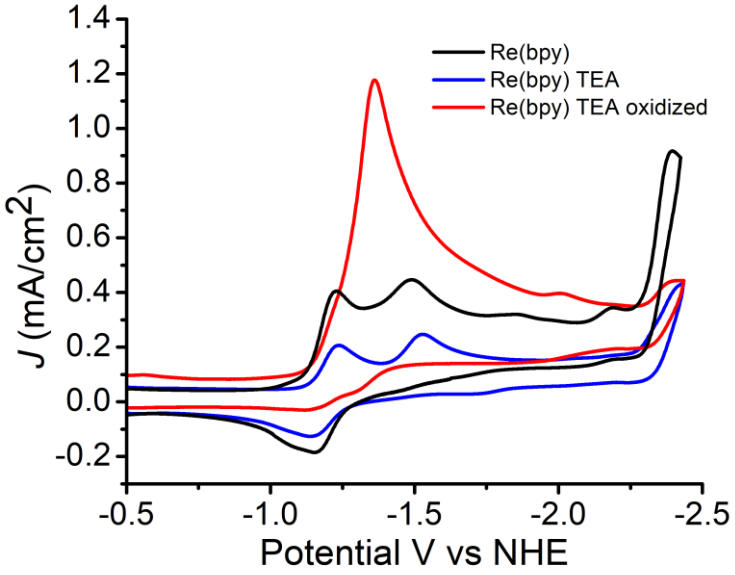

Figure S3.16. Cyclic voltammogram of $Re(bpy)(CO)_3Cl$ with and without TEA.

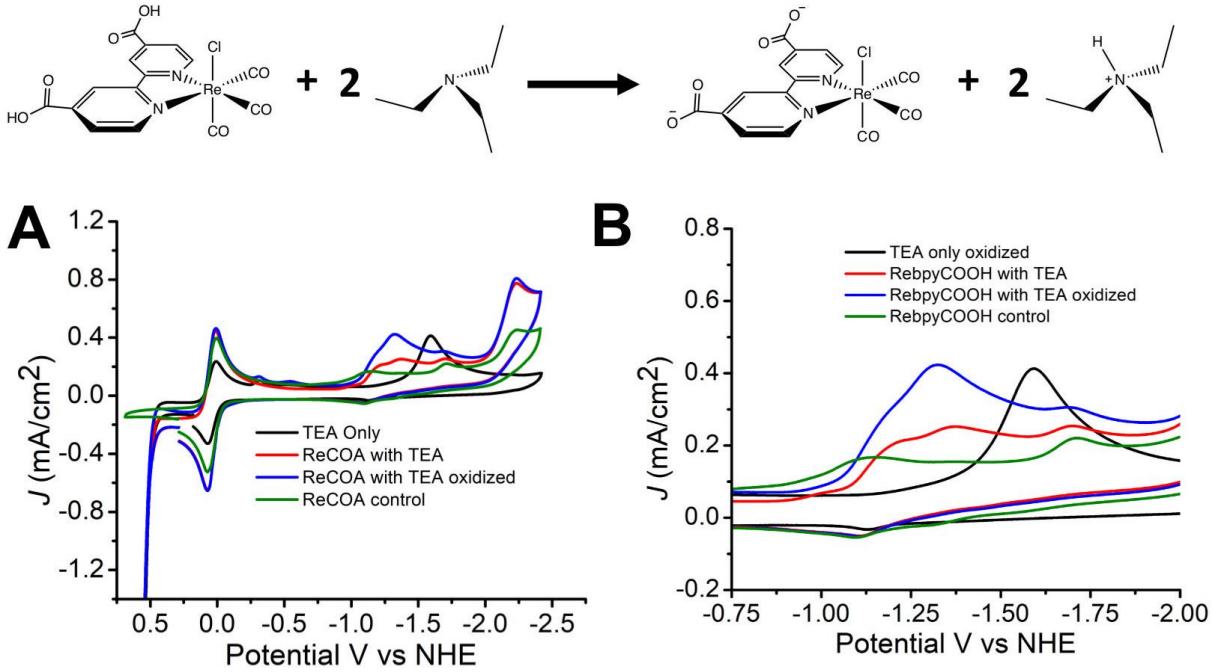

Figure S3.17. (A) CV curves for TEA, ReC0A, ReC0A + TEA and ReC0A + TEA with TEA oxidized first, (B) zoomed in region of the curves in (A).

To determine if the small peak in the ReC0A electrochemistry was from the reduction of $TEAH^+$, TEA oxidation and reduction was studied electrochemically. In a solution with TEA and no catalyst, there were not visible reduction peaks when scanning between 0.4 V and -2.0 V vs NHE. When the solution is scanned past 0.5 V vs NHE, there is a large increase in current corresponding to the oxidation of TEA. In the same scan, the reduction of $TEAH^+$ is now present at -1.56 V vs NHE. In the presence of ReCl, the oxidation of TEA is unchanged but, when the oxidation is followed by scanning cathodically, the reduction of TEA shifts positively to -1.34 V vs NHE. When this experiment is run in the presence of ReC0A, the reduction of the $TEAH^+$ appears at -1.29 V vs NHE, similar to the small peak seen in the TEA plus ReC0A solution. From this, we conclude that the change in the first reduction of the ReC0A upon addition of TEA and the appearance of a new reduction peak, is due to the deprotonation of the carboxylic acid on the bpy ligand.

3.4.12 Kinetics of QDs and Electron Acceptors with and without TEA

To study if the increased electron transfer rate after adding TEA was generalizable, we tested multiple QD-electron acceptor systems with and without TEA, in multiple solvents. Figure S3.18, shows that this is indeed the case. We studied CdSe in heptane with ReC0A bound, CdS in $CHCl_3$ with ReC0A bound and CdS in $CHCl_3$ with methyl viologen ($[MV]^{2+}$) in solution. Each of them shows an enhanced electron transfer rate upon the addition of 10% (v/v) TEA. All samples were excited with 400 nm light.

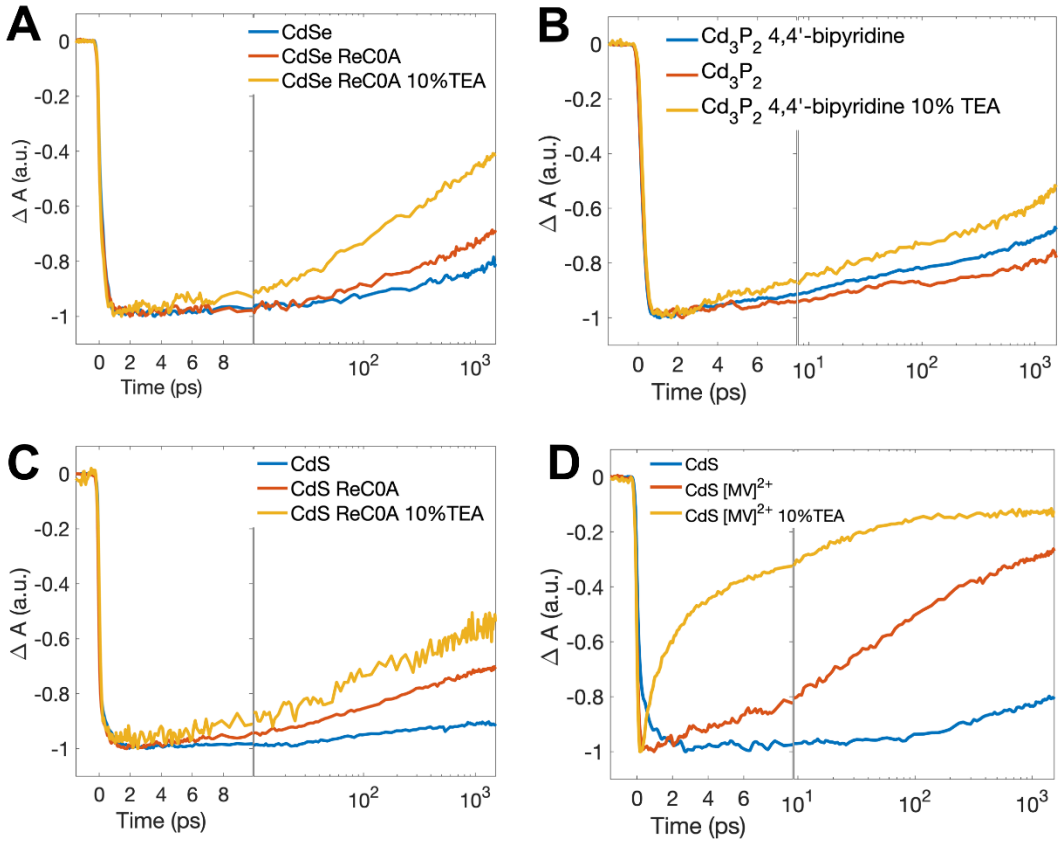

Figure S3.18. Normalized kinetic traces of different quantum dots, ReC0A bound, and TEA added, showing increased electron transfer with the addition of the hole scavenger A) CdSe, CdSe-ReC0A, CdSe-ReC0A-TEA B) Cd_3P_2, Cd_3P_2-4,4'-bipyridine, Cd_3P_2-4,4'-bipyridine-TEA C) CdS, CdS-ReC0A, CdS-ReC0A-TEA D) CdS, CdS-MV^{2+}, CdS-MV^{2+}-TEA.

3.4.13 *Ab initio* Method Details

Gaussian 16 version A.03[7] and Vienna Ab initio Simulation Packages (VASP) version 5.4.1[8-11] were used to on all density functional theory (DFT) calculations. The Vaspkit[12] program was used to calculate the work function and Jmol[13] was used for visualization.

Gaussian was used for ReC0A geometry optimizations and frequency calculations, which were performed using the (U)B3LYP functional[14-16] with the 6-311+G(2df,p) basis sets[17-25] on all non-

metallic atoms and the def2-TZVP effective core potential and basis set[26-27] on the Re atom. for geometry optimization and frequency calculations. Scale factor 0.965 was applied to all frequency calculation results reported in this article.

VASP was used for optimizations of Cd_3P_2 unit cell, Cd_3P_2 slab, Cd_3P_2 slab with capping agent, and Cd_3P_2 slab with capping agent & ReC0A. The electron–ion interactions were described by the Perdew–Burke–Ernerhof (PBE) exchange-correlation functional[28] and the projected augmented-wave (PAW) method[29-30]. The Gaussian smearing method with a smearing parameter $\sigma = 0.1$ eV was applied for all the calculations. The DFT-D3 method with the Becke-Jonson damping[31-32] was used to describe dispersion interactions. The plane wave basis set was cutoff at 400 eV and the energy convergence criterion was set to be 10^{-6} eV per unit cell. A Monckhorst–Pack[33] (MP) type k-point grid of $9 \times 9 \times 9$ was used for the optimization of Cd_3P_2 unit cell; an MP type k-point grid of $3 \times 3 \times 1$ was used for the optimization of Cd_3P_2 slabs (with and without capping agents); an MP type k-point grid of $1 \times 1 \times 1$ was used for the optimization of Cd_3P_2 slab with capping agents and ReC0A. The capping agents were modeled as formic acid. During structure optimization, the Cd_3P_2 unit cell's atom position, cell shape and cell volume were allowed to relax; for Cd_3P_2 slabs, Cd_3P_2 slabs with capping agents, and Cd_3P_2 slabs with capping agent & ReC0A only atom positions were allowed to relax. However, atoms in the bottom half of Cd_3P_2 slabs were frozen at their bulk positions. Both ReC0A binding geometries were optimized with the same unit cell and number of molecules. For the single carboxylic acid case, the ReC0A was optimized from a monodentate structure. In the case of dicarboxylic acid binding, the complex was optimized from a bidentate structure. The stable (100) facet of Cd_3P_2 was selected as the exposed surface to model Cd_3P_2 quantum dots. For all Density of State (DOS) calculation, the Heyd-Scuseria-Ernzerhof (HSE) screened hybrid functional[34] was applied. Considering the size of the model, a MP type k-point grid of $1 \times 1 \times 1$ was applied.

3.4.14 Quantum Dot Area Calculation

In experiments, the QD diameter is 3.1 nm and the QD concentration is 25 μM. From the simulation model, we estimated for both ReC0A's carboxyl functional group to be bound on the QD surface, the minimum surface area require is 1.06 nm^2 per ReC0A molecule. The experimental QD's surface area is 30.19 nm^2, thus about 28.5 (31.19 nm^2/1.06 nm^2) ReC0A molecules can be adsorbed on the QD through both carboxyl groups. If the number of ReC0A molecules is more than 28.5 per QD, some of them can only have single carboxyl bound to the surface, with the second carboxyl group protonated and pointed away from QD. For a solution with 25 μM QD, the critical concentration for ReC0A to change its surface binding mode from double carboxylate to single carboxylate will be 0.71 (28.48*25 μM* 1/1000 mM/μM) mM, which is within the same range of experimental concentrations to see the disappearance of the 1700 cm^{-1} peak. The maximum effective concentration of surface protons should be 2.84 mM (4 times site number compared to ReC0A binding site).

3.5 References

1. Morris, A. J.; Meyer, G. J.; Fujita, E., Molecular Approaches to the Photocatalytic Reduction of Carbon Dioxide for Solar Fuels. *Accounts of Chemical Research* **2009,** *42* (12), 1983-1994.
2. Grills, D. C.; Fujita, E., New Directions for the Photocatalytic Reduction of CO2: Supramolecular, scCO(2) or Biphasic Ionic Liquid-scCO(2) Systems. *Journal of Physical Chemistry Letters* **2010,** *1* (18), 2709-2718.
3. Benson, E. E.; Kubiak, C. P.; Sathrum, A. J.; Smieja, J. M., Electrocatalytic and homogeneous approaches to conversion of CO2 to liquid fuels. *Chemical Society Reviews* **2009,** *38* (1), 89-99.
4. Dabbousi, B. O.; RodriguezViejo, J.; Mikulec, F. V.; Heine, J. R.; Mattoussi, H.; Ober, R.; Jensen, K. F.; Bawendi, M. G., (CdSe)ZnS Core-Shell Quantum Dots: Synthesis and Characterization of a Size Series of Highly Luminescent Nanocrystallites. *Journal of Physical Chemistry B* **1997,** *101* (46), 9463-9475.
5. Talapin, D. V.; Haubold, S.; Rogach, A. L.; Kornowski, A.; Haase, M.; Weller, H., A Novel Organometallic Synthesis of Highly Luminescent CdTe Nanocrystals. *Journal of Physical Chemistry B* **2001,** *105* (12), 2260-2263.
6. Wu, K. F.; Lian, T. Q., Quantum confined colloidal nanorod heterostructures for solar-to-fuel conversion. *Chemical Society Reviews* **2016,** *45* (14), 3781-3810.
7. Alivisatos, A. P., Semiconductor clusters, nanocrystals, and quantum dots. *Science* **1996,** *271* (5251), 933-937.
8. Smith, A. M.; Nie, S. M., Semiconductor Nanocrystals: Structure, Properties, and Band Gap Engineering. *Accounts of Chemical Research* **2010,** *43* (2), 190-200.
9. Jasieniak, J.; Califano, M.; Watkins, S. E., Size-Dependent Valence and Conduction Band-Edge Energies of Semiconductor Nanocrystals. *Acs Nano* **2011,** *5* (7), 5888-5902.
10. Wu, K. F.; Liu, Z.; Zhu, H. M.; Lian, T. Q., Exciton Annihilation and Dissociation Dynamics in Group II-V Cd3P2 Quantum Dots. *Journal of Physical Chemistry A* **2013,** *117* (29), 6362-6372.
11. Vlcek, A., Ultrafast Excited-State Processes in Re(I) Carbonyl-Diimine Complexes: From Excitation to Photochemistry. In *Photophysics of Organometallics*, Vol. 29, pp 73-114.
12. Agarwal, J.; Fujita, E.; Schaefer, H. F.; Muckerman, J. T., Mechanisms for CO Production from CO_2 Using Reduced Rhenium Tricarbonyl Catalysts. *Journal of the American Chemical Society 134* (11), 5180-5186.
13. Hawecker, J.; Lehn, J. M.; Ziessel, R., Efficient Photochemical Reduction of CO_2 to CO by Visible Light Irradiation of Systems Containing $Re(bipy)(CO)_3X$ or $Ru(bipy)_3^{2+}$-Co^{2+} Combinations as Homogeneous Catalysts. *Journal of the Chemical Society-Chemical Communications* **1983,** (9), 536-538.
14. Kutal, C.; Weber, M. A.; Ferraudi, G.; Geiger, D., A Mechanistic Investigation of the Photoinduced Reduction of Carbon Dioxide Mediated by Tricarbonylbromo(2,2'-bipyridine)rhenium(I). *Organometallics* **1985,** *4* (12), 2161-2166.
15. Kutal, C.; Corbin, A. J.; Ferraudi, G., Further Studies of the Photoinduced Reduction of Carbon Dioxide Mediated by Tricarbonylbromo(2,2'-bipyridine)rhenium(I). *Organometallics* **1987,** *6* (3), 553-557.
16. Takeda, H.; Koike, K.; Inoue, H.; Ishitani, O., Development of an efficient photocatalytic system for CO2 reduction using rhenium(l) complexes based on mechanistic studies. *Journal of the American Chemical Society* **2008,** *130* (6), 2023-2031.
17. Kutal, C.; Corbin, A. J.; Ferraudi, G., Further-Studies Of The Photoinduced Reduction Of Carbon-Dioxide Mediated By Tricarbonylbromo(2,2'-Bipyridine)Rhenium(I). *Organometallics* **1987,** *6* (3), 553-557.

18. Bullen, C.; Mulvaney, P., The effects of chemisorption on the luminescence of CdSe quantum dots. *Langmuir* **2006,** *22* (7), 3007-3013.
19. Nose, K.; Fujita, H.; Omata, T.; Otsuka-Yao-Matsuo, S.; Nakamura, H.; Maeda, H., Chemical role of amines in the colloidal synthesis of CdSe quantum dots and their luminescence properties. *Journal of Luminescence* **2007,** *126* (1), 21-26.
20. Landes, C.; Burda, C.; Braun, M.; El-Sayed, M. A., Photoluminescence of CdSe Nanoparticles in the Presence of a Hole Acceptor: n-butylamine. *Journal of Physical Chemistry B* **2001,** *105* (15), 2981-2986.
21. Morgan, D. P.; Kelley, D. F., Mechanism of Hole Trap Passivation in CdSe Quantum Dots by Alkylamines. *Journal of Physical Chemistry C* **2018,** *122* (44), 25661-25667.
22. Kornowski, A.; Eichberger, R.; Giersig, M.; Weller, H.; Eychmuller, A., Preparation and photophysics of strongly luminescing Cd3P2 quantum dots. *Journal of Physical Chemistry* **1996,** *100* (30), 12467-12471.
23. Yu, W. W.; Qu, L. H.; Guo, W. Z.; Peng, X. G., Experimental Determination of the Extinction Coefficient of CdTe, CdSe, and CdS Nanocrystals. *Chemistry of Materials* **2003,** *15* (14), 2854-2860.
24. Green, M.; O'Brien, P., The Synthesis of Cadmium Phosphide Nanoparticles Using Cadmium Diorganophosphide Precursors. *Journal of Materials Chemistry* **1999,** *9* (1), 243-247.
25. Linchung, P. J., Energy Band Structures of Cd_3P_2 and Zn_3P_2. *Physica Status Solidi B-Basic Research* **1971,** *47* (1), 33-&.
26. Wang, R. B.; Ratcliffe, C. I.; Wu, X. H.; Voznyy, O.; Tao, Y.; Yu, K., Magic-Sized Cd3P2 II-V Nanoparticles Exhibiting Bandgap Photoemission. *Journal of Physical Chemistry C* **2009,** *113* (42), 17979-17982.
27. Fischer, A. B.; Bronstein-Bonte, I., Photoinduced Electron Transfer Quenching of Rhodamine B in Polymer Films. *Journal of Photochemistry* **1985,** *30* (4), 475-485.
28. Qiao, J. L.; Liu, Y. Y.; Hong, F.; Zhang, J. J., A review of catalysts for the electroreduction of carbon dioxide to produce low-carbon fuels. *Chemical Society Reviews* **2014,** *43* (2), 631-675.
29. Brus, L. E., A Simple-Model of the Ionization-Potential, Electron-Affinity, and Aqueous Redox Potentials of Small Semiconductor Crystallites. *Journal of Chemical Physics* **1983,** *79* (11), 5566-5571.
30. Bawendi, M. G.; Steigerwald, M. L.; Brus, L. E., The Quantum-Mechanics of Larger Semiconductor Clusters (Quantum Dots). *Annual Review of Physical Chemistry* **1990,** *41*, 477-496.
31. Steigerwald, M. L.; Brus, L. E., Semiconductor Crystallites - A Class of Large Molecules. *Accounts of Chemical Research* **1990,** *23* (6), 183-188.
32. Guyot-Sionnest, P.; Wehrenberg, B.; Yu, D., Intraband Relaxation in CdSe Nanocrystals and the Strong Influence of the Surface Ligands. *Journal of Chemical Physics* **2005,** *123* (7).
33. Laaser, J. E.; Christianson, J. R.; Oudenhoven, T. A.; Joo, Y.; Gopalan, P.; Schmidt, J. R.; Zanni, M. T., Dye Self-Association Identified by Intermolecular Couplings between Vibrational Modes As Revealed by Infrared Spectroscopy, and Implications for Electron Injection. *Journal of Physical Chemistry C* **2014,** *118* (11), 5854-5861.
34. Kiefer, L. M.; Kubarych, K. J., Solvent-Dependent Dynamics of a Series of Rhenium Photoactivated Catalysts Measured with Ultrafast 2DIR. *Journal of Physical Chemistry A* **2015,** *119* (6), 959-965.
35. Westmoreland, D. E.; López-Arteaga, R.; Weiss, E. A., N-Heterocyclic Carbenes as Reversible Exciton-Delocalizing Ligands for Photoluminescent Quantum Dots. *Journal of the American Chemical Society* **2020,** *142* (5), 2690-2696.
36. Oudenhoven, T. A.; Joo, Y.; Laaser, J. E.; Gopalan, P.; Zanni, M. T., Dye aggregation identified by vibrational coupling using 2D IR spectroscopy. *Journal of Chemical Physics* **2015,** *142* (21).

37. Keith, J. A.; Grice, K. A.; Kubiak, C. P.; Carter, E. A., Elucidation of the selectivity of proton-dependent electrocatalytic CO2 reduction by fac-Re(bpy)(CO)3Cl. *J. Am. Chem. Soc.* **2013,** *135* (42), 15823-15829.
38. Diaz-Torres, R.; Alvarez, S., Coordinating Ability of Anions and Solvents Towards Transition Metals and Lanthanides. *Dalton Transactions* **2011,** *40* (40), 10742-10750.
39. Sharma, S. N.; Sharma, H.; Singh, G.; Shivaprasad, S. M., Studies of Interaction of Amines with TOPO/TOP Capped CdSe Quantum Dots: Role of Crystallite Size and Oxidation Potential. *Materials Chemistry and Physics* **2008,** *110* (2-3), 471-480.
40. Galian, R. E.; Scaiano, J. C., Fluorescence quenching of CdSe quantum dots by tertiary amines and their surface binding effect. *Photochemical & Photobiological Sciences* **2009,** *8* (1), 70-74.
41. Huang, J. E.; Huang, Z. Q.; Jin, S. Y.; Lian, T. Q., Exciton Dissociation in CdSe Quantum Dots by Hole Transfer to Phenothiazine. *Journal of Physical Chemistry C* **2008,** *112* (49), 19734-19738.
42. Dannhauser, T.; Oneil, M.; Johansson, K.; Whitten, D.; McLendon, G., Photophysics Of Quantized Colloidal Semiconductors Dramatic Luminescence Enhancement By Binding Of Simple Amines. *Journal of Physical Chemistry* **1986,** *90* (23), 6074-6076.
43. Bagno, A.; Scorrano, G.; Stiz, S., Preferential Solvation of Neutral Species in Binary Solvent Mixtures Characterized by H-1 NOESY NMR Spectroscopy. *Journal of the American Chemical Society* **1997,** *119* (9), 2299-2300.
44. De Roo, J.; Yazdani, N.; Drijvers, E.; Lauria, A.; Maes, J.; Owen, J. S.; Van Driessche, I.; Niederberger, M.; Wood, V.; Martins, J. C.; Infante, I.; Hens, Z., Probing Solvent-Ligand Interactions in Colloidal Nanocrystals by the NMR Line Broadening. *Chemistry of Materials* **2018,** *30* (15), 5485-5492.
45. Kalyanasundaram, K., Luminescence and Redox Reactions of the Metal-to-Ligand Charge-Transfer Excited-State of Tricarbonylchloro(Polypyridyl)Rhenium(I) Complexes. *Journal of the Chemical Society-Faraday Transactions II* **1986,** *82*, 2401-2415.
46. Takeda, H.; Koike, K.; Inoue, H.; Ishitani, O., Development of an Efficient Photocatalytic System for CO2 Reduction Using Rhenium(I) Complexes Based on Mechanistic Studies. *Journal of the American Chemical Society* **2008,** *130* (6), 2023-2031.
47. Guo, X.; Li, Q.; Liu, Y.; Jin, T.; Chen, Y.; Guo, L.; Lian, T., Enhanced Light-Driven Charge Separation and H2 Generation Efficiency in WSe2 Nanosheet–Semiconductor Nanocrystal Heterostructures. *ACS Applied Materials & Interfaces* **2020,** *12* (40), 44769-44776.
48. Wu, K.; Zhu, H.; Liu, Z.; Rodríguez-Córdoba, W.; Lian, T., Ultrafast Charge Separation and Long-Lived Charge Separated State in Photocatalytic CdS–Pt Nanorod Heterostructures. *Journal of the American Chemical Society* **2012,** *134* (25), 10337-10340.
49. Wu, K.; Song, N.; Liu, Z.; Zhu, H.; Rodríguez-Córdoba, W.; Lian, T., Interfacial Charge Separation and Recombination in InP and Quasi-Type II InP/CdS Core/Shell Quantum Dot-Molecular Acceptor Complexes. *The Journal of Physical Chemistry A* **2013,** *117* (32), 7561-7570.
50. Zhu, H.; Song, N.; Lian, T., Controlling Charge Separation and Recombination Rates in CdSe/ZnS Type I Core−Shell Quantum Dots by Shell Thicknesses. *Journal of the American Chemical Society* **2010,** *132* (42), 15038-15045.
51. Zhu, H.; Song, N.; Rodríguez-Córdoba, W.; Lian, T., Wave Function Engineering for Efficient Extraction of up to Nineteen Electrons from One CdSe/CdS Quasi-Type II Quantum Dot. *Journal of the American Chemical Society* **2012,** *134* (9), 4250-4257.
52. Yang, W.; Liu, Y.; Edvinsson, T.; Castner, A.; Wang, S.; He, S.; Ott, S.; Hammarström, L.; Lian, T., Photoinduced Fano Resonances between Quantum Confined Nanocrystals and Adsorbed Molecular Catalysts. *Nano Letters* **2021,** *21* (13), 5813-5818.
53. Oomens, J.; Steill, J. D., Free carboxylate stretching modes. *Journal of Physical Chemistry A* **2008,** *112* (15), 3281-3283.

54. Huang, J.; Gatty, M. G.; Xu, B.; Pati, P. B.; Etman, A. S.; Tian, L.; Sun, J. L.; Hammarstrom, L.; Tian, H. N., Covalently Linking $CuInS_2$ Quantum Dots with a Re Catalyst by Click Reaction for Photocatalytic CO_2 Reduction. *Dalton Transactions* **2018,** *47* (31), 10775-10783.
55. Claridge, T. D. W., *High-Resolution NMR Techniques in Organic Chemistry*. 3rd ed.; Elsevier: Amsterdam, 2016; p 537.

Chapter 4. Fano Resonance Coupling of Quantum Dot-ReC0A Complexes Reveals Loading and Size Dependence

4.1 Introduction

Semiconductor (SC) nanomaterials have emerged as invaluable assets in the realm of renewable energy, owing to their myriad of advantages in photocatalysis[1-5], photodetectors[6-8], and solar cell[9-12] applications. Additionally, the optical properties of SC quantum dots (QDs) can be manipulated by altering their size and composition.[13-19] This allows for the design of nanomaterials with specific energy levels and differing surfaces which affects their charge carrier lifetimes, making them suitable for the aforementioned applications. The integration of SC QDs with molecular catalysts facilitates the prospect of enhancing processes such as CO_2 reduction and H_2 generation, thus diverging from conventional electrochemical or purely photochemical approaches reliant solely on the catalyst where it can act as the light absorber. Therefore, nanoparticle-molecular catalyst complexes have emerged as a promising alternative, circumventing the disadvantages of molecular catalysts on their own.

Several catalysts exhibit distinctive vibrational signatures in the infrared region that allow for monitoring their ultrafast dynamics upon catalyzing a certain reaction.[20] Additionally, semiconductor nanocrystals (NCs), specifically QDs, are known to have broad absorptions in the infrared, corresponding to intraband transitions in the conduction band. Oftentimes, ligands residing on the surface of QDs also have manifest vibrational signatures in the near IR region.[21-24] Thus adsorbate vibrations and QD intraband excitations may overlap and lead to the formation of Fano resonance (FR).[25] FR arises from the mixing of a discrete quantum state to a continuum state; here these would correspond to a sharp vibrational mode from a catalyst or ligands and the broad absorption from the intraband transition of QDs, respectively. This phenomenon has been observed in various types of

systems, most commonly in plasmonic nanomaterials.[26-29] For example, Agrawal et al. investigated F and Sn co-doped InO_3 NCs with oleate ligands bound to the surface.[30] They observed that the C-H bonds within the oleate can couple to the localized surface plasmon resonance of the NCs, resulting in a Fano lineshape. FR usually manifests as a derivative shaped feature in IR spectra, but can vary depending on the Fano asymmetry parameter q, which relates to the transition probabilities into the continuum and the hybridized discrete level and determines the shape of the observed feature.[25] This type of coupling can also occur in QDs.

Recently, we have demonstrated that FRs emerge upon binding a Fe-Fe molecular catalyst ($[Fe_2(cbdt)(CO)_6]$ to CdS nanorods (NRs) and CdSe QDs.[31] Fano resonance coupling occurred between the three vibrational modes of the catalyst and the broad absorption from the NCs regardless of whether electron transfer was possible. Several studies have also demonstrated in literature that QD excitons can couple to the vibrational modes of their capping ligands, usually long chain organic molecules such as oleic acid, in the near IR region.[21-22] Upon exchanging the native ligands, it has been shown that charge carrier dynamics can be affected, particularly intraband relaxation of hot carriers.[18-19, 32-34] This presents the intriguing prospect of vibrational coupling, in this specific case, FR coupling, being able to affect charge transfer processes within NC-molecular catalyst complexes.

Herein, we use a well-known CO_2 reduction catalyst, $Re(CO)_3$(bpy-COOH)Cl (ReC0A) at several concentrations, and bound to QDs of varying sizes, to investigate the effect of catalyst loading and QD size on the observed transient FRs. We use both transient visible (TA) and infrared (TRIR) spectroscopies to monitor electron transfer between the QD and complex, as well as the shape of the FR under these different conditions. We find that the Fano asymmetry parameter q increases with catalyst concentration but decreases with increasing QD size. This provides us with deeper insight into NC-catalyst interactions.

4.2 Results and Discussion

4.2.1 Characterization of Quantum Dots

CdSe QDs were used in our present study because of their superior size tunability within the visible range compared to other chalcogenide QDs (CdS, Cd_3P_2, etc). Several sizes of CdSe QDs were synthesized after following previous literature, resulting in exciton band absorptions corresponding to sizes ranging from 2 to 5.6 nm in diameter. CdSe QDs were dispersed in heptane or hexanes, and UV-Vis spectra and band diagrams for three QDs are shown in Figure 4.1a and b. Their exciton band absorptions are centered at 490, 545, and 582 nm, corresponding to 2.3, 3.0, and 3.9 nm diameters, which we refer to as CdSe 490, CdSe 545, and CdSe 582, respectively.

Different concentrations of ReC0A were introduced to each size of CdSe QDs dispersed in hexanes, as depicted in FTIR (Figure 4.1c). The molecular catalyst is not soluble in hexanes, so the intensity of the vibrational modes indicates the amount of ReC0A molecules only bound to the QD surface through their carboxylic acid ligands (Figure S4.1a). Average amounts of catalyst bound for each concentration are detailed in Table S4.1. The catalyst in acetonitrile (MeCN) has a visible absorption at 400 nm corresponding to the metal-to-ligand charge transfer (MLCT) state (Figure S4.1c).[35-36] FTIR spectra of ReC0A in MeCN show three vibrational modes centered at 2025, 1921, and 1905 cm^{-1}, corresponding to the symmetric, asymmetric, and out of phase symmetric CO stretches, respectively (Figure S4.1b). Upon addition to the QDs, the lower frequency modes slightly shift to 1925, and 1909 cm^{-1} (Figure 4.1c). Figure S4.2a and b shows FTIR of CdSe 545 and 582 with varying concentrations of ReC0A and demonstrate the same trend; as the ReC0A concentration added increases, more ReC0A binds to the QD. All FTIR spectra are solvent subtracted, as hexanes has an absorption at the same frequency as the ReC0A high frequency mode and second low frequency mode, with an additional shoulder peak at approximately 2050 cm^{-1} (unsubtracted FTIR shown in Figure

S4.2c). These discrete vibrational modes will couple to the 1S to 1P intraband transition of the QD to generate FR signals.[37] We focus on the high frequency mode centered at 2025 cm^{-1} in the transient IR experiments as it is easier to observe on top of the solvent absorptions.

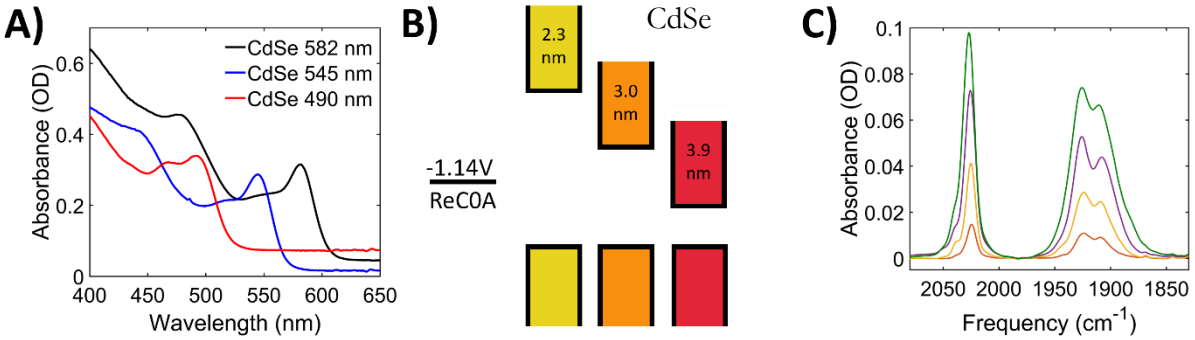

Figure 4.1. A) UV-Vis spectra of the three CdSe QDs demonstrating their exciton band positions. Corresponding sizes are 2.3 (CdSe 490), 3.0 (CdSe 545), and 3.9 (CdSe 582) nm. B) Energy band diagrams of each QD compared to the reduction potential of ReC0A. Lower bands correspond to the valence band for each nanoparticle, while the higher bands are the conduction bands. As the QD diameter increases, the band gap decreases. C) Solvent subtracted FTIR spectra of CdSe 490 with varying amounts of ReC0A bound to the surface (red: 0.25x, yellow: 0.5x, purple: 1x, green: 2x).

4.2.2 Electron Transfer Rates After Visible Excitation

Transient absorption (TA) experiments were performed to elucidate the electron transfer properties of CdSe QDs with varying concentrations of ReC0A and were conducted under 475 nm excitation, to avoid direct excitation of the catalyst. The first panel in Figures S4.3, S4.4, and S4.5 shows TA spectra for each individual QD in heptane, CdSe 490, CdSe 545, and CdSe 582, respectively. After excitation, ground state bleaches appear for each sample due to state filling of the 1S conduction

band (CB) state.[38] Triexponential fits resulted in amplitude weighted average time constants that were on the order of tens of nanoseconds shown in Table S4.2. Figure 4.2 shows the kinetic traces for each sample probed at the center of the QD bleaches. For CdSe 490, the exciton bleach (XB) recovery occurs significantly faster upon addition of 0.25xRe (2.1 ns), indicating electron transfer to the catalyst (Figure 4.2, Figure S4.3). As more ReC0A is added, the bleach recovery lifetime decreases to 0.31 ns with 1xRe, suggesting that with more catalyst added, electron transfer occurs faster. However, at 2xRe the bleach recovery slightly decreases to 0.41 ns suggesting that electron transfer is ideal the 1x concentration of the catalyst. The same trend is observed for CdSe 545; however, the lifetimes are longer after ReC0A addition (between 3.0 and 4.3 ns), indicating slower electron transfer to the catalyst. This is because of the increased size of the QD compared to CdSe 490. As QD size increases, the band gap is known to decrease. This would change the position of the CB band edge corresponding to a decrease in the QD reduction potential (Figure 4.1b). CdSe 582 with ReC0A demonstrated similarly longer XB recovery lifetimes as the QD only case, several tens of nanoseconds, indicating very little electron transfer occurs, due to the reduction potential of the QDs being similar to or lower than that of the catalyst. Upon electron transfer, the catalyst should be singly reduced and is known to have a small absorption at approximately 520 nm.[39] This is not observed, due to the large absorption of the bleaches for the QDs most likely obscuring the signal.

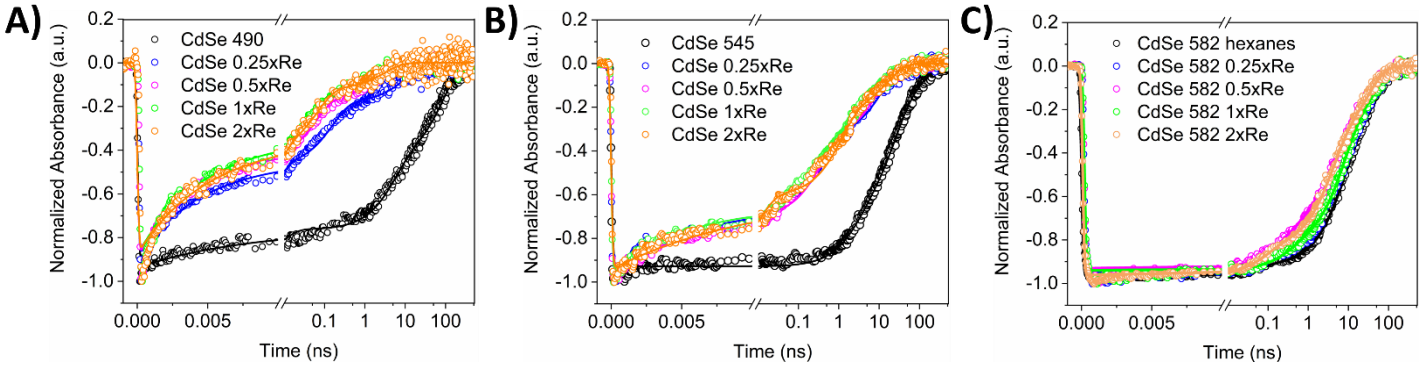

Figure 4.2. Fitted kinetics of CdSe QDs with varying amounts of ReC0A bound, probed at their corresponding ground state bleaches. A) CdSe 490. The addition of ReC0A to the QD results in faster bleach recovery indicating electron transfer. B) CdSe 545. At this point, the CB edge is still more negative than the ReC0A reduction potential. Slower bleach recovery compared to CdSe 490 indicates electron transfer does not occur as quickly. C) CdSe 582. Similar kinetics implies that very little electron transfer occurs.

4.2.3 Fano Resonance as a Function of Catalyst Concentration

Time resolved infrared spectroscopy (TRIR) was used to determine the interaction between the QDs and varying concentrations of catalyst in hexanes. Upon 475 nm excitation, we have observed two large positive absorption features at 2030 and 2050 cm^{-1} for bare QDs, which corresponds to the solvent absorption of hexanes (Figure 4.3). This suggests that the solvent vibrational modes couple to the photoinduced IR 1S to 1P transition in the CdSe QD CB.[31] Positive absorption features were observed at frequencies identical to the solvent's absorption upon the introduction of ReC0A to the QDs. The position of the ReC0A high frequency mode (~2025 cm^{-1}) is directly on top of the hexanes absorption. The peak at 2030 cm^{-1} increases in amplitude in comparison to the pure QDs in hexanes, indicating that the QD-ReC0A coupling signal is on top of the solvent FR (Figure S4.6). This demonstrates the catalyst indeed couples to the QD. Although the FR from coupling between ReC0A and the QDs is on top of the solvent absorption, the second peak at ~2050 cm^{-1} only corresponds to the solvent.

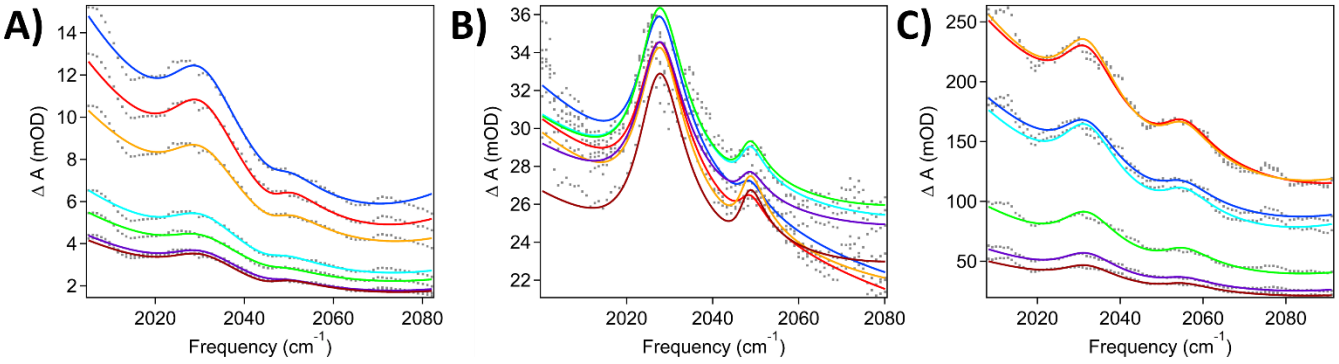

Figure 4.3. TRIR spectra of CdSe QDs in hexanes. A) CdSe 490 B) CdSe 545 C) CdSe 582. Absorptions at ~2030 and 2050 cm^{-1} suggest solvent vibrations couple with the QD intraband transition. (Legend: blue: 0-2 ps, red: 2-5 ps, orange: 5-15 ps, cyan: 25-100 ps, green: 100-200 ps, purple: 400-800 ps, burgundy: 800-1670 ps).

The Fano parameter, q, provides a measure of the asymmetry in the FR lineshape. Microscopically, q is directly proportional to the transition probability into hybrid (molecular-QD) discrete states embedded in the intraband QD continuum, and inversely proportional to the transition probability into the unperturbed continuum state resonant with the catalyst vibrational mode. To determine the value of q, all TRIR spectra have been globally fitted with the following equation (Eq 1)[25, 31, 40]:

$$\Delta A = \sum_i \left[A_i \frac{(q_i + \varepsilon_i)^2}{1+\varepsilon_i^2} - A_i' \frac{2}{\pi}\left(\frac{\Gamma_i}{4(\nu-\nu_{0,i})^2 + \Gamma_i^2}\right)\right] + PA - IR(\nu) \qquad (1)$$

where the first and second terms correspond to the absorption due to the formation of the Fano resonance and the (ground state bleach) Lorentzian absorption, respectively. The PA-IR term corresponds to the IR signal originating from the signal corresponding to the QD intraband electronic

transition. A_i and A_i' are the amplitudes of the Fano and Lorentzian terms, respectively. q_i is the Fano asymmetry parameter, Γ_i is the width of the IR transition, and $v_{0,i}$ is the peak position of the vibrational feature. ε_i is the detuning term where $\varepsilon_i = 2\left(v - v_{0,i}\right)/\Gamma_i$. Since hexanes appears to couple to the QDs, we globally fit the data to Eq 1 with two Fano and two Lorentzian terms corresponding to each peak, 2030 and 2050 cm^{-1} to obtain q values for the coupling of both solvent vibrations. After ReC0A is bound to the QD, because the solvent and ReC0A CO symmetric mode overlap, we subtracted the solvent peaks from each QD-ReC0A sample spectra by using the q values and other parameters from the solvent fits. This is described in detail in the Supporting Information (4.4.3). Hereafter, all spectra shown have been solvent subtracted.

For each QD, as the amount of bound ReC0A increases, the amplitude of the FR signal increases, suggesting enhanced oscillator strength for the transition into the hybrid discrete mode. Figure 4.4 shows CdSe 490 without ReC0A, and with additional amounts of ReC0A, demonstrating this trend. We attribute this to the strength of the CO modes as a vibrational oscillator. With more catalyst bound to the surface, there are more CO modes, and therefore a larger dipolar polarization density. This increase in the oscillator strength of the catalyst modes on the QD surface leads to an expected increase in q with catalyst concentration. As the QD electronic signal decays, the FR amplitude simultaneously decreases, indicating the essential role of the conduction band electron, in the Fano resonance. After the FR signal decays, a peak at ~ 2013 cm^{-1} and a negative feature at 2035 cm^{-1} suggests that ReC0A is being singly reduced.[37, 41] This confirms that the FR signal obstructs the singly reduced signal. Between the 1x and 2xRe concentrations, the amplitudes of the reduced species get larger, indicating more ReC0A is being reduced as we have observed with Cd_3P_2-ReC0A in a previously published paper.[41] The augmentation in FR signal with higher ReC0A concentration was likewise noted in the case of the other two studied quantum dots, CdSe 545 (Figure S4.8) and CdSe 582 (Figure S4.9). Nevertheless, due to the slower electron transfer kinetics compared to the smallest

QD, the observation of the singly reduced species was not observed. The fits for each sample spectra agree well with the data. Table 4.1 shows the coupling constants for each sample, demonstrating that as catalyst concentration increases, the Fano asymmetry associated with each QD size also increases.

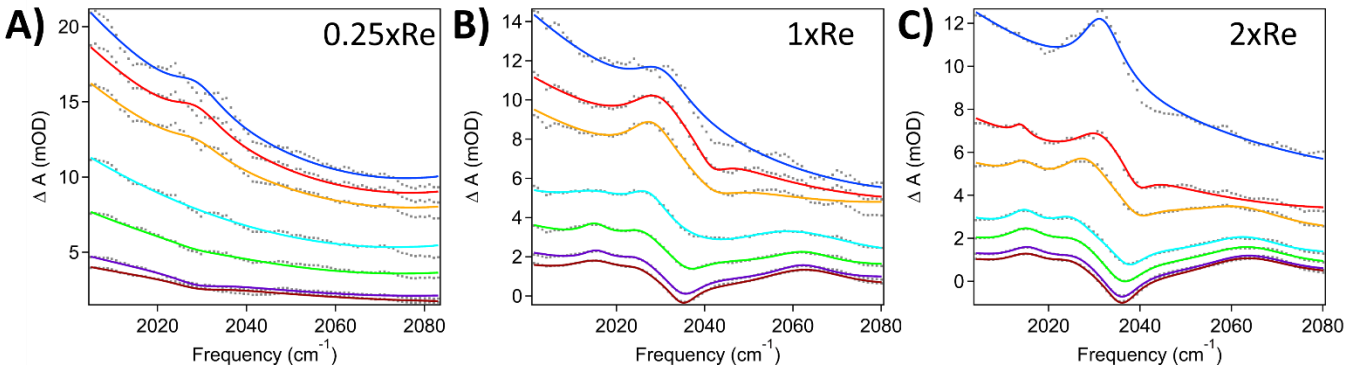

Figure 4.4. CdSe 490 with varying amounts of ReC0A. Since the singly reduced ReC0A species begins to appear as the FR signal decays, two more Lorentzians were used to fit the peak at ~2013 cm^{-1} and bleach at 2035 cm^{-1}. A) CdSe 490-0.25xRe. B) CdSe 490-1xRe. C) CdSe 490-2xRe. (Legend: blue: 0-2 ps, red: 2-5 ps, orange: 5-15 ps, cyan: 25-100 ps, green: 100-200 ps, purple: 400-800 ps, burgundy: 800-1670 ps)

Table 4.1. Fano asymmetry parameters q each QD and ReC0A concentration. With higher ReC0A concentrations, the coupling constants increase.

	0.25xRe	**0.5xRe**	**1xRe**	**2xRe**	**4xRe**
CdSe 490	10.3 ± 1.9	--	21.9 ± 4.2	41.4 ± 12.1	--
CdSe 545	--	15.5 ± 3.5	20.6 ± 3.17	32.7 ± 5.2	66.4 ± 15.3
CdSe 582	10.6 ± 1.9	12.3 ± 1.4	20.2 ± 4.5	23.2 ± 4.4	--

4.2.4 Fano Resonance as a Function of QD Size

We also investigated the effect of QD size on the FR coupling. It is not explicitly apparent from the spectra for CdSe 490 and CdSe 582 at a concentration of 2xRe, that there is a significant difference in the FR amplitude. However, our fits result in asymmetry parameters constants that reveal considerable size dependence. To observe this more clearly, four new QDs, CdSe 525 (2.6 nm), CdSe 550 (3.0 nm), CdSe 580 (3.8 nm), and CdSe 620 (5.6 nm), were synthesized. The highest concentration of ReC0A (2x) was added to each, with their FTIR shown in Figure S4.11. Upon 475 nm excitation of the QDs, as seen previously, we observe two positive features at approximately 2030 cm^{-1} and 2050 cm^{-1}, corresponding to the solvent absorptions (Figure S4.10). Upon addition of ReC0A, the solvent absorptions were still present, and the intensity of the 2030 cm^{-1} peak increased, as previously observed. The solvent FR was fitted to equation 1 and the values obtained were used to subtract the solvent contribution from the QD-ReC0A samples as described previously. The subtracted QD-ReC0A FR was then globally fitted to the same equation to obtain coupling values (Table 4.2). Comparing both the FR amplitudes of each sample in Figure 4.5, as well as the asymmetry parameters, there appears to be a basic trend. As the size of the QD increases, the FR amplitude, and the asymmetry factor q decrease. We attribute this effect to the extent with which the QD electron wavefunction penetrates the surface. Since QDs are quantum confined, in comparison to bulk semiconductors, they have larger electron wavefunction amplitudes at longer distances from the surface.[42-43] It is well known that as QD size increases, a simultaneous decrease occurs for the band gap and the electron wavefunction amplitude away from the surface due to the quantum confinement effect.[13-14, 44] As shown in computations by Zhu et al, the radial distributions for electron and hole surface densities decrease with increase QD size.[15] It follows that as the QD size increases, the electron wavefunction decays faster away from the surface. This feature leads to a decrease in the electronic

charge transfer coupling between the QD and catalyst CO vibrational modes promoted via its vibronic coupling with the catalyst LUMO. A reduced spatial overlap between the molecular LUMO and the intraband electronic excited state leads to a reduced Fano hybridization and a weaker FR signal with a smaller vibrational oscillator strength and asymmetry parameter q, as observed here.

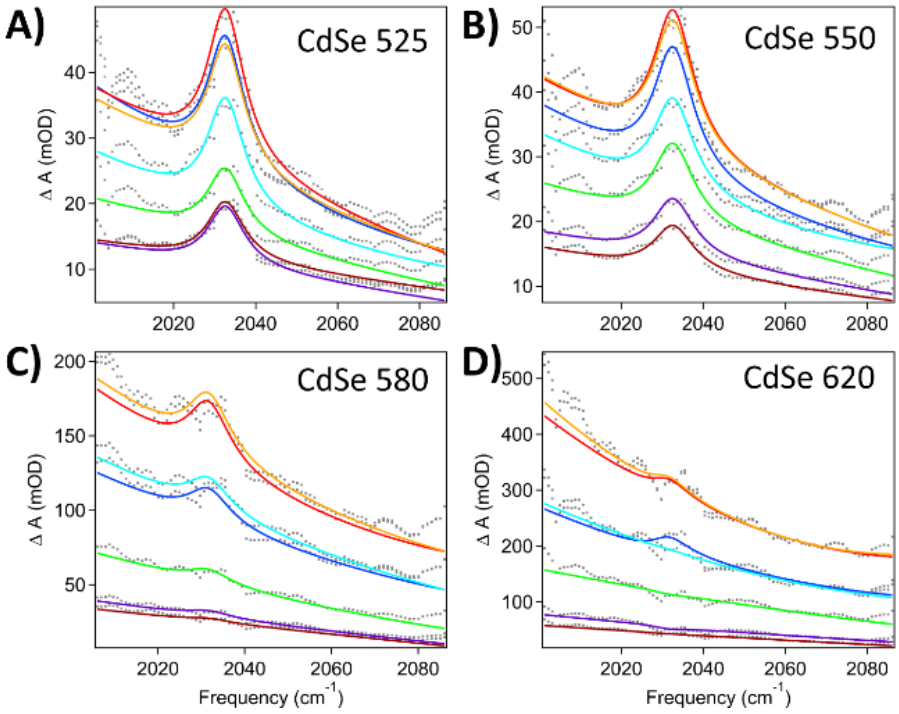

Figure 4.5. CdSe QDs after solvent subtraction. As QD size increases, coupling decreases. (Legend: blue: 0-2 ps, red: 2-5 ps, orange: 5-15 ps, cyan: 25-100 ps, green: 100-200 ps, purple: 400-800 ps, burgundy: 800-1670 ps)

Table 4.2. Fano parameter (q) values for each QD-2xRe complex.

	CdSe 525	**CdSe 550**	**CdSe 580**	**CdSe 620**
2xRe	29.8 ± 7.3	22.9 ± 3.6	20.2 ± 6.8	4.41 ± 1.1

While we describe the FR as arising from a charge transfer mechanism depending on the overlap of the QD electron wavefunction and the catalyst LUMO, it is also possible for the FR to occur through a dipole-dipole interaction. We are currently developing a model to determine this and more explicitly describe the mechanism of this FR coupling and how the asymmetry parameter q changes with QD size.

4.3 Conclusions

In conclusion, after adding varying amounts of ReC0A to different QDs, we have demonstrated that the FR signal increases with catalyst concentration. This effect is induced by a greater density of catalysts bound to the surface and the corresponding oscillator strength of catalysts vibrations embedded in the QD intraband absorption continuum. In addition, when varying the size of the QDs, we observed that increasing the QD diameter results in a decreasing FR signal. This is ascribed to the reduced penetration of the electron wavefunction away from the surface with increasing QD size, and corresponding weaker interaction of the bound ReC0A adsorbate with the larger QDs. These results have provided us with a deeper understanding of how FR is affected by various experimental conditions and lend us further insight into the interactions between QDs and their surface bound species.

4.4 Supporting Information

4.4.1 Characterization of ReC0A on CdSe QDs

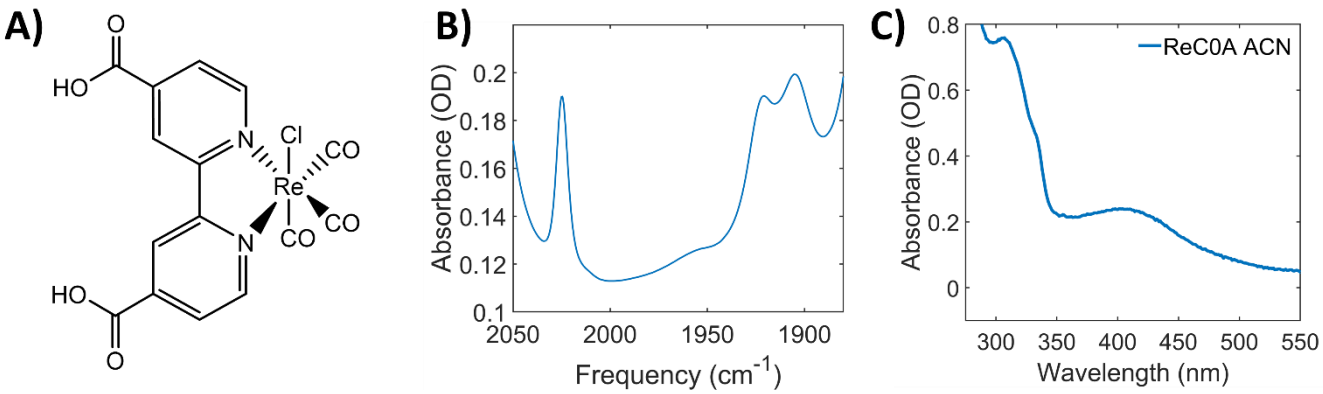

Figure S4.1. A) Molecular structure of ReC0A. Carboxylic acid groups allow binding of the catalyst to the QD surface. B) FTIR of ReC0A in acetonitrile shows high and low frequency modes corresponding to different CO stretching modes (symmetric, asymmetric, and out of phase symmetric, respectively). C) UV-Vis spectra of ReC0A in MeCN. Absorptions at approximately 305 and 400 nm correspond to the π to π* transition of the bipyridine and the MLCT transition, respectively.

Table S4.1. Number of ReC0A molecules bound to the QD surface (describe how to get these numbers and add concentrations too)

	0.25xRe	**0.5xRe**	**1xRe**	**2xRe**
CdSe 490	1.2	--	5.9	8.4
CdSe 545	--	10.1	17.8	36.7
CdSe 582	9.4	9.7	14.7	25.6

In order to obtain the number of ReC0A on the QDs, the catalyst absorbances in the FTIR

were used to calculate the concentrations of ReC0A for each QD. After obtaining the QD concentrations, the number of moles for each were converted to the number of molecules or QDs in each sample. The number of ReC0A molecules was divided by the number of QDs in the sample volume to get the average amount of catalyst on each QD. For CdSe 545, an additional concentration, 4xRe, was also tested, with FTIR shown in Figure S4.2a (green trace). This concentration had approximately 65.5 molecules on the QD surface.

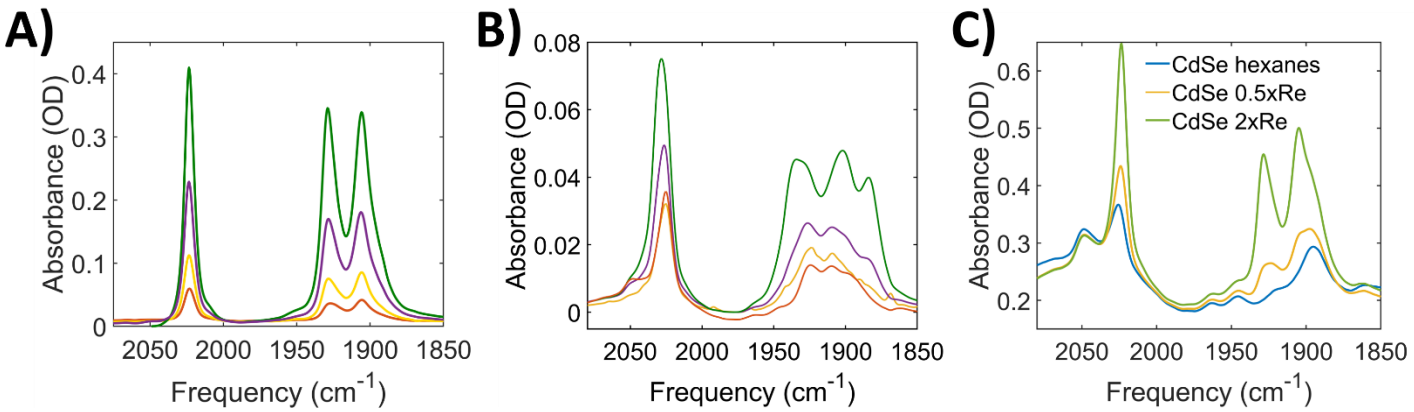

Figure S4.2. FTIR of varying concentrations of ReC0A on the QD. A) Varying ReC0A concentrations on CdSe 545 where higher concentrations were used: 0.5x (red), 1x (yellow), 2x (purple), and 4xRe (green). B) Varying ReC0A concentrations on CdSe 582 (red: 0.25x, yellow: 0.5x, purple: 1x, green: 2x). C) FTIR of CdSe 545 0.5x and 2xRe compared to the QD in hexanes demonstrates the solvent absorbs at the same frequency as the ReC0A complex.

4.4.2 TA Spectra of ReC0A on QDs

The following figures show TA spectra of the QDs with each concentration of ReC0A bound. Each QD spectra demonstrates slow bleach recovery indicating a long-lived band edge electron within

1.6 ns. Lifetimes in Table S4.2 and kinetics traces in Figure 4.2 demonstrate that the exciton lives for several tens of nanoseconds. CdSe 490-ReC0A shows fast bleach recovery within 1.6 ns indicating fast electron transfer from the QD to the catalyst. However, no signal corresponding to the singly reduced catalyst appears (~520 nm) due to the strong absorption of the QD bleach. CdSe 545 spectra with ReC0A demonstrate the same phenomenon as seen with CdSe 490. However, because of the increased size, the electron transfer does not proceed as quickly, resulting in slower bleach recovery compared to CdSe 490. The last QD, CdSe 582, shows that with the catalyst, there is little bleach recovery, meaning that there is very little electron transfer occurring.

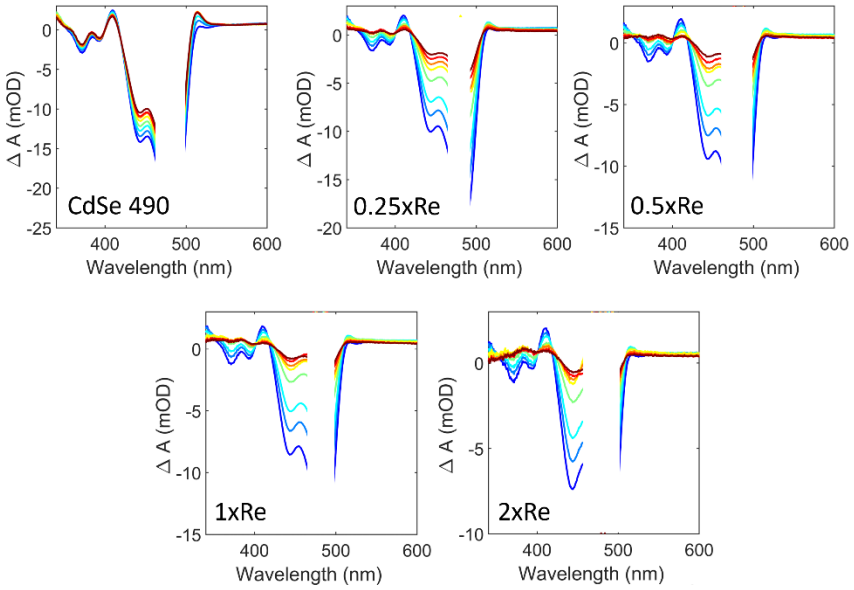

Figure S4.3. TA spectra for CdSe 490 with varying amounts of ReC0A (dark blue: 0-2 ps, blue: 2-5 ps, cyan: 5-15 ps, green: 25-100 ps, yellow: 100-200 ps, orange: 250-350 ps, red: 500-800 ps, burgundy: 1000-1600 ps)

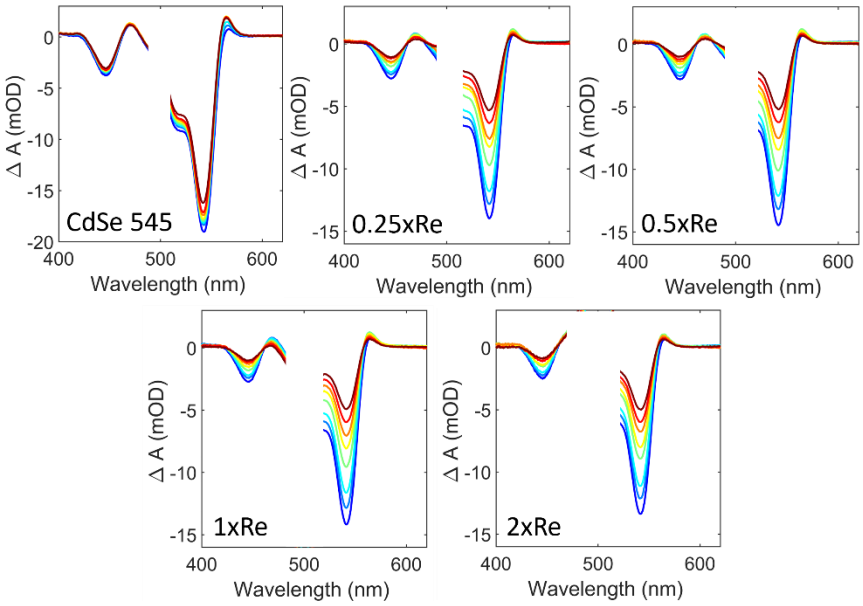

Figure S4.4. TA spectra for CdSe 545 with and without ReC0A bound. (dark blue: 0-2 ps, blue: 2-5 ps, cyan: 5-15 ps, green: 25-100 ps, yellow: 100-200 ps, orange: 250-350 ps, red: 500-800 ps, burgundy: 1000-1600 ps)

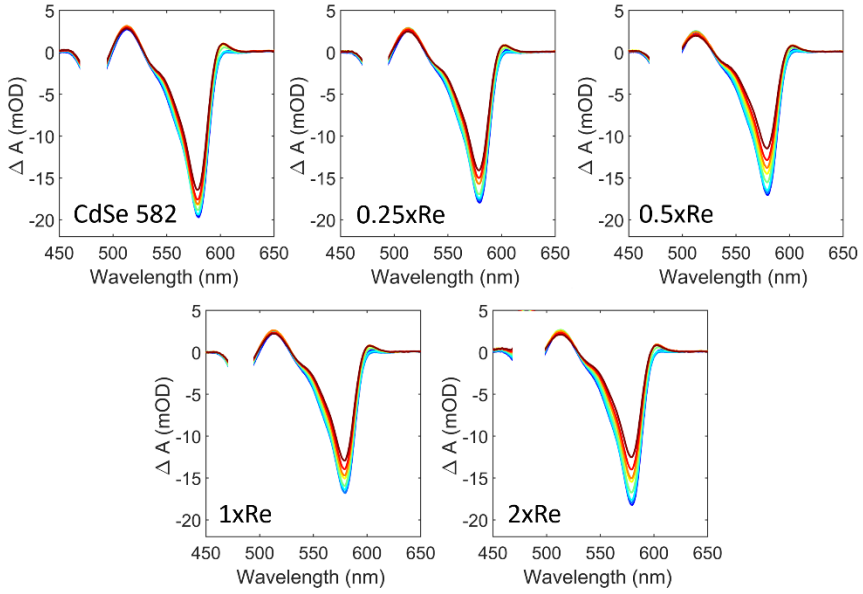

Figure S4.5. TA spectra for CdSe 582 with and without ReC0A. (dark blue: 0-2 ps, blue: 2-5 ps, cyan: 5-15 ps, green: 25-100 ps, yellow: 100-200 ps, orange: 250-350 ps, red: 500-800 ps, burgundy: 1000-1600 ps)

Table S4.2. Amplitude weighted average time constants of CdSe QDs with and without ReC0A

	CdSe 490	**CdSe 545**	**CdSe 582**
QD only	41.42 ± 0.022 ns	39.4 ± 0.45 ns	22.2 ± 1.91 ns
0.25xRe	2.1 ± 0.0049 ns	4.3 ± 0.003 ns	19.6 ± 0.34 ns
0.5xRe	0.424 ± 0.0028 ns	3.52 ± 0.002 ns	13.9 ± 0.32 ns
1xRe	0.31 ± 0.0047 ns	2.98 ± 0.0012 ns	18.7 ± 0.58 ns
2xRe	0.41 ± 0.0094 ns	4.2 ± 0.13 ns	13.2 ± 0.045 ns

4.4.3 Subtraction of Solvent from TRIR Spectra

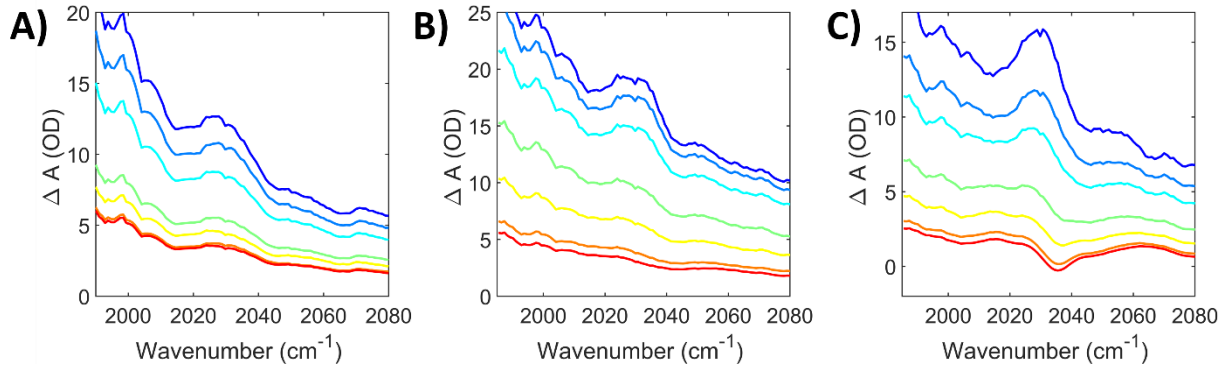

Figure S4.6. Unsubtracted TRIR spectra. A) CdSe 490 in hexanes. The two large absorptions observed correspond to solvent FR coupling. B) CdSe 490-0.25xRe. Amplitude of FR signal at ~2030 cm^{-1} increased compared to A, suggesting FR coupling with the ReC0A. The solvent and ReC0A signals overlap. C) CdSe 490-2xRe. The amplitude of FR is even larger, due to increased

ReC0A concentration. Solvent FR signal can be seen at 2050 cm^{-1}. This will allow us to subtract the solvent contribution from the 2030 cm^{-1} peak.

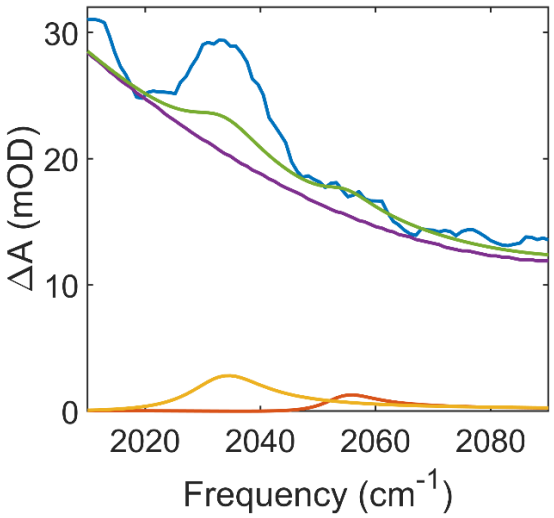

Parameters	**Values from solvent fit**
Amplitude 2	0.00012
q_2	3.13 (**fixed**)
$v_{0,2}$	2054 (**fixed**)
Γ_2	11 (**fixed**)
Amplitude 1 (A_2/1.42)	0.000085
q_1	5.69 (**fixed**)
$v_{0,1}$	2033 (**fixed**)
Γ_1	16 (**fixed**)

Figure S4.7. Demonstration of how solvent contribution is subtracted from TRIR spectra. Blue: unsubtracted data; Purple: QD background fitted with a polynomial (n=3); Red: fit for second FR peak; Yellow: solvent peak to subtract from QD-ReC0A, determined by the amplitude ratio between A_{2050} and A_{2030} from the solvent fit (Ratio = 1.42); Green: FR signal originating from the solvent. This will be subtracted from the data.

Since hexanes appears to couple to the QDs, we globally fit the data to equation 1 with two Fano and two Lorentzian terms corresponding to each peak, 2030 and 2050 cm^{-1}. After ReC0A is bound to the QD, because the solvent and ReC0A CO symmetric mode overlap, each QD-hexanes sample was fit to equation 1 with two Fano terms and two Lorentzian terms to obtain q values for coupling of both solvent vibrations. In order to separate these contributions, we subtracted the solvent peaks from each QD-ReC0A sample spectra. We first fit the QD-hexanes spectra and obtained the

coupling, as well as the amplitudes of the FR peaks. The Lorentzian amplitudes were held to some small value (~0.001) due to a negligible contribution of the Lorentzian absorption (from FTIR absorbance) in comparison to the FR signal. To subtract the solvent contribution, we held the parameters from the solvent fit constant (q_i, ε_i, $\nu_{0,i}$, and Γ_i) and found the ratios between the fitted amplitude of the 2050 cm^{-1} peak to the 2030 cm^{-1} absorption (A_{2050}/A_{2030}). The ratio was fixed for each time delay when inputting amplitude values for the QD-ReC0A FR peak and the hexanes peak at 2050 cm^{-1}. For example, if the ratio between the peaks was $A_{2050}/A_{2030} = 2.0$ from the CdSe 490-hexanes sample at the 0-1 ps time delay, after moving to the QD-1xRe sample, all other fitting parameters would be held constant. If the Fano amplitude for 2050 cm^{-1} (hexanes) was 0.02, then the amplitude of the hexanes under the QD-1xRe FR peak would be 0.04, after which we would be able to subtract this curve from the spectra to result in the QD-ReC0A only FR peak (Figure S4.7). All other spectra that appear after Figure S4.7 have been solvent subtracted.

4.4.4 Fitted TRIR Spectra of CdSe 545 with and without ReC0A

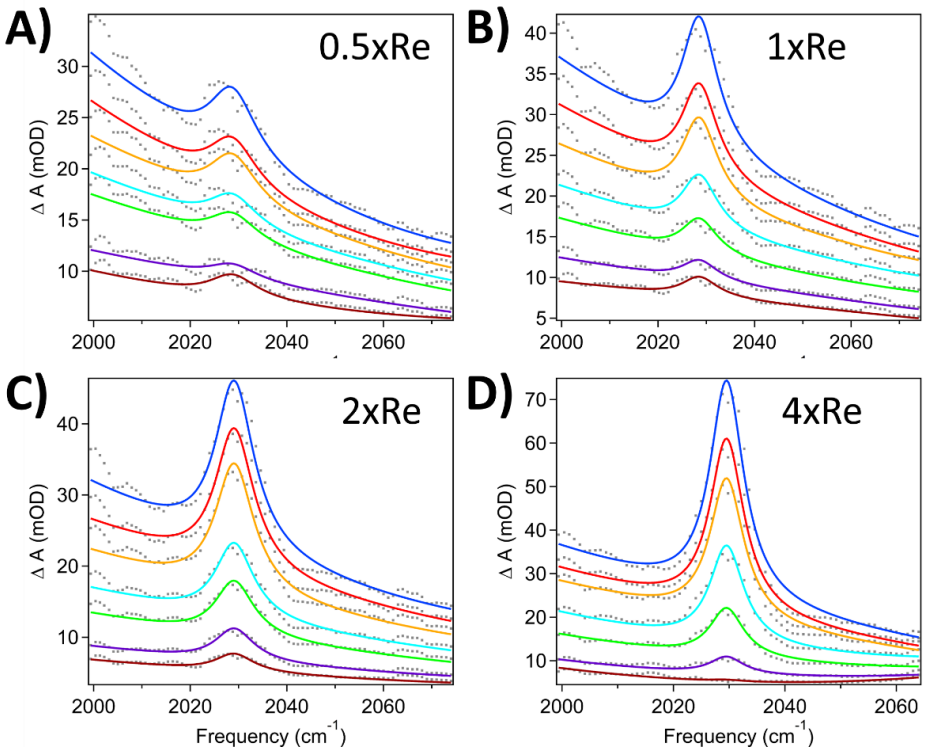

Figure S4.8. CdSe 545 with ReC0A. As seen with CdSe 490, with higher amounts of ReC0A added to the QDs, the FR signal increases. 4xRe is the highest concentration used in this study and shows a very clear sharp FR signal. CdSe 545-0.25xRe was not included in this study.

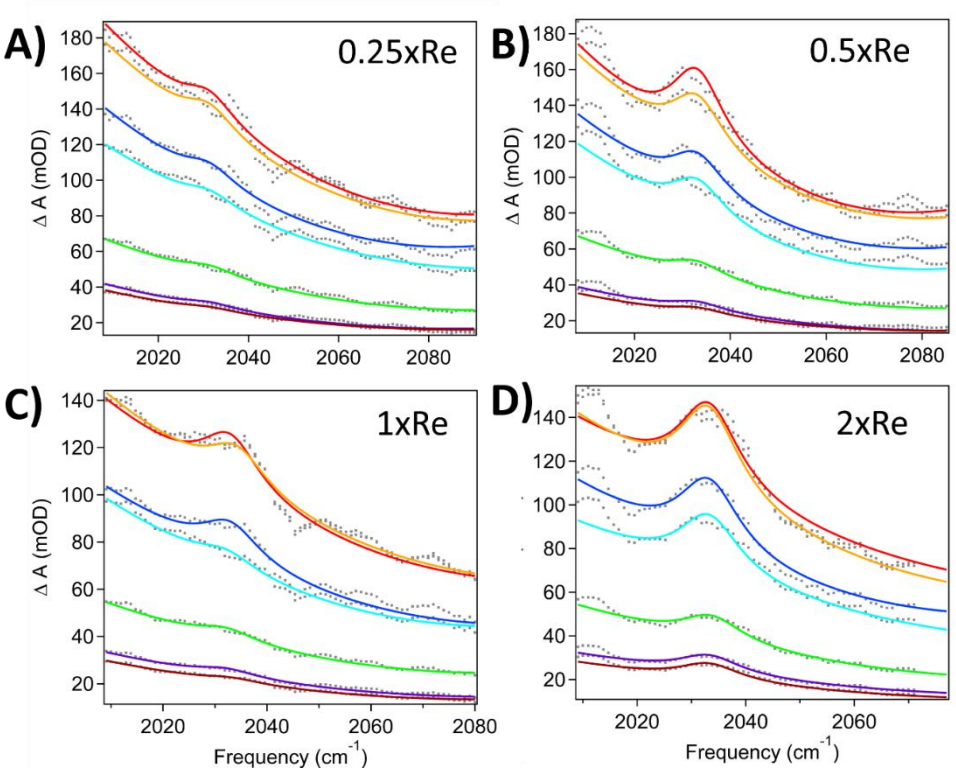

Figure S4.9. CdSe 582 ReC0A. The same trend that was seen for the other two QDs is observed for CdSe 582.

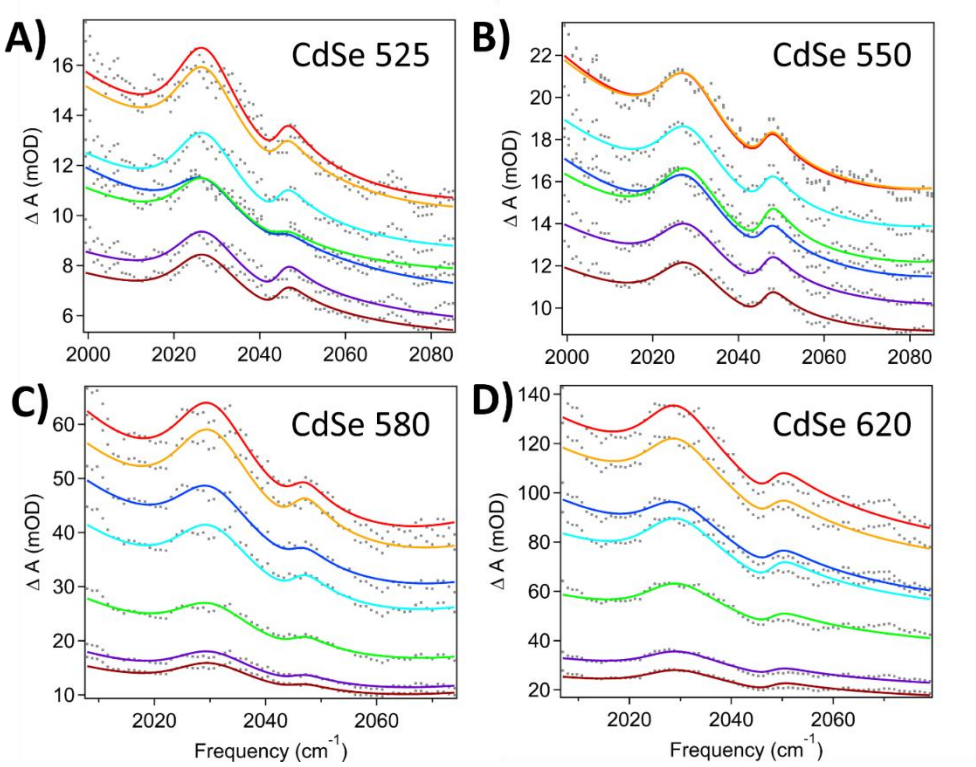

Figure S4.10. TRIR of QDs in hexanes. Both solvent absorptions are seen for each QD for our size dependent study.

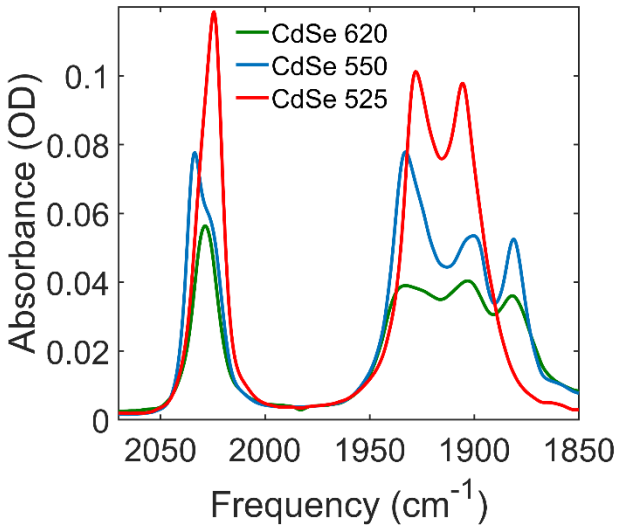

Figure S4.11. FTIR of CdSe 525, 550, and 620 with 2xRe bound to the surface.

Table S4.3. Number of ReC0A molecules bound to CdSe 525, 550, and 620.

	CdSe 525	**CdSe 550**	**CdSe 580**	**CdSe 620**
2xRe	21.8	17.3	25.6	27.7

Table S4.4. Solvent q values (coupling) for all QDs in hexanes.

CdSe	**490**	**525**	**545**	**550**	**580**	**582**	**620**
2030 cm^{-1}	3.7 ± 0.08	6.7 ± 0.41	6.7 ± 0.33	6.5 ± 0.4	5.6 ± 0.21	5.7 ± 0.26	4.3 ± 0.18
2050 cm^{-1}	0.94 ± 0.05	1.6 ± 0.1	3.0 ± 0.31	1.9 ± 0.1	2.0 ± 0.13	3.1 ± 0.15	1.0 ± 0.06

4.5 References

1. Wang, C., Chapter 9 - Quantum Dots for Visible-Light Photocatalytic CO2 Reduction. In *Novel Materials for Carbon Dioxide Mitigation Technology*, Shi, F.; Morreale, B., Eds. Elsevier: Amsterdam, 2015; pp 269-295.
2. Moore, G. F.; Brudvig, G. W., Energy Conversion in Photosynthesis: A Paradigm for Solar Fuel Production. *Annual Review of Condensed Matter Physics* **2011,** *2* (1), 303-327.
3. Kamat, P. V., Quantum Dot Solar Cells. Semiconductor Nanocrystals as Light Harvesters. *The Journal of Physical Chemistry C* **2008,** *112* (48), 18737-18753.
4. Wu, K.; Lian, T., Quantum confined colloidal nanorod heterostructures for solar-to-fuel conversion. *Chemical Society Reviews* **2016,** *45* (14), 3781-3810.
5. Li, Q.; Zhao, F.; Qu, C.; Shang, Q.; Xu, Z.; Yu, L.; McBride, J. R.; Lian, T., Two-Dimensional Morphology Enhances Light-Driven H2 Generation Efficiency in CdS Nanoplatelet-Pt Heterostructures. *Journal of the American Chemical Society* **2018,** *140* (37), 11726-11734.
6. Đorđević, N.; Schwanninger, R.; Yarema, M.; Koepfli, S.; Yarema, O.; Salamin, Y.; Lassaline, N.; Cheng, B.; Yazdani, N.; Dorodnyy, A.; Fedoryshyn, Y. M.; Wood, V.; Leuthold, J., Metasurface Colloidal Quantum Dot Photodetectors. *ACS Photonics* **2022,** *9* (2), 482-492.
7. Livache, C.; Martinez, B.; Goubet, N.; Gréboval, C.; Qu, J.; Chu, A.; Royer, S.; Ithurria, S.; Silly, M. G.; Dubertret, B.; Lhuillier, E., A colloidal quantum dot infrared photodetector and its use for intraband detection. *Nature Communications* **2019,** *10* (1), 2125.
8. Guo, R.; Zhang, M.; Ding, J.; Liu, A.; Huang, F.; Sheng, M., Advances in colloidal quantum dot-based photodetectors. *Journal of Materials Chemistry C* **2022,** *10* (19), 7404-7422.
9. Kirmani, A. R.; Luther, J. M.; Abolhasani, M.; Amassian, A., Colloidal Quantum Dot Photovoltaics: Current Progress and Path to Gigawatt Scale Enabled by Smart Manufacturing. *ACS Energy Letters* **2020,** *5* (9), 3069-3100.
10. Kamat, P. V., Quantum Dot Solar Cells. The Next Big Thing in Photovoltaics. *The Journal of Physical Chemistry Letters* **2013,** *4* (6), 908-918.
11. Hu, L.; Zhao, Q.; Huang, S.; Zheng, J.; Guan, X.; Patterson, R.; Kim, J.; Shi, L.; Lin, C.-H.; Lei, Q.; Chu, D.; Tao, W.; Cheong, S.; Tilley, R. D.; Ho-Baillie, A. W. Y.; Luther, J. M.; Yuan, J.; Wu, T., Flexible and efficient perovskite quantum dot solar cells via hybrid interfacial architecture. *Nature Communications* **2021,** *12* (1), 466.
12. Kim, M. R.; Ma, D., Quantum-Dot-Based Solar Cells: Recent Advances, Strategies, and Challenges. *The Journal of Physical Chemistry Letters* **2015,** *6* (1), 85-99.
13. Smith, A. M.; Nie, S., Semiconductor Nanocrystals: Structure, Properties, and Band Gap Engineering. *Accounts of Chemical Research* **2010,** *43* (2), 190-200.
14. Alivisatos, A. P., Semiconductor Clusters, Nanocrystals, and Quantum Dots. *Science* **1996,** *271* (5251), 933-937.
15. Zhu, H.; Lian, T., Wavefunction engineering in quantum confined semiconductor nanoheterostructures for efficient charge separation and solar energy conversion. *Energy & Environmental Science* **2012,** *5* (11), 9406-9418.
16. Kilina, S.; Velizhanin, K. A.; Ivanov, S.; Prezhdo, O. V.; Tretiak, S., Surface Ligands Increase Photoexcitation Relaxation Rates in CdSe Quantum Dots. *ACS Nano* **2012,** *6* (7), 6515-6524.
17. Hines, D. A.; Kamat, P. V., Recent Advances in Quantum Dot Surface Chemistry. *ACS Applied Materials & Interfaces* **2014,** *6* (5), 3041-3057.

18. Peterson, M. D.; Cass, L. C.; Harris, R. D.; Edme, K.; Sung, K.; Weiss, E. A., The Role of Ligands in Determining the Exciton Relaxation Dynamics in Semiconductor Quantum Dots. *Annual Review of Physical Chemistry* **2014,** *65* (1), 317-339.
19. Schnitzenbaumer, K. J.; Labrador, T.; Dukovic, G., Impact of Chalcogenide Ligands on Excited State Dynamics in CdSe Quantum Dots. *The Journal of Physical Chemistry C* **2015,** *119* (23), 13314-13324.
20. Turner, J. J., Infrared vibrational band shapes in excited states. *Coordination Chemistry Reviews* **2002,** *230* (1), 213-224.
21. Leger, J. D.; Friedfeld, M. R.; Beck, R. A.; Gaynor, J. D.; Petrone, A.; Li, X.; Cossairt, B. M.; Khalil, M., Carboxylate Anchors Act as Exciton Reporters in 1.3 nm Indium Phosphide Nanoclusters. *The Journal of Physical Chemistry Letters* **2019,** *10* (8), 1833-1839.
22. Kennehan, E. R.; Munson, K. T.; Grieco, C.; Doucette, G. S.; Marshall, A. R.; Beard, M. C.; Asbury, J. B., Exciton–Phonon Coupling and Carrier Relaxation in PbS Quantum Dots: The Case of Carboxylate Ligands. *The Journal of Physical Chemistry C* **2021,** *125* (41), 22622-22629.
23. Guyot-Sionnest, P.; Wehrenberg, B.; Yu, D., Intraband relaxation in CdSe nanocrystals and the strong influence of the surface ligands. *The Journal of Chemical Physics* **2005,** *123* (7), 074709.
24. Mack, T. G.; Jethi, L.; Andrews, M.; Kambhampati, P., Direct Observation of Vibronic Coupling between Excitonic States of CdSe Nanocrystals and Their Passivating Ligands. *The Journal of Physical Chemistry C* **2019,** *123* (8), 5084-5091.
25. Limonov, M. F.; Rybin, M. V.; Poddubny, A. N.; Kivshar, Y. S., Fano resonances in photonics. *Nature Photonics* **2017,** *11* (9), 543-554.
26. Frontiera, R. R.; Gruenke, N. L.; Van Duyne, R. P., Fano-Like Resonances Arising from Long-Lived Molecule-Plasmon Interactions in Colloidal Nanoantennas. *Nano Letters* **2012,** *12* (11), 5989-5994.
27. Miroshnichenko, A. E.; Flach, S.; Kivshar, Y. S., Fano resonances in nanoscale structures. *Reviews of Modern Physics* **2010,** *82* (3), 2257-2298.
28. Luk'yanchuk, B.; Zheludev, N. I.; Maier, S. A.; Halas, N. J.; Nordlander, P.; Giessen, H.; Chong, C. T., The Fano resonance in plasmonic nanostructures and metamaterials. *Nature Materials* **2010,** *9* (9), 707-715.
29. Wang, M.; Krasnok, A.; Zhang, T.; Scarabelli, L.; Liu, H.; Wu, Z.; Liz-Marzán, L. M.; Terrones, M.; Alù, A.; Zheng, Y., Tunable Fano Resonance and Plasmon–Exciton Coupling in Single Au Nanotriangles on Monolayer WS2 at Room Temperature. *Advanced Materials* **2018,** *30* (22), 1705779.
30. Agrawal, A.; Singh, A.; Yazdi, S.; Singh, A.; Ong, G. K.; Bustillo, K.; Johns, R. W.; Ringe, E.; Milliron, D. J., Resonant Coupling between Molecular Vibrations and Localized Surface Plasmon Resonance of Faceted Metal Oxide Nanocrystals. *Nano Letters* **2017,** *17* (4), 2611-2620.
31. Yang, W.; Liu, Y.; Edvinsson, T.; Castner, A.; Wang, S.; He, S.; Ott, S.; Hammarström, L.; Lian, T., Photoinduced Fano Resonances between Quantum Confined Nanocrystals and Adsorbed Molecular Catalysts. *Nano Letters* **2021,** *21* (13), 5813-5818.
32. Yang, W.; Vansuch, G. E.; Liu, Y.; Jin, T.; Liu, Q.; Ge, A.; Sanchez, M. L. K.; K. Haja, D.; Adams, M. W. W.; Dyer, R. B.; Lian, T., Surface-Ligand "Liquid" to "Crystalline" Phase Transition Modulates the Solar H2 Production Quantum Efficiency of CdS Nanorod/Mediator/Hydrogenase Assemblies. *ACS Applied Materials & Interfaces* **2020,** *12* (31), 35614-35625.
33. Kirkwood, N.; Monchen, J. O. V.; Crisp, R. W.; Grimaldi, G.; Bergstein, H. A. C.; du Fossé, I.; van der Stam, W.; Infante, I.; Houtepen, A. J., Finding and Fixing Traps in II–VI and III–V Colloidal Quantum Dots: The Importance of Z-Type Ligand Passivation. *Journal of the American Chemical Society* **2018,** *140* (46), 15712-15723.
34. Kennehan, E. R.; Munson, K. T.; Grieco, C.; Doucette, G. S.; Marshall, A. R.; Beard, M. C.; Asbury, J. B., Influence of Ligand Structure on Excited State Surface Chemistry of Lead Sulfide Quantum Dots. *Journal of the American Chemical Society* **2021,** *143* (34), 13824-13834.

35. Takeda, H.; Koike, K.; Morimoto, T.; Inumaru, H.; Ishitani, O., Photochemistry and photocatalysis of rhenium(I) diimine complexes. In *Advances in Inorganic Chemistry*, Eldik, R. v.; Stochel, G., Eds. Academic Press: 2011; Vol. 63, pp 137-186.
36. Kiefer, L. M.; Kubarych, K. J., Solvent-Dependent Dynamics of a Series of Rhenium Photoactivated Catalysts Measured with Ultrafast 2DIR. *The Journal of Physical Chemistry A* **2015,** *119* (6), 959-965.
37. Huang, J.; Stockwell, D.; Huang, Z.; Mohler, D. L.; Lian, T., Photoinduced Ultrafast Electron Transfer from CdSe Quantum Dots to Re-bipyridyl Complexes. *Journal of the American Chemical Society* **2008,** *130* (17), 5632-5633.
38. Zhu, H.; Yang, Y.; Wu, K.; Lian, T., Charge Transfer Dynamics from Photoexcited Semiconductor Quantum Dots. *Annual Review of Physical Chemistry* **2016,** *67* (1), 259-281.
39. Takeda, H.; Koike, K.; Inoue, H.; Ishitani, O., Development of an Efficient Photocatalytic System for CO2 Reduction Using Rhenium(I) Complexes Based on Mechanistic Studies. *Journal of the American Chemical Society* **2008,** *130* (6), 2023-2031.
40. Herlihy, D. M.; Waegele, M. M.; Chen, X.; Pemmaraju, C. D.; Prendergast, D.; Cuk, T., Detecting the oxyl radical of photocatalytic water oxidation at an n-SrTiO3/aqueous interface through its subsurface vibration. *Nature Chemistry* **2016,** *8* (6), 549-555.
41. Gebre, S. T.; Kiefer, L. M.; Guo, F.; Yang, K. R.; Miller, C.; Liu, Y.; Kubiak, C. P.; Batista, V. S.; Lian, T., Amine Hole Scavengers Facilitate Both Electron and Hole Transfer in a Nanocrystal/Molecular Hybrid Photocatalyst. *Journal of the American Chemical Society* **2023,** *145* (5), 3238-3247.
42. Zhu, H.; Song, N.; Lian, T., Wave Function Engineering for Ultrafast Charge Separation and Slow Charge Recombination in Type II Core/Shell Quantum Dots. *Journal of the American Chemical Society* **2011,** *133* (22), 8762-8771.
43. Zhu, H.; Song, N.; Rodríguez-Córdoba, W.; Lian, T., Wave Function Engineering for Efficient Extraction of up to Nineteen Electrons from One CdSe/CdS Quasi-Type II Quantum Dot. *Journal of the American Chemical Society* **2012,** *134* (9), 4250-4257.
44. *Nanocrystal Quantum Dots*. 2 ed.; CRC Press: Boca Raton, 2010; p 460.

Chapter 5. Effect of Distance on Fano Resonance Coupling in CdSe-ReCxA and CdSe/ZnS-ReS_2 Complexes

5.1 Introduction

Semiconductor nanocrystals (NCs) have various diverse applications in areas such as solar fuel generation[1-4], photovoltaics[5-8], and light emitting diodes[9-12]. Quantum dots (QDs) in particular, have various unique optical properties owed to their quantum confinement, including being excellent light harvesters as well as the ability to manipulate their energetic band structures through wavefunction engineering.[13-15] In addition, their surface composition and structure can greatly affect the NC's photophysical properties, and therefore performance in devices or for photocatalysis.[16-21] Surface ligands play a pivotal role for the formation of the nanocrystals and the types of ligands, as well as their exchange can affect the NC charge carrier lifetimes. There has been a multitude of work investigating charge transfer processes between QDs and varying types of ligands or surface bound species, such as electron acceptors and hole scavengers. These studies demonstrate that charge transfer and intraband relaxation can be greatly affected by processes such as hole and electron trapping and Auger recombination, originating from QD-species interfacial interactions. Oftentimes, many of these ligands and other molecules have discrete vibrational signatures that can also be monitored to observe directly interfacial interactions from the point of view of these molecules.[22-26] This is useful to gain a full picture of what occurs in these types of systems.

When molecules are bound to QDs, vibrational modes of molecules and intraband transition of QDs can be coupled, leading to the phenomenon called Fano resonance (FR).[27-28] FR is a phenomenon where a discrete state mixes with a continuum state typically yielding a distinctive derivative shaped feature, and described by the Fano parameter q, which serves as a measure of

lineshape asymmetry. This kind of phenomenon has been observed in many different systems, including plasmonic nanomaterials.[29-33] Frontiera *et al.* investigated colloidal nanoantennas with *trans*-1,2-bis(4-pyridyl)-ethylene as a reporter molecule for surface enhanced Raman spectroscopy, where they perceived the phase of the Fano lineshape changed with the plasmon energy and found that the coupling does not affect molecular vibrational coherence lifetime.[34] Since such surface interactions have the potential to affect QD performance, in particular photocatalytic performance, we aim to further understand FR coupling in QD-molecular catalyst complexes. However, work with this type of system is few and far between.

Here, we investigate the effect of distance on FR coupling in CdSe-rhenium and CdSe/ZnS-rhenium catalyst complexes. We study this effect from both the QD and catalyst points of view. In terms of the catalyst, we use variations of the $Re(CO)_3$(bpy-COOH)Cl (ReC0A) catalyst, where CH_2 groups are added between the bipyridyl and carboxylic acid groups of the complex denoted as $Re(CO)_3$(bpy-$(CH_2)_x$-COOH)Cl (x = 0, 1, 2, 3) These are bound to a small CdSe QD. With regards to the QDs, we grow ZnS shells of different thicknesses on large CdSe QDs and bind ReS_2 complexes to the surface. We find that with increasing shell thickness and distance from the core, the FR amplitude indeed decreases. However, with the varying linker length in the ReCxA complexes, FR is observed, but the trend is not as straightforward.

5.2 Results and Discussion

5.2.1 Characterization of Quantum Dot and Rhenium Complexes

CdSe QDs and CdSe/ZnS core shell structures were used in this study with various rhenium complexes bound to the surface to systematically investigate the effect of distance on FR coupling. First, we modified the ReC0A catalyst to insert a CH_2 group between the bipyridine and carboxylic

acid groups. We refer to these complexes as ReCxA, where x = 0, 1, 2, and 3, corresponding to the number of CH_2 groups inserted in the catalyst ($Re(CO)_3(bpy\text{-}(CH_2)_x\text{-}COOH)Cl$).[35-36] The structures of these complexes are shown in Figure S5.1. Both UV-Vis and FTIR spectra were obtained for all complexes (Figure S5.2). The UV-Vis spectra show both the metal-to-ligand charge transfer (MLCT) state and π to π^* transition of the bipyridine.[37] The MLCT state for ReC0A appears at 400 nm compared to the other complexes (365 nm) due to the conjugation of the ReC0A shifting the transition energy. The π to π^* transition seems to stay at roughly the same energy (~310 nm). The CO stretching modes of the complexes are also shifted in energy compared to ReC0A in acetonitrile (MeCN). These complexes have three CO stretching modes; the symmetric (2023 cm^{-1}), asymmetric (1915 cm^{-1}), and out of phase symmetric (1896 cm^{-1}) modes. For ReC0A, these modes are shifted to 2025, 1922, and 1905 cm^{-1}, respectively, again, likely due to the difference in conjugation between these molecules. ReCxA were bound to a CdSe QD with an exciton absorbance at 505 nm, corresponding to a size of 2.4 nm. UV-Vis and FTIR spectra are shown in Figure S5.3. Visible spectra show that after the addition of ReCxA complexes, the exciton absorbance position remains the same, with an increase in the scattering of the samples. The hexanes absorbance in the CdSe hexanes sample is at the same frequency as the ReCxA on CdSe. The solvent was subtracted to observe the contribution of the absorbance of ReCxA molecules on the CdSe surface.

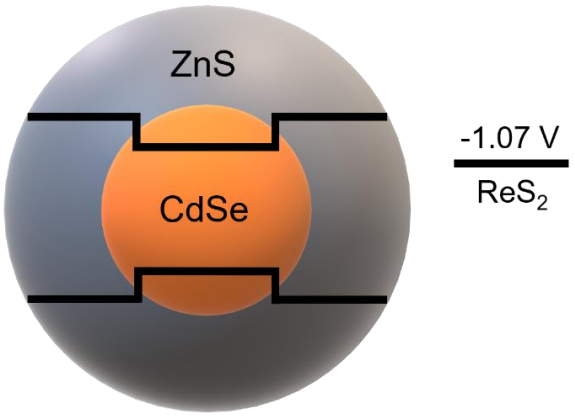

Figure 5.1. Energy diagram showing the type 1 band alignment of CdSe/ZnS with ReS_2.

To investigate the distance dependence of FR from the QD point of view, several core shell structures were made. First, oleate capped CdSe QDs were synthesized following literature procedures and resulted in an exciton absorbance centered at 550 nm, corresponding to a size of 3 nm. ZnS shells were grown onto the CdSe core, as described in the supporting information (5.4.1) to obtain a type 1 band alignment (Figure 5.1).[38] The number of growth cycles to form ZnS shells resulted in what was expected to be 1 monolayer (ML), 3 ML, and 6 ML of ZnS on the CdSe core. Transmission electron microscopy (TEM) was used to determine the size of each nanocrystal and resulted in sizes of 3.15 ± 0.41 (CdSe core), 3.79 ± 0.46 (CdSe/ZnS 1ML), 3.92 ± 0.45 (CdSe/ZnS 3ML), and 4.90 ± 0.53 (CdSe/ZnS 6ML) nm. These samples are hereafter referred to as CdSe core, CdSe/$ZnS_{0.64}$, CdSe/$ZnS_{0.77}$, and CdSe/$ZnS_{1.75}$, respectively, corresponding to the shell thickness grown. TEM images and size distributions are shown in Figure S5.4 and S5.5. In the UV-Vis (Figure 5.2a), between the CdSe core and CdSe/$ZnS_{0.64}$, there is a slight shift of 5 nm (550 to 555 nm). As the shell thickness increases, the peak is significantly broadened and red shifted to 565 nm. This is due to leakage of the core exciton wavefunction into the ZnS shell.[39] The PL data shown is under both 400 and 520 nm excitation (Figure 5.2b and c respectively). Upon growth of the shells, there is a dramatic increase in the PL compared to the CdSe core (blue) due to passivation of trap states. As the shell thickness increases, the PL is further increased, indicating that traps are further passivated, resulting in less nonradiative emission for both cases. The PL increases by approximately 16.2 times under 520 excitation and 11.5 times under 400 nm light between the core and CdSe/$ZnS_{1.75}$ samples.

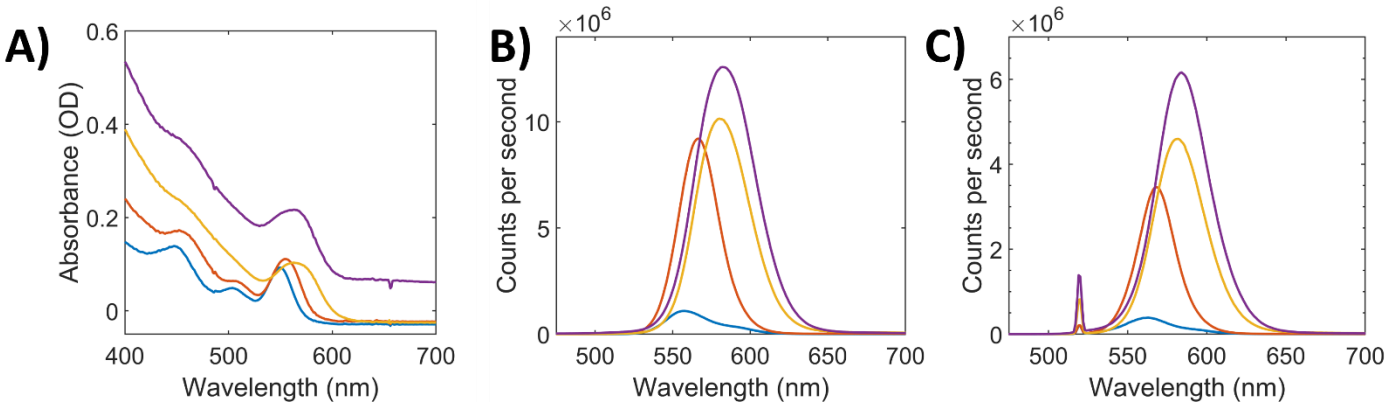

Figure 5.2. Steady state characterization of CdSe core and CdSe/ZnS QDs. [blue: CdSe core; red: $CdSe/ZnS_{0.64}$; yellow: $CdSe/ZnS_{0.77}$; purple: $CdSe/ZnS_{1.75}$] A) UV-Vis of QDs. The CdSe core absorbance is centered at 550 nm and $CdSe/ZnS_{0.64}$ is slightly broadened and shifted to 555 nm. Both $CdSe/ZnS_{0.77}$ and $CdSe/ZnS_{1.75}$ are more significantly broadened and shifted to 565 nm. B) PL spectra of the QDs excited at 400 nm. C) PL spectra of the QDs excited at 520 nm.

In addition, time correlated single photon counting (TCSPC) was performed to characterize the PL lifetime of the CdSe core and CdSe/ZnS QDs. The samples used had UV-Vis and PL spectra seen in Figure 5.2. Experiments were conducted under 400 nm excitation for each sample with kinetics shown in Figure 5.3a. It is apparent that as the shell thickness increases, the PL lifetime also increases, confirming the steady state PL results. The thicker the shell, the more traps are passivated, resulting in less nonradiative emission, and therefore an enhanced PL lifetime. The kinetics were fit to a multiexponential resulting in time constants that are shown in Table S5.1.

The complex used for this study was $[Re(SS\text{-}bpy)(CO)_3Cl]$ (ReS_2), a rhenium complex with a disulfide bridge across the bipyridyl group (Figure S5.6a).[40] Upon addition to the QDs, the disulfide bond breaks, resulting in the two thiols acting as the binding groups. This complex was used instead of ReC0A due to its superior binding ability compared to carboxylic acid groups. UV-Vis and FTIR

spectra show that the MLCT state absorbs at 420 nm with the CO stretching modes appearing at frequencies typical for these types of rhenium complexes (ReC0A, etc) (Figure S5.6b-c). ReS_2 was then added to the QDs, UV-Vis spectra taken (Figure S5.7) and transient absorption (TA) performed. As with the CdSe-ReCxA complexes, there is no change in spectra after catalyst binding except for an increase in the scattering of the samples. The samples were then made into films on TiO_2-sapphire (Figure S5.14) and transient infrared spectroscopy (TRIR) was done. As the TiO_2 has a large band gap and the conduction band is much higher than CdSe, we can assume there is no electron transfer occurring between the two.

5.2.2 Characterization of QD-Rhenium Complexes Using Visible Transient Spectroscopy

TA was first performed on the CdSe-ReCxA complexes to characterize their exciton dynamics. These complexes were excited under 500 nm pump, outside the range of any MLCT states so as not to directly excite the Re catalysts. After visible excitation, an exciton bleach formed, due to state filling of the 1S conduction band (CB) state (Figure S5.8).[41] In the case of CdSe, the kinetics were long-lived within the time of the experiment, 1.7 ns (Figure 5.3b). After addition of the catalysts, we would expect that electron transfer from the QD to the ReC0A would occur the fastest in comparison to the other complexes, because it is the closest to the QD surface and has no CH_2 linker groups. This is exactly what we observe. The decay of the exciton bleach in the ReC0A case is faster than the CdSe only sample, indicating electron transfer occurring. The half-life of CdSe-ReC0A was determined to be 198 ps. However, within 1.7 ns, the decay of the other ReCxA molecules with CdSe does not reach half the normalized amplitude needed to determine the half-lives. Looking at the kinetics, we can determine that ReC0A has the fastest rate of electron transfer, with ReC2A and ReC3A being similarly slower, and ReC1A having the same kinetics as the QD by itself. One would expect that ReC1A would

have faster bleach recovery that ReC2A or ReC3A, however, it seems that with more CH_2 groups, there is more flexibility in the complex, allowing for the bipyridine or Re center to bend over and get nearer to the surface, making the electron transfer quicker.

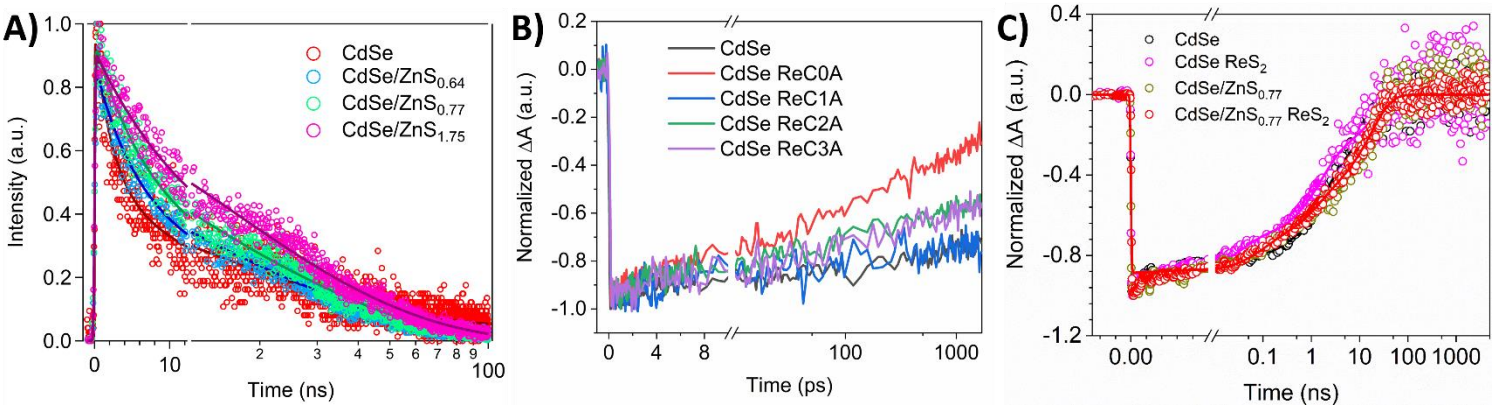

Figure 5.3. TA Kinetics of CdSe-ReCxA, CdSe-ReS_2 and CdSe/ZnS-ReS_2 complexes along with TCSPC of the core shell QDs. A) TCSPC data of the core shell structures. As the shell gets thicker, the PL lifetime increases due to trap passivation B) TA Kinetics of CdSe-ReCxA samples after 500 nm excitation, traced at 461 nm. C) TA kinetics of the CdSe core, CdSe-ReS_2, CdSe/$ZnS_{0.77}$, and CdSe/$ZnS_{0.77}$-ReS_2. Samples with ReS_2 show slightly faster kinetics, alluding to a small percentage of electron transfer.

Lastly, ReS_2 was added to the CdSe core and CdSe/ZnS QDs for TA. Since the CdSe core was larger than the QD used for the CdSe-ReCxA samples, our pump wavelength was 520 nm, once again, to avoid excitation of the catalyst. As before, after excitation, an exciton bleach appears due to the 1S state filling of the CB (Figure S5.9). It seems that for each sample, upon addition of ReS_2, the bleach recovery occurred slightly faster (Figure 5.3c, S5.10). This could be from a small percentage of electrons transferring to the catalyst, from slight electron trapping due the ReS_2 binding to the surface or some combination of both. Due to the position of the exciton absorbance (550 nm) we believe that electron transfer is only slightly possible because of the reduction potential of the CB (~1 V vs

NHE).[42-43] The reduction potential for ReS_2 is at -1.07 V vs NHE[40], so because they are so close in energy, it might still be possible for electron transfer to occur. The kinetics were fit to a triexponential resulting in amplitude weighted average time constants shown in Table S5.2.

5.2.3 Fano Resonance as a Function of Distance: Catalyst Modifications

TRIR experiments were first performed with the CdSe-ReCxA complexes in hexanes under high pump fluence at 520 nm. In the case of CdSe in hexanes, we would expect that there would be no FR due to the absence of the ReCxA high frequency mode. However, two large positive absorptions appear at ~2028 and 2048 cm^{-1}, which correspond to the absorption of hexanes, indicating solvent coupling to the QD. The first peak is at the same position as the CO high frequency mode, while the second appears as a shoulder in the FTIR (Figure S5.3b) and is solely due to the hexanes. After ReC0A is added, there is an increase in the amplitude of the peak at 2028 cm^{-1}, indicating there is coupling between the CO mode and the 1S to 1P intraband transition in the QD CB, but that it is on top of the hexanes absorption (Figure S5.11). This is seen for every CdSe-ReCxA complex. In addition, at later time, we observe that the FR signal has decayed, and with it, a peak at ~2010 and a bleach at ~2030 cm^{-1} corresponds to the singly reduced species of the catalyst, as we have previously observed. This is not seen for any other CdSe-ReCxA complexes because very little electron transfer occurs.

The following equation[42] was used to globally fit the FR to obtain the value of the asymmetry parameter, q:

$$\Delta A = \sum_i \left[A_i \frac{(q_i + \varepsilon_i)^2}{1+\varepsilon_i{}^2} - A_i{}' \frac{2}{\pi}\left(\frac{\Gamma_i}{4(v-v_{0,i})^2 + \Gamma_i{}^2}\right)\right] + PA - IR(v) \qquad (1)$$

where the first and second terms correspond to the absorption due to Fano resonance and the Lorentzian absorption, respectively. The PA-IR term corresponds to the IR signal originating from

the QD intraband electron signal. A_i and A_i' are the amplitudes of the Fano and Lorentzian terms, respectively. q_i is the coupling parameter, Γ_i is the width of the IR transition, and $v_{0,i}$ is the peak position of the vibrational feature. ε_i is the detuning term where $\varepsilon_i = 2\left(v - v_{0,i}\right)/\Gamma_i$. Since the hexanes and CO FR signals overlap, we have subtracted the solvent coupling to obtain the contribution only from the ReCxA FR. We fit the solvent FR to eq 1 to get the value of the Fano parameter, q, getting the ratio of the amplitudes between the peaks, and using those to fit the solvent peak at 2048 cm^{-1}, and therefore the amplitude of the solvent FR at 2028 cm^{-1} for subtraction. This process is described in more detail in 5.4.4. The spectra shown hereafter are all solvent subtracted.

The TRIR spectra for these samples are shown in Figure 5.4, with their q values described in Table 5.1. Going from CdSe-ReC0A to CdSe-ReC1A, the FR amplitude decreases, indicating that the addition of a CH_2 group, and therefore distance, does affect the FR lineshape. However, for CdSe-ReC2A, the asymmetry parameter increases to more than CdSe-ReC0A, while the CdSe-ReC3A FR asymmetry parameter q is the same as CdSe-ReC0A. The growth in the q value for these two samples is unexpected because we would expect that with more CH_2 groups, and therefore distance, the FR coupling should decrease because of less overlap between the QD exciton wavefunction and the CO modes. However, that is not what we observe here. We attribute the increase in FR for the ReC2A and ReC3A complexes to the flexibility of these complexes compared to the other two. Since they have more degrees of freedom because of increased CH_2 groups, we believe that the molecules can bend over and possibly lay flat on the QD surface, putting the CO groups closer to the surface. This would result in greater overlap of the exciton wavefunction and CO modes than CdSe-ReC1A. This trend suggests that FR, in this case, is a through space phenomenon.

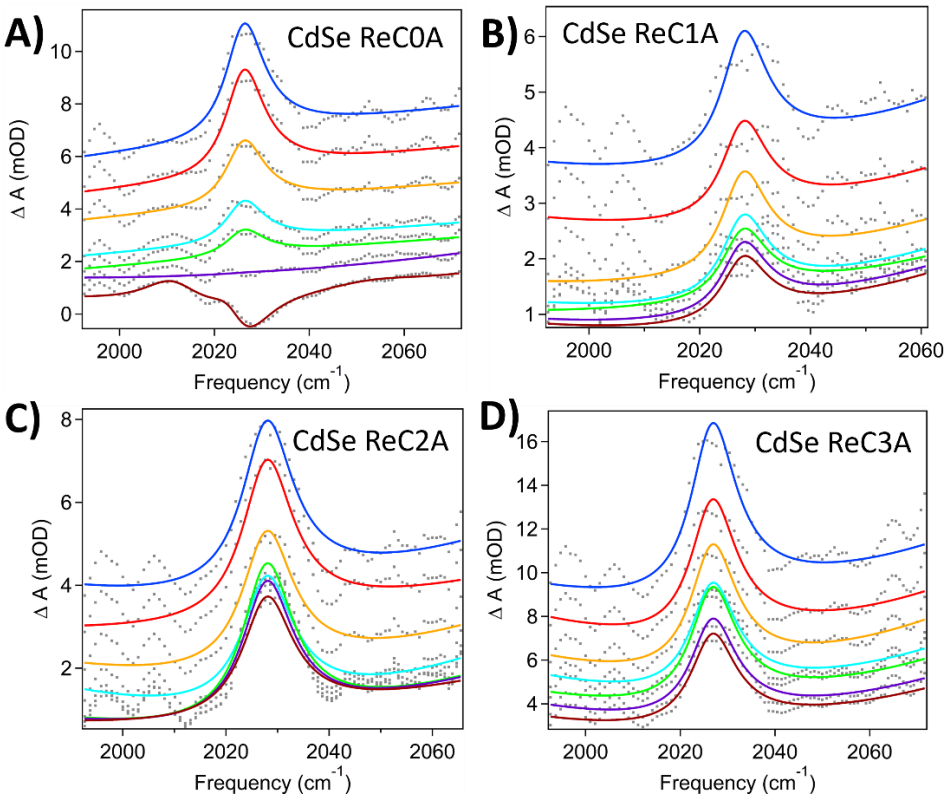

Figure 5.4. Solvent subtracted TRIR spectra, showing the FR that arises from the CdSe CB electron and ReCxA vibrational modes (blue: 0-1 ps, red: 2-5 ps, yellow: 5-15 ps, purple: 25-100 ps, green: 100-200 ps, light blue: 400-800 ps, burgundy: 800-1670 ps). A) CdSe-ReC0A. As time goes on, the FR signal decays and reveals the reduced species of the catalyst as previously observed. B) CdSe-ReC1A. FR coupling occurs here, but with a smaller amplitude, indicating weaker coupling. C) CdSe-ReC2A. D) CdSe-ReC3A. It seems that for these two samples, the FR has increased in comparison to CdSe-ReC1A, likely due to increased degrees of freedom in these molecules allowing for the CO modes to bend closer to the QD surface.

Table 5.1. Asymmetry values (q) of CdSe-ReCxA complexes globally fit by equation 1.

CdSe-ReC0A	CdSe-ReC1A	CdSe-ReC2A	CdSe-ReC3A
12.6 ± 1.08	9.14 ± 1.19	17.1 ± 1.86	12.7 ± 0.93

5.2.4 Effect of Shell Thickness on Fano Resonance

To study distance dependence from the side of the QD, we have synthesized oleate capped CdSe with an exciton absorption centered at 550 nm. ZnS shells were grown onto the QD, to produce three core shell structures: CdSe/$ZnS_{0.64}$, CdSe/$ZnS_{0.77}$, and CdSe/$ZnS_{1.75}$. This notation is used to describe the thickness of the ZnS shell for each sample. For TRIR experiments, ReS_2 was added to each QD and then both spin-coated and drop-cast onto TiO_2 to create films. This method was used to circumvent the hexanes absorption in the spectra, so that the signal would arise from only the FR due to ReS_2. Films were made for both QD only and QD-ReS_2 samples. QD only TRIR spectra are shown in Figure S5.12. As expected, there is a broad absorption across the infrared window probed corresponding to the intraband transition within the QD CB. This signal is featureless, as we would expect due to there being no molecular absorption in that region. Each spectrum was fitted to a polynomial for use in equation 1.

After adding ReS_2 to the QDs, we observe the growth of FR signals, as we expect (Figure 5.5). Since the films are not uniform because of the drop casting step, we calibrated the ReS_2 absorption intensity by moving the films to spots where the intensities would be similar (Figure S5.13). This was to eliminate any effect of differing ReS_2 concentrations, for which we know is a parameter that can change FR asymmetry value. Peaks appear between 2030 and 2038 cm^{-1} corresponding to FR coupling. Both the amplitudes of the FR signal in Figure 5.5 and the q values in Table 5.2, demonstrate that the FR increases with increasing shell thickness. CdSe/ZnS core shell structures have type 1 band alignment (Figure 5.1) meaning that the valence band (VB) and CB are offset compared to the core QD.[38] This restricts the exciton wavefunction to the core, making this an ideal system for this type of study. The trend we observe here is clear evidence for the distance dependence of the FR phenomenon. The q value of the core is significantly larger than the core shell QDs, which we expect

considering the catalyst is the closest to the surface that it can get. The next two sizes of CdSe/ZnS QDs have similar asymmetry parameter values, however this is because there is only a small difference in the ZnS shells (0.64 vs 0.77 nm). CdSe/$ZnS_{0.77}$-ReS_2 is slightly smaller than CdSe/$ZnS_{0.64}$. The most drastic change in the q values is seen with CdSe/$ZnS_{1.75}$-ReS_2. With the thickest ZnS shell, the FR amplitude is dramatically smaller than CdSe-ReS_2, and much smaller than the other two core shell structures. This demonstrates a clear trend regarding FR as a function of distance. The reason for this is, once again, because of the interaction between the QD wavefunction and the catalyst vibrational modes. Since the core shell structures have a type 1 band structure, the ZnS shell blocks the exciton wavefunction from penetrating the CdSe/ZnS surface, localizing the exciton to the CdSe core. As the shell thickness increases, the molecule gets farther away from the surface, further separating the CO modes from the CdSe core, lessening the electronic-vibrational overlap of the two. The thicker the shell, the less the QD wavefunction can penetrate the surface, and by the time we arrive at the thickest sample, it is likely that the wavefunction is significantly blocked in comparison to the thinnest CdSe/ZnS. As with the ReCxA tests, this provides further evidence that FR is a through space phenomena.

While we describe the FR as arising from a charge transfer mechanism depending on the overlap of the QD electron wavefunction and the catalyst LUMO, it is also possible for the FR to manifest through a dipole-dipole interaction. We are currently developing a model to elucidate this and describe the mechanism of the FR coupling and how the asymmetry parameter q changes as a result.

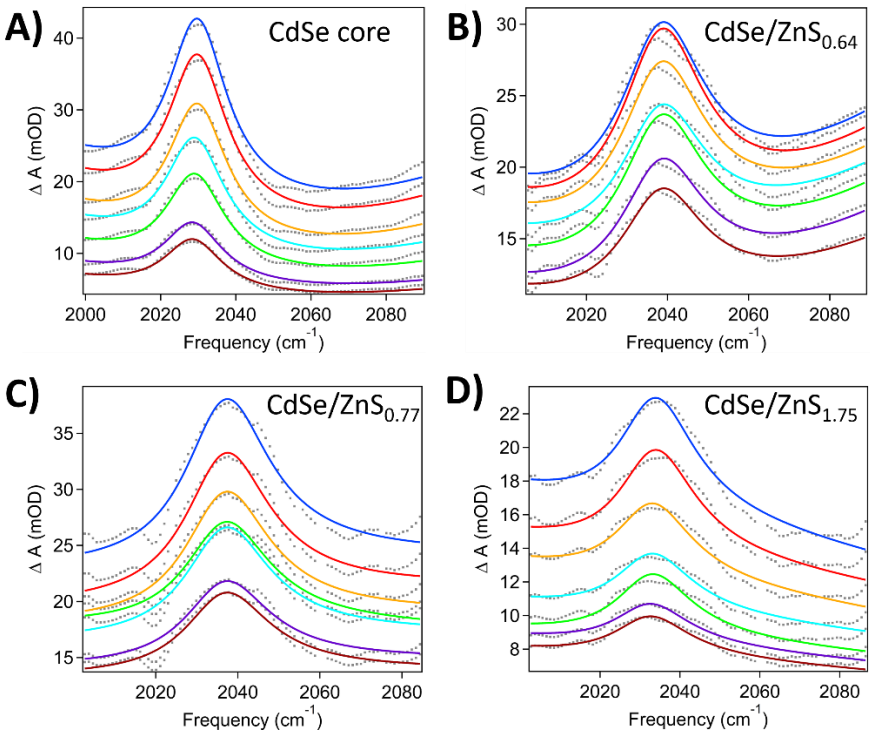

Figure 5.5. TRIR spectra of QDs with ReS_2 showing FR coupling and globally fitted to equation 1. (blue: 0-1 ps, red: 2-5 ps, yellow: 5-15 ps, purple: 25-100 ps, green: 100-200 ps, light blue: 400-800 ps, burgundy: 800-1670 ps) A) CdSe-ReS_2 B) CdSe/$ZnS_{0.64}$-ReS_2 C) CdSe/$ZnS_{0.77}$-ReS_2 D) CdSe/$ZnS_{1.75}$-ReS_2. With increasing shell thickness, the FR signal decreases.

Table 5.2. Coupling values for QD-ReS_2 from globally fit TRIR spectra.

CdSe core	**CdSe/$ZnS_{0.64}$**	**CdSe/$ZnS_{0.77}$**	**CdSe/$ZnS_{1.75}$**
78.7 ± 14.2	13.9 ± 0.45	13.1 ± 0.64	10.7 ± 0.50

5.3 Conclusions

In conclusion, we have investigated the effect of distance on the FR asymmetry parameter from both the catalyst and QD's points of view. We used ReCxA complexes with a varying number CH_2 groups as linkers between the catalyst bipyridyl and carboxylic acid groups and found that going from ReC0A to ReC1A, there was a decrease in q, that was promptly reversed in the ReC2A and ReC3A samples. This was due to the flexibility of the catalysts, resulting in the ability for the molecules to bend in such a way that pushes the CO groups closer to the surface than CdSe-ReC1A. Additionally, CdSe and CdSe/ZnS QDs were made with ReS_2 added to the surface to study the effect of shell thickness on FR coupling. We determined that with increasing shell thickness, the FR signal greatly decreased because of the type 1 band structure of the core shell structures. The ZnS shell obstructs the QD wavefunction from reaching the surface and localizes it to the core QD. This decreases the overlap between the CdSe core and molecule, minimizing the FR amplitude as a result. Both these experiments suggest and confirm that FR is a through space phenomena. These results provide us with a greater understanding of interfacial interactions between QD-molecular catalyst assemblies and QD-surface bound molecular complexes.

5.4 Supporting Information

5.4.1 Characterization of Free Rhenium Complexes and Bound to QDs

ReCxA complexes and ReS_2 solutions were made in MeCN and stored in a 4 ^{o}C fridge between uses. UV-Vis spectra were collected in a Starna 1 mm quartz cuvette, while FTIR were taken in a Harrick FTIR cell with a path length of 950 μm.

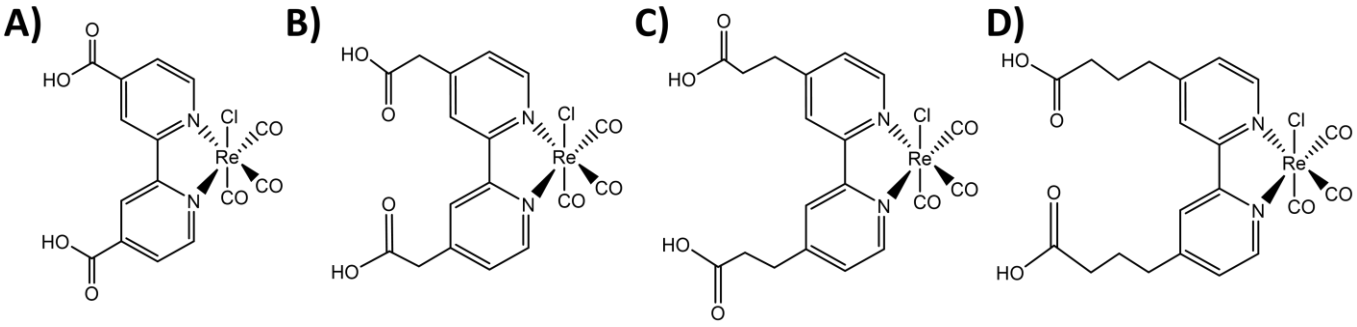

Figure S5.1. ReCxA molecules that are used for different linker length distance study. A) ReC0A B) ReC1A C) ReC2A D) ReC3A.

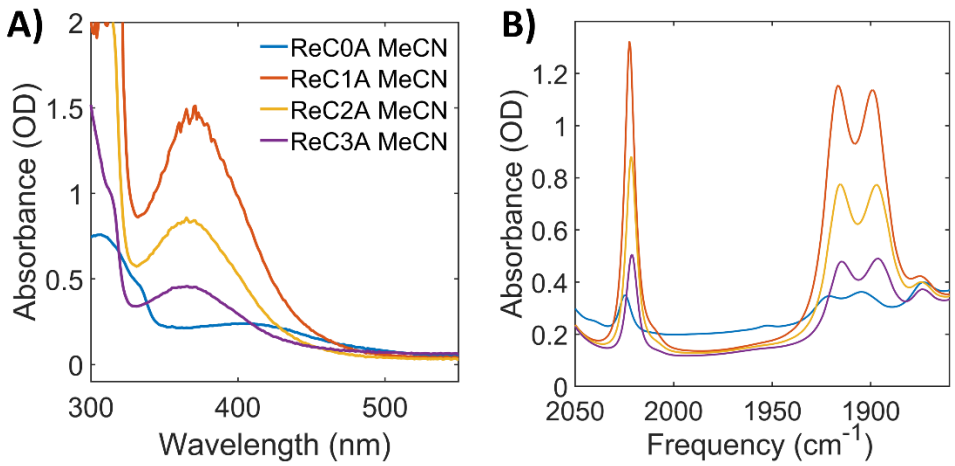

Figure S5.2. UV-Vis and FTIR of ReCxA molecules in MeCN. A) UV-Vis spectra of each complex. ReC0A MLCT transition is red shifted from the other complexes (~ 365 nm) due to pi conjugation, appearing at ~ 400 nm. The π to π^* transition of the bipyridine remains at approximately 310 nm. B) FTIR of ReCxA complexes in MeCN (legend is same as A). There are three vibrational modes corresponding to the symmetric (2025 cm^{-1}), asymmetric (1922 cm^{-1}) and out of phase symmetric (1905 cm^{-1}) stretches of the CO ligands. As you can see, with the addition of CH_2 groups, the CO

modes slightly shift to 2023, 1915, and 1896 cm^{-1} respectively, once again, most likely due to the difference in conjugation of the complexes.

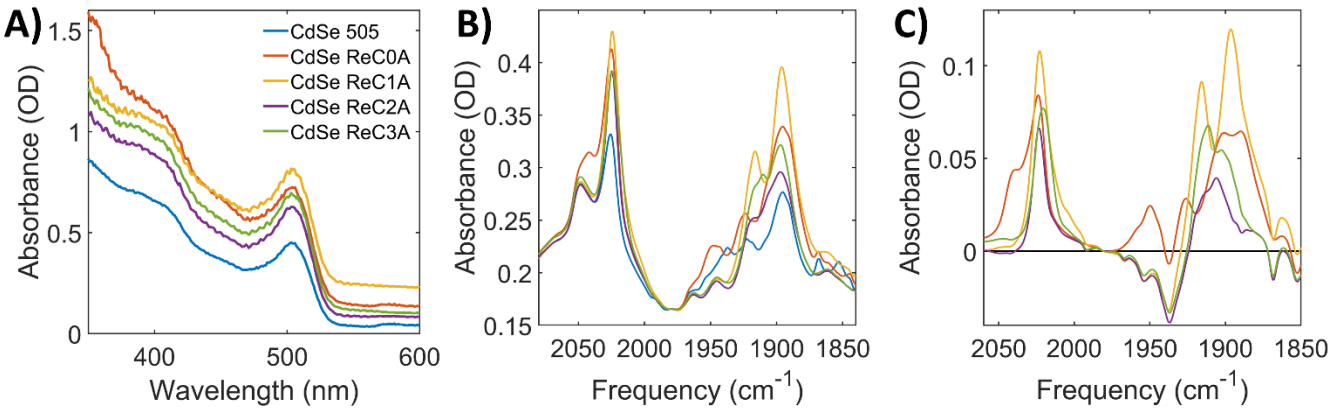

Figure S5.3. Characterization of CdSe (505)-ReCxA in hexanes A) UV-Vis spectra of CdSe-ReCxA. The blue trace shows the original exciton absorbance of the CdSe QD. Upon the addition of 2x ReCxA to the surface, there is some scattering in each sample. B) Unsubtracted FTIR of CdSe-ReCxA (same legend as A). The blue trace of CdSe in hexanes demonstrates that the solvent has an absorbance at the same frequency as ReCxA. In order to observe the amount of complex bound to the surface, the solvent was subtracted from the CdSe-ReCxA samples. C) Solvent subtracted FTIR showing the pure ReCxA bound to the CdSe.

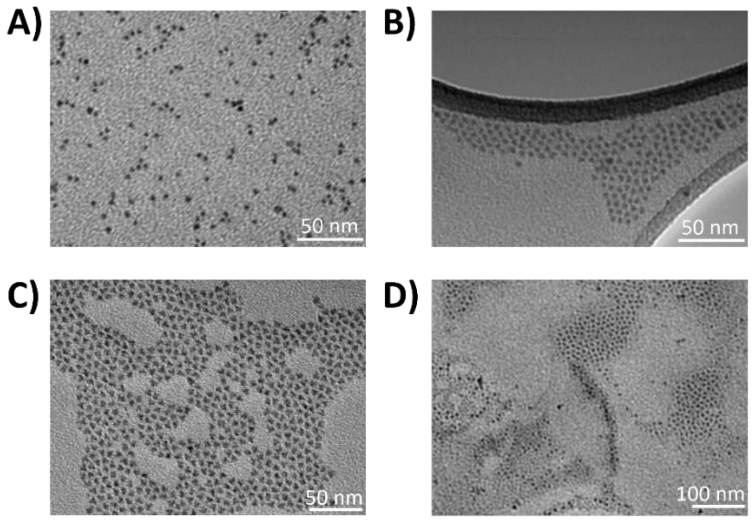

Figure S5.4. TEM images of CdSe core and CdSe/ZnS core shell structures. A) CdSe core. B) $CdSe/ZnS_{0.64}$ which underwent 1 growth cycle, believed to be 1 ML of ZnS. C) $CdSe/ZnS_{0.77}$ which was created with 3 growth cycles, believed to be 3 ML. D) $CdSe/ZnS_{1.75}$ which used 6 growth cycles, expected to be 6 ML.

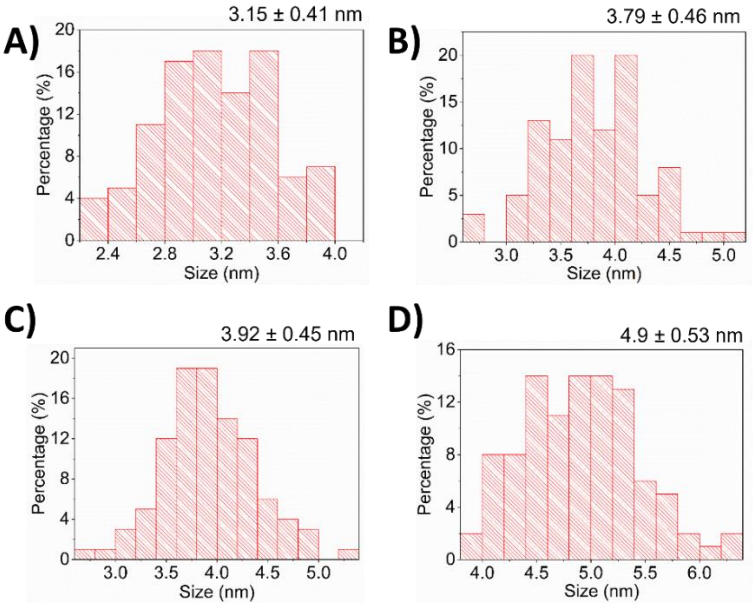

Figure S5.5. Size distributions of CdSe and CdSe/ZnS QDs. A) CdSe core. B) $CdSe/ZnS_{0.64}$ C) $CdSe/ZnS_{0.77}$ D) $CdSe/ZnS_{1.75}$.

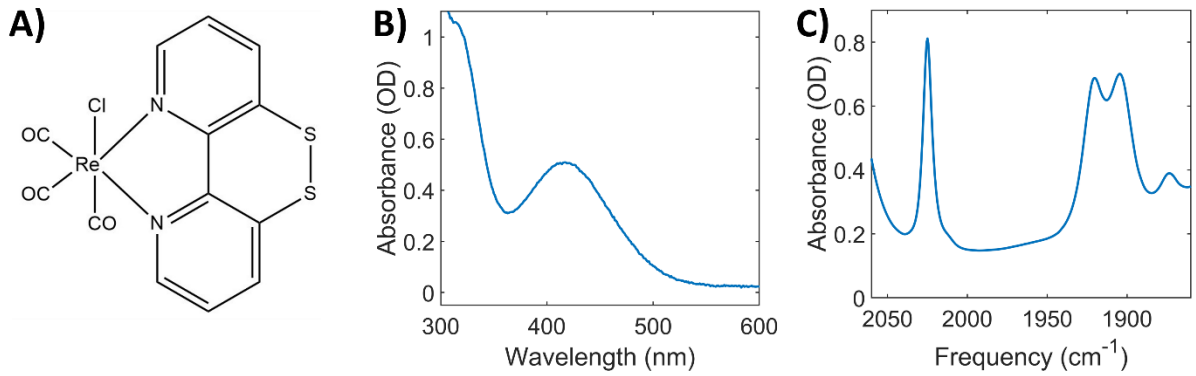

Figure S5.6. Characterization of free ReS_2. A) Structure of ReS_2 B) UV-Vis showing MLCT band centered at 420 nm. C) FTIR showing CO stretching modes located at 2025, 1920, and 1905 cm^{-1}.

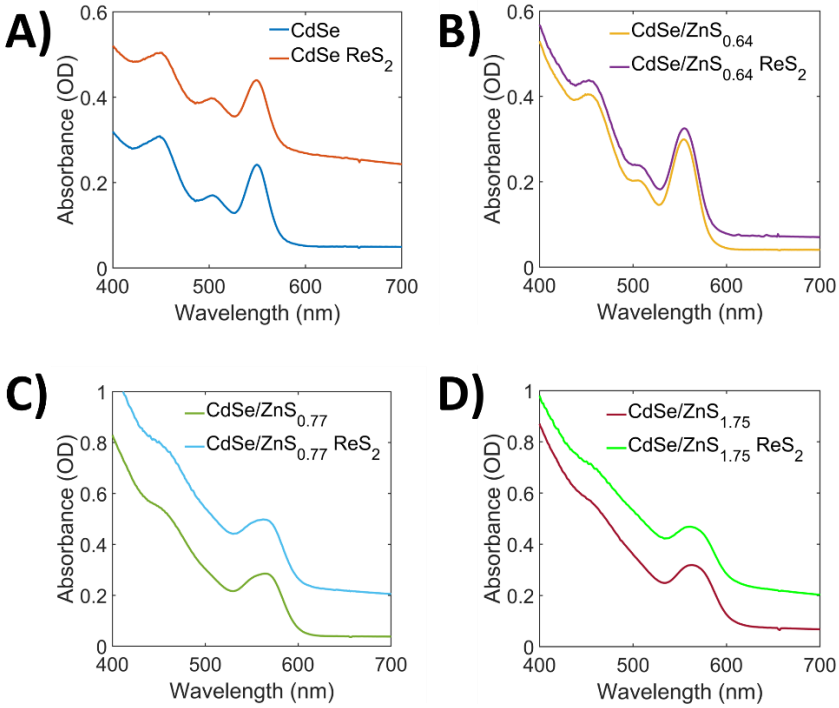

Figure S5.7. UV-Vis spectra of each QD with and without ReS_2. A) CdSe and CdSe-ReS_2 B) CdSe/$ZnS_{0.64}$ and CdSe/$ZnS_{0.64}$-ReS_2 C) CdSe/$ZnS_{0.77}$ and CdSe/$ZnS_{0.77}$-ReS_2 D) CdSe/$ZnS_{1.75}$ and CdSe/$ZnS_{1.75}$-ReS_2.

5.4.2 TA Spectra of Complexes on QDs

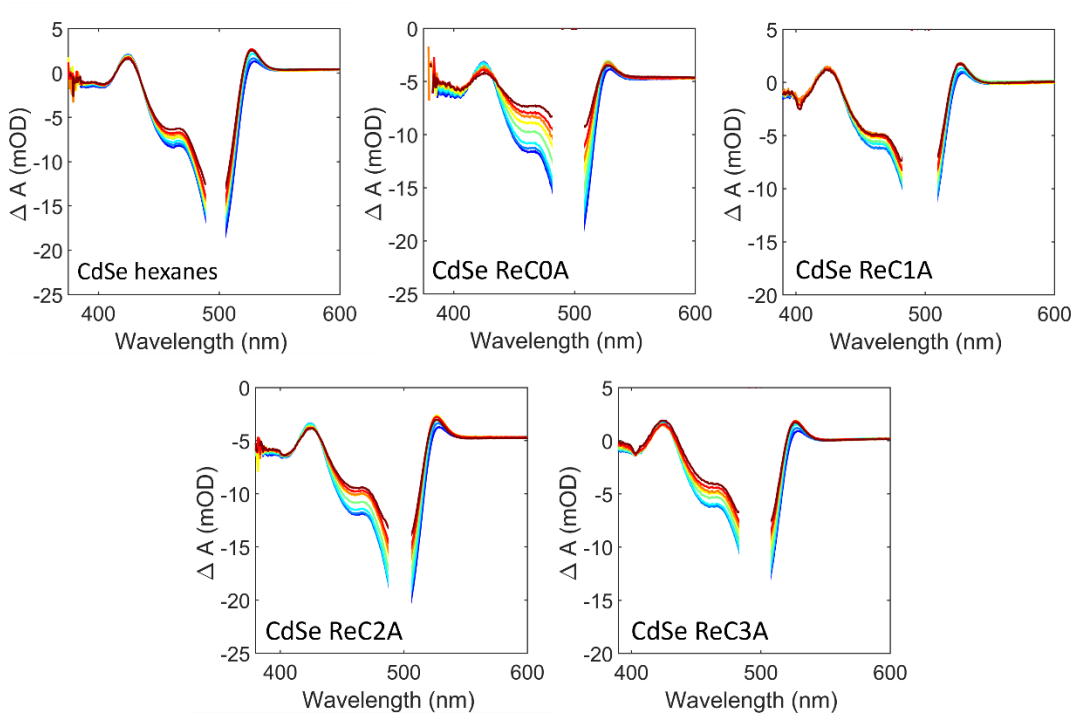

Figure S5.8. TA spectra of CdSe-ReCxA complexes. CdSe-ReC0A exhibits the fastest bleach recovery, with CdSe-ReC2A and ReC3A decaying slower, but faster than CdSe-ReC1A. (dark blue: 0-2 ps, blue: 2-5 ps, cyan: 5-15 ps, green: 25-100 ps, yellow: 100-200 ps, orange: 250-350 ps, red: 500-800 ps, burgundy: 1000-1600 ps)

Table S5.1. Parameters from multiexponential fits of the PL lifetime under 400 nm excitation

	IRF (ps)	**A_0**	**τ_0 (ns)**	**A_1**	**τ_1 (ns)**	**A_2**	**τ_2**
CdSe core	100	0.46 ± 0.02	2.30 ± 0.19	0.40 ± 0.015	17.5 ± 1.64	0.10 ± 0.19	147 ± 39.5
CdSe/$ZnS_{0.64}$	280	0.39 ±	4.97 ± 0.14	0.49 ±	26.3 ± 0.25	--	--

		0.006		0.006			
CdSe/ZnS$_{0.77}$	280	0.42 ± 0.009	6.44 ± 0.20	0.52 ± 0.01	27.4 ± 0.33	--	--
CdSe/ZnS1$_{1.75}$	280	0.41 ± 0.02	11.4 ± 0.48	0.51 ± 0.02	32.4 ± 0.64	--	--

The instrument response function (IRF) was obtained and fitted to a Gaussian to use in the PL lifetime fits.

Table S5.2. Amplitude weighted average time constants (ns) for CdSe-ReS_2 and CdSe/ZnS-ReS_2 complexes under 520 nm excitation.

	CdSe core	**CdSe/ZnS$_{0.64}$**	**CdSe/ZnS$_{0.77}$**	**CdSe/ZnS$_{1.75}$**
Without ReS_2	7.14 ± 0.052	7.62 ± 0.023	9.53 ± 0.027	16.2 ± 0.135
With ReS_2	6.94 ± 0.322	9.07 ± 0.006	9.30 ± 0.111	13.1 ± 0.296

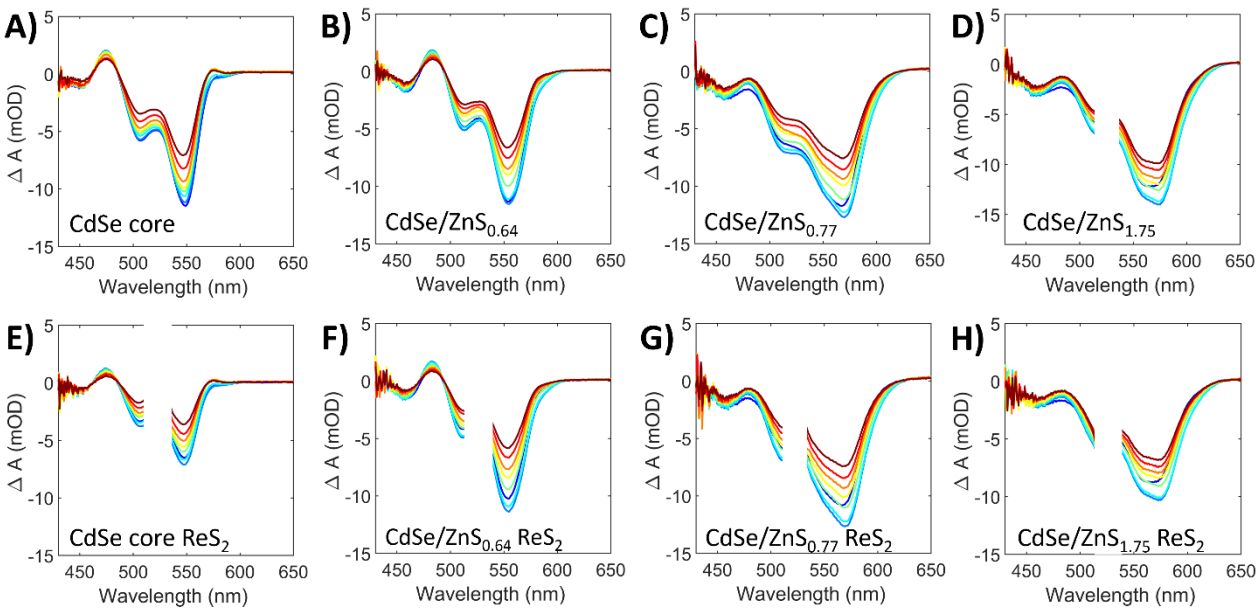

Figure S5.9. TA spectra of CdSe and CdSe/ZnS with and without ReS_2 bound. The lifetimes have been fit to triexponentials with lifetimes shown in the above table. The bleach recovery between each sample with and without ReS_2 seems fairly similar, confirmed by kinetics lifetimes. (dark blue: 0-2 ps, blue: 2-5 ps, cyan: 5-15 ps, green: 25-100 ps, yellow: 100-200 ps, orange: 250-350 ps, red: 500-800 ps, burgundy: 1000-1600 ps)

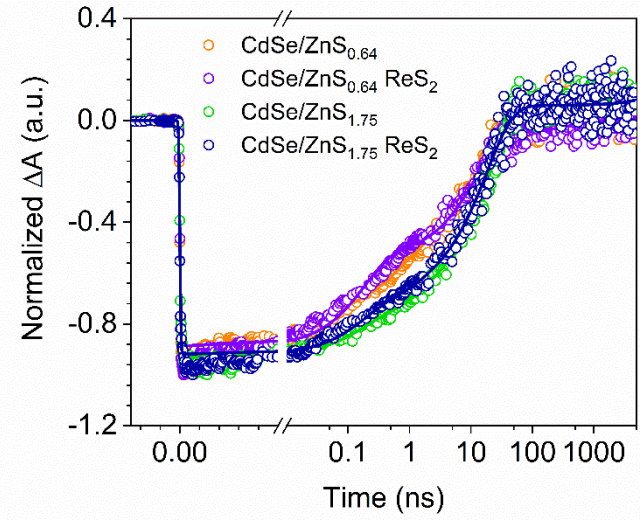

Figure S5.10. TA kinetics of the CdSe/$ZnS_{0.64}$, CdSe/$ZnS_{0.64}$-ReS_2, CdSe/$ZnS_{1.75}$, and CdSe/$ZnS_{1.75}$-ReS_2. Samples with ReS_2 show slightly faster kinetics, alluding to a small percentage of electron transfer.

5.4.3 Subtraction of solvent from TRIR Spectra: QD-ReCxA

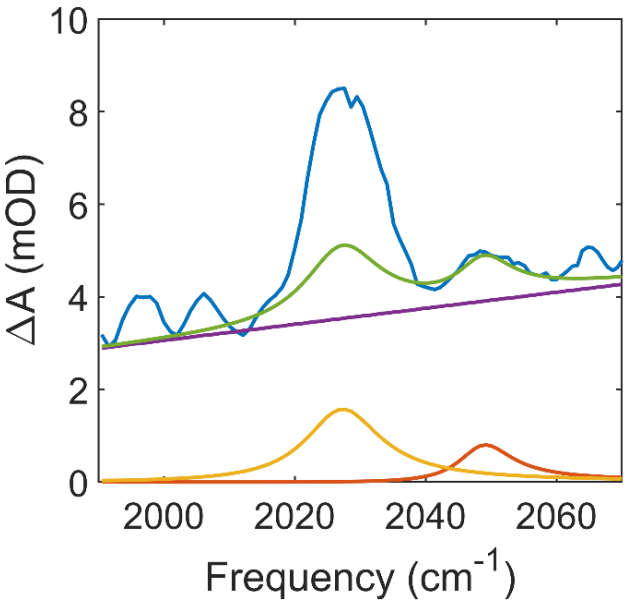

Parameters	Values from solvent fit
A_2	0.000013
q_2	7.79 **(fixed)**
v_{02}	2048.5 **(fixed)**
Γ_2	10 **(fixed)**
A_1 (A_2/3.4)	0.0000038
q_1	20.4 **(fixed)**
v_{01}	2027 **(fixed)**
Γ_1	14 **(fixed)**

Figure S5.11. Unsubtracted data demonstrating the method with which we eliminate the solvent absorption to obtain the ReCxA only FR signal. Blue: unsubtracted data, purple: polynomial fit of QD background, red: FR fit of solvent peak, yellow: FR fit of solvent under ReCxA FR to be subtracted, green: total fit of the solvent to be subtracted from the raw data.

Since the hexanes and CO FR coupling signals overlap, we have subtracted the hexanes to obtain the contribution only from the ReCxA FR. We fit the solvent FR to eq 1 to get the value of the Fano parameter, q, getting the ratio of the amplitudes between the peaks, and using those to fit the solvent peak at 2048 cm^{-1}, and therefore the amplitude of the solvent FR at 2028 cm^{-1} for subtraction. Explicitly, for each peak of the solvent, we fit two Lorentzian and two Fano terms, one for each peak. The Lorentzian amplitudes were held at some small value (0.001) due to negligible

contribution in comparison to the FR signal. After obtaining the fitting parameters (table in Figure S5.11), those values (q_i, ε_i, $\nu_{0,i}$, and Γ_i) from the solvent fit were held constant when fitting the CdSe-ReCxA samples. The amplitude ratio of the two solvent peaks was obtained (A_{2048}/A_{2048}) and that value was fixed when determining the amplitudes between the 2028 and 2048 cm^{-1} peaks for the ReCxA FR. For example, if the ratio between the solvent peaks was $A_{2048}/A_{2048} = 3.0$, we would then move to the CdSe-ReCxA samples. If we have the 0-1 ps trace of the CdSe-ReC0A sample and the amplitude of the 2048 cm^{-1} was 0.06, then the amplitude of the solvent under the ReCxA FR signal would be 0.02. We would then be able to subtract this curve from the raw spectrum (Figure S5.11) to obtain the ReCxA FR only contribution.

5.4.4. Fitted TRIR Spectra of CdSe and CdSe/ZnS on TiO_2 films

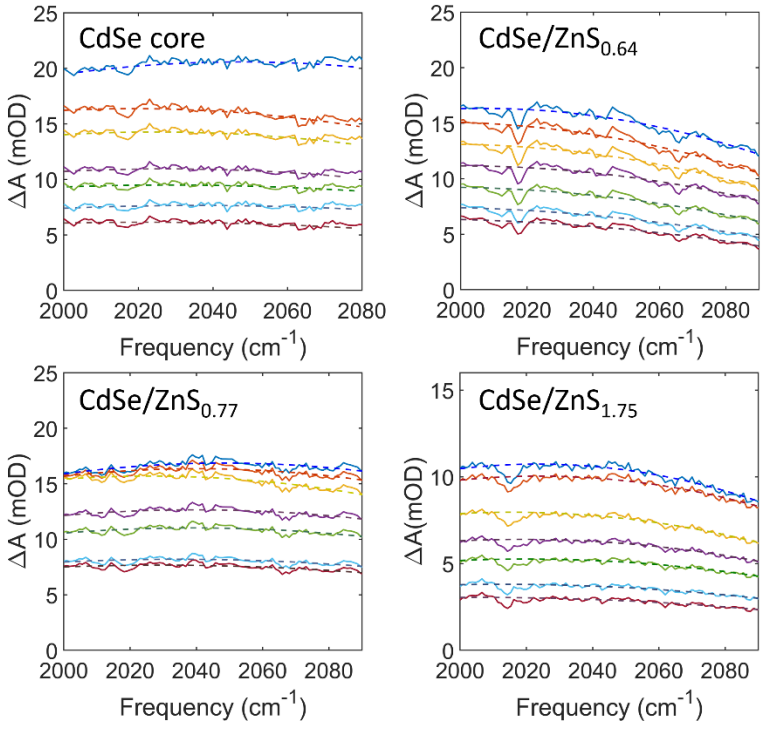

Figure S5.12. Fitted TA spectra of the QDs on TiO_2 films. Each spectrum is fit to a polynomial to describe the broad QD background originating from the 1S to 1P transition in the QD CB. (blue: 0-

1 ps, red: 2-5 ps, yellow: 5-15 ps, purple: 25-100 ps, green: 100-200 ps, light blue: 400-800 ps, burgundy: 800-1670 ps)

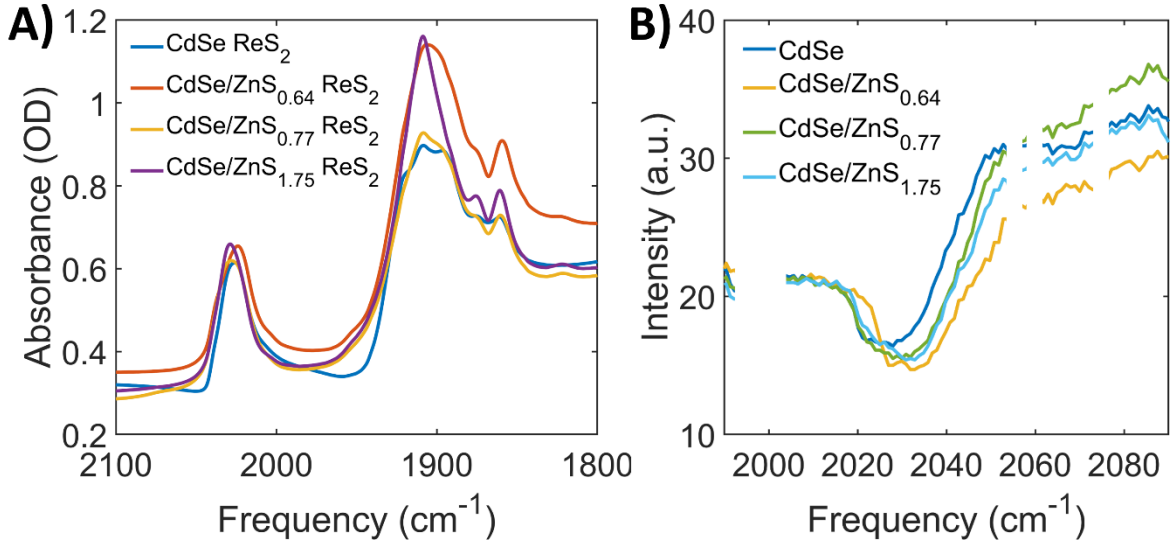

Figure S5.13. Infrared spectra of QD-ReS_2 films on TiO_2. A) FTIR of QD-ReS_2 films. The absorbance intensity of the catalyst was controlled so that they would be roughly the same. B) IR probe spectra of each film sample with ReS_2. Since the film samples are not uniform because we drop cast the samples, the ReS_2 signal was "calibrated" by moving the film to a spot where the probe absorption was similar.

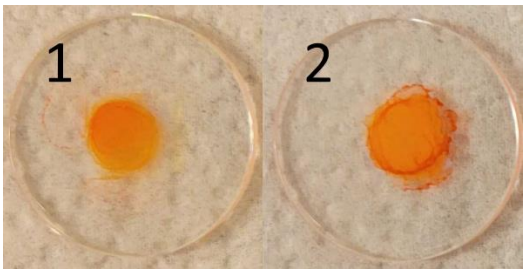

Figure S5.14. Representative pictures of QD-TiO_2 and QD-ReS_2-TiO_2 films. Samples are as follows: 1) CdSe core-TiO_2 2) CdSe core-ReS_2-TiO_2.

5.5 References

1. Wang, C., Chapter 9 - Quantum Dots for Visible-Light Photocatalytic CO2 Reduction. In *Novel Materials for Carbon Dioxide Mitigation Technology*, Shi, F.; Morreale, B., Eds. Elsevier: Amsterdam, 2015; pp 269-295.
2. Wu, K.; Lian, T., Quantum confined colloidal nanorod heterostructures for solar-to-fuel conversion. *Chemical Society Reviews* **2016,** *45* (14), 3781-3810.
3. Li, Q.; Zhao, F.; Qu, C.; Shang, Q.; Xu, Z.; Yu, L.; McBride, J. R.; Lian, T., Two-Dimensional Morphology Enhances Light-Driven H2 Generation Efficiency in CdS Nanoplatelet-Pt Heterostructures. *Journal of the American Chemical Society* **2018,** *140* (37), 11726-11734.
4. Song, W.; Qi, G.; Liu, B., Halide perovskite quantum dots for photocatalytic CO2 reduction. *Journal of Materials Chemistry A* **2023,** *11* (24), 12482-12498.
5. Kirmani, A. R.; Luther, J. M.; Abolhasani, M.; Amassian, A., Colloidal Quantum Dot Photovoltaics: Current Progress and Path to Gigawatt Scale Enabled by Smart Manufacturing. *ACS Energy Letters* **2020,** *5* (9), 3069-3100.
6. Kamat, P. V., Quantum Dot Solar Cells. The Next Big Thing in Photovoltaics. *The Journal of Physical Chemistry Letters* **2013,** *4* (6), 908-918.
7. Hu, L.; Zhao, Q.; Huang, S.; Zheng, J.; Guan, X.; Patterson, R.; Kim, J.; Shi, L.; Lin, C.-H.; Lei, Q.; Chu, D.; Tao, W.; Cheong, S.; Tilley, R. D.; Ho-Baillie, A. W. Y.; Luther, J. M.; Yuan, J.; Wu, T., Flexible and efficient perovskite quantum dot solar cells via hybrid interfacial architecture. *Nature Communications* **2021,** *12* (1), 466.
8. Kim, M. R.; Ma, D., Quantum-Dot-Based Solar Cells: Recent Advances, Strategies, and Challenges. *The Journal of Physical Chemistry Letters* **2015,** *6* (1), 85-99.
9. Chen, H.-C.; Shabir, A.; Tan, C. M.; Singh, P.; Lin, J.-H., Degradation dynamics of quantum dots in white LED applications. *Scientific Reports* **2021,** *11* (1), 24153.
10. Shirasaki, Y.; Supran, G. J.; Bawendi, M. G.; Bulović, V., Emergence of colloidal quantum-dot light-emitting technologies. *Nature Photonics* **2013,** *7* (1), 13-23.
11. Onal, A.; Eren, G. O.; Sadeghi, S.; Melikov, R.; Han, M.; Karatum, O.; Ozer, M. S.; Bahmani Jalali, H.; Dogru-Yuksel, I. B.; Yilgor, I.; Metin, Ö.; Nizamoglu, S., High-Performance White Light-Emitting Diodes over 150 lm/W Using Near-Unity-Emitting Quantum Dots in a Liquid Matrix. *ACS Photonics* **2022,** *9* (4), 1304-1314.
12. Bang, S. Y.; Suh, Y.-H.; Fan, X.-B.; Shin, D.-W.; Lee, S.; Choi, H. W.; Lee, T. H.; Yang, J.; Zhan, S.; Harden-Chaters, W.; Samarakoon, C.; Occhipinti, L. G.; Han, S. D.; Jung, S.-M.; Kim, J. M., Technology progress on quantum dot light-emitting diodes for next-generation displays. *Nanoscale Horizons* **2021,** *6* (2), 68-77.
13. Smith, A. M.; Nie, S., Semiconductor Nanocrystals: Structure, Properties, and Band Gap Engineering. *Accounts of Chemical Research* **2010,** *43* (2), 190-200.
14. Alivisatos, A. P., Semiconductor Clusters, Nanocrystals, and Quantum Dots. *Science* **1996,** *271* (5251), 933-937.
15. Jasieniak, J.; Califano, M.; Watkins, S. E., Size-Dependent Valence and Conduction Band-Edge Energies of Semiconductor Nanocrystals. *ACS Nano* **2011,** *5* (7), 5888-5902.
16. Peterson, M. D.; Cass, L. C.; Harris, R. D.; Edme, K.; Sung, K.; Weiss, E. A., The Role of Ligands in Determining the Exciton Relaxation Dynamics in Semiconductor Quantum Dots. *Annual Review of Physical Chemistry* **2014,** *65* (1), 317-339.
17. Katsiev, K.; Ip, A. H.; Fischer, A.; Tanabe, I.; Zhang, X.; Kirmani, A. R.; Voznyy, O.; Rollny, L. R.; Chou, K. W.; Thon, S. M.; Carey, G. H.; Cui, X.; Amassian, A.; Dowben, P.; Sargent, E. H.; Bakr,

O. M., The Complete In-Gap Electronic Structure of Colloidal Quantum Dot Solids and Its Correlation with Electronic Transport and Photovoltaic Performance. *Advanced Materials* **2014,** *26* (6), 937-942.
18. Kennehan, E. R.; Munson, K. T.; Grieco, C.; Doucette, G. S.; Marshall, A. R.; Beard, M. C.; Asbury, J. B., Exciton–Phonon Coupling and Carrier Relaxation in PbS Quantum Dots: The Case of Carboxylate Ligands. *The Journal of Physical Chemistry C* **2021,** *125* (41), 22622-22629.
19. Schnitzenbaumer, K. J.; Labrador, T.; Dukovic, G., Impact of Chalcogenide Ligands on Excited State Dynamics in CdSe Quantum Dots. *The Journal of Physical Chemistry C* **2015,** *119* (23), 13314-13324.
20. Hines, D. A.; Kamat, P. V., Recent Advances in Quantum Dot Surface Chemistry. *ACS Applied Materials & Interfaces* **2014,** *6* (5), 3041-3057.
21. Schnitzenbaumer, K. J.; Dukovic, G., Comparison of Phonon Damping Behavior in Quantum Dots Capped with Organic and Inorganic Ligands. *Nano Letters* **2018,** *18* (6), 3667-3674.
22. Leger, J. D.; Friedfeld, M. R.; Beck, R. A.; Gaynor, J. D.; Petrone, A.; Li, X.; Cossairt, B. M.; Khalil, M., Carboxylate Anchors Act as Exciton Reporters in 1.3 nm Indium Phosphide Nanoclusters. *The Journal of Physical Chemistry Letters* **2019,** *10* (8), 1833-1839.
23. Guyot-Sionnest, P.; Wehrenberg, B.; Yu, D., Intraband relaxation in CdSe nanocrystals and the strong influence of the surface ligands. *The Journal of Chemical Physics* **2005,** *123* (7), 074709.
24. Mack, T. G.; Jethi, L.; Andrews, M.; Kambhampati, P., Direct Observation of Vibronic Coupling between Excitonic States of CdSe Nanocrystals and Their Passivating Ligands. *The Journal of Physical Chemistry C* **2019,** *123* (8), 5084-5091.
25. Kennehan, E. R.; Munson, K. T.; Doucette, G. S.; Marshall, A. R.; Beard, M. C.; Asbury, J. B., Dynamic Ligand Surface Chemistry of Excited PbS Quantum Dots. *The Journal of Physical Chemistry Letters* **2020,** *11* (6), 2291-2297.
26. Kennehan, E. R.; Munson, K. T.; Grieco, C.; Doucette, G. S.; Marshall, A. R.; Beard, M. C.; Asbury, J. B., Influence of Ligand Structure on Excited State Surface Chemistry of Lead Sulfide Quantum Dots. *Journal of the American Chemical Society* **2021,** *143* (34), 13824-13834.
27. Limonov, M. F.; Rybin, M. V.; Poddubny, A. N.; Kivshar, Y. S., Fano resonances in photonics. *Nature Photonics* **2017,** *11* (9), 543-554.
28. Miroshnichenko, A. E.; Flach, S.; Kivshar, Y. S., Fano resonances in nanoscale structures. *Reviews of Modern Physics* **2010,** *82* (3), 2257-2298.
29. Luk'yanchuk, B.; Zheludev, N. I.; Maier, S. A.; Halas, N. J.; Nordlander, P.; Giessen, H.; Chong, C. T., The Fano resonance in plasmonic nanostructures and metamaterials. *Nature Materials* **2010,** *9* (9), 707-715.
30. Mirin, N. A.; Bao, K.; Nordlander, P., Fano Resonances in Plasmonic Nanoparticle Aggregates. *The Journal of Physical Chemistry A* **2009,** *113* (16), 4028-4034.
31. Khanikaev, A. B.; Wu, C.; Shvets, G., Fano-resonant metamaterials and their applications. *Nanophotonics* **2013,** *2* (4), 247-264.
32. Verellen, N.; Sonnefraud, Y.; Sobhani, H.; Hao, F.; Moshchalkov, V. V.; Dorpe, P. V.; Nordlander, P.; Maier, S. A., Fano Resonances in Individual Coherent Plasmonic Nanocavities. *Nano Letters* **2009,** *9* (4), 1663-1667.
33. Rahmani, M.; Luk'yanchuk, B.; Hong, M., Fano resonance in novel plasmonic nanostructures. *Laser & Photonics Reviews* **2013,** *7* (3), 329-349.
34. Frontiera, R. R.; Gruenke, N. L.; Van Duyne, R. P., Fano-Like Resonances Arising from Long-Lived Molecule-Plasmon Interactions in Colloidal Nanoantennas. *Nano Letters* **2012,** *12* (11), 5989-5994.
35. Asbury, J. B.; Hao, E.; Wang, Y.; Lian, T., Bridge Length-Dependent Ultrafast Electron Transfer from Re Polypyridyl Complexes to Nanocrystalline TiO2 Thin Films Studied by Femtosecond Infrared Spectroscopy. *The Journal of Physical Chemistry B* **2000,** *104* (50), 11957-11964.

36. Anfuso, C. L.; Xiao, D.; Ricks, A. M.; Negre, C. F. A.; Batista, V. S.; Lian, T., Orientation of a Series of CO2 Reduction Catalysts on Single Crystal TiO2 Probed by Phase-Sensitive Vibrational Sum Frequency Generation Spectroscopy (PS-VSFG). *The Journal of Physical Chemistry C* **2012,** *116* (45), 24107-24114.
37. Takeda, H.; Koike, K.; Morimoto, T.; Inumaru, H.; Ishitani, O., Photochemistry and photocatalysis of rhenium(I) diimine complexes. In *Advances in Inorganic Chemistry*, Eldik, R. v.; Stochel, G., Eds. Academic Press: 2011; Vol. 63, pp 137-186.
38. Reiss, P.; Protière, M.; Li, L., Core/Shell Semiconductor Nanocrystals. *Small* **2009,** *5* (2), 154-168.
39. Zhu, H.; Song, N.; Lian, T., Controlling Charge Separation and Recombination Rates in CdSe/ZnS Type I Core−Shell Quantum Dots by Shell Thicknesses. *Journal of the American Chemical Society* **2010,** *132* (42), 15038-15045.
40. Cattaneo, M.; Guo, F.; Kelly, H. R.; Videla, P. E.; Kiefer, L.; Gebre, S.; Ge, A.; Liu, Q.; Wu, S.; Lian, T.; Batista, V. S., Robust Binding of Disulfide-Substituted Rhenium Bipyridyl Complexes for CO2 Reduction on Gold Electrodes. *Frontiers in Chemistry* **2020,** *8*.
41. Zhu, H.; Yang, Y.; Wu, K.; Lian, T., Charge Transfer Dynamics from Photoexcited Semiconductor Quantum Dots. *Annual Review of Physical Chemistry* **2016,** *67* (1), 259-281.
42. Yang, W.; Liu, Y.; Edvinsson, T.; Castner, A.; Wang, S.; He, S.; Ott, S.; Hammarström, L.; Lian, T., Photoinduced Fano Resonances between Quantum Confined Nanocrystals and Adsorbed Molecular Catalysts. *Nano Letters* **2021,** *21* (13), 5813-5818.
43. Wu, K.; Liu, Z.; Zhu, H.; Lian, T., Exciton Annihilation and Dissociation Dynamics in Group II–V Cd3P2 Quantum Dots. *The Journal of Physical Chemistry A* **2013,** *117* (29), 6362-6372.

Chapter 6. Epitaxial Growth of Highly Symmetrical Branched Noble Metal-Semiconductor Heterostructures with Efficient Plasmon-Induced Hot-Electron Transfer

With Yawei Liu

This chapter was partially reproduced from Zhai, L., Gebre, S.T., Chen, B. *et al.* Epitaxial growth of highly symmetrical branched noble metal-semiconductor heterostructures with efficient plasmon-induced hot-electron transfer. *Nat Commun* **14**, 2538 (2023)

6.1 Introduction

Plasmonic nanomaterials have been studied for application in photovoltaics[1-2], photodetection[3-4], and photocatalysis[2, 5-6] owing to their localized surface plasmon resonances (LSPR) and large absorption cross sections.[5] Oftentimes, they are used with semiconductors to form heterostructures across which an electron can be injected upon excitation of the plasmonic material. The most common heterostructures include metal nanoparticles (NP) such as Au or Ag with semiconductor materials like metal oxides or chalcogenides.[7-10] The type of plasmonic material, its size and morphology, as well as the metal semiconductor interface are all factors that can affect the efficiency of charge transfer within these materials, which would affect their potential for application in devices.[11-12] For example, Zhang *et al.* has used theory to demonstrate that different shapes results in different amounts of charge carriers where they determined that nanocubes can generate a higher amount of charge carriers than nanospheres, which has more photogenerated carriers than a Au slab.[11]

Epitaxial synthesis has become one of the most common ways of precisely controlling the structure and interface of the heterostructure.[13-14] However, this method requires a small lattice mismatch[13, 15-16] and many of the materials synthesized epitaxially are made up of similar

components, e.g. metal oxide- metal oxide[17-18] and perovskite-perovskite[19]. While nonepitaxial noble metal- semiconductor heterostructures have demonstrated potential usefulness in photovoltaics[2, 9, 20] and other applications, these materials are limited in their ability to control the structure and interface. Here we have synthesized Ag-CdSe and Ag-CdS epitaxial heterostructures with well-defined interfaces with a lattice mismatch of 40% and demonstrated their superior plasmon induced hot electron transfer (PHET) quantum yield (QY) with values of 17.6% and 18.1%, respectively.

6.2 Experimental Methods

Time resolved infrared and transient absorption spectroscopies were used as described in Chapter 2.1.

6.2.1 Quantum Yield Calculation

The QY of electron transfer from Ag to CdS and CdSe (550 and 700 nm excitation, respectively) was determined using the method described by Wu *et al.*[7] It can be determined by using the amplitude of the IR absorption originating from the 1S to 1P transition in the CdS (CdSe) per CB electron (Eq 1), which can be observed with kinetics traced around 3340 cm^{-1}.

$$S_0 = \frac{\Delta A\ (CdS, 400\ nm)}{N\ (CdS\ CB\ electrons)} \quad (1)$$

ΔA denotes the maximum signal amplitude from the kinetics, while N corresponds to the number of CdS CB electrons determined by the number of absorbed photons by CdS under 400 nm excitation. One photon creates one CB electron with CdS pumped at 400 nm, therefore N is the photon flux in the pump-probe overlap region multiplied by the sample absorption: $(\frac{power/_{hv}}{beam\ size}\ x\ (1 - 10^{OD}))$, where hv is the photon energy.

In Eq 2, the QY can be calculated by determining the number of hot electrons formed in

Ag-CdS per the number of absorbed photons after 550 nm pump excitation:

$$QY = \frac{N\ (hot\ electrons)}{N\ (absorbed\ photons)} \tag{2}$$

$$= \frac{\frac{\Delta A\ (Ag-CdS,550)}{S_0}}{\frac{power\ (550)}{hv\ (550)}\ x\ (1-10^{-OD(Ag-CdS,550)})}$$

$$= \frac{beam\ size\ (550)}{beam\ size\ (400)}\ x\ \left[\frac{\frac{\Delta A\ (Ag-CdS,550)}{power\ (550)/hv\ (550)}}{(1-10^{-OD(Ag-CdS,550)})} \Big/ \frac{\frac{\Delta A\ (CdS,400)}{power\ (400)/hv\ (400)}}{(1-10^{-OD(CdS,400)})}\right]$$

where beam size (550) and beam size (400) are the pump probe overlap areas under both pump excitations. The ratio of these can be determined by using Cd_3P_2 as a calibration sample under the same conditions excited at both wavelengths, which we expect to have the same QY for creating CB electrons. Therefore, $\frac{beam\ size\ (550)}{beam\ size\ (400)}$ can be described below as

$$\frac{beam\ size\ (550)}{beam\ size\ (400)} = \frac{\frac{\Delta A\ (Cd_3P_2,400)}{power\ (400)/hv\ (400)}}{(1-10^{-OD(Cd_3P_2,400)})} \Big/ \frac{\frac{\Delta A\ (Cd_3P_2,550)}{power\ (550)/hv\ (550)}}{(1-10^{-OD(Cd_3P_2,550)})} \tag{3}$$

The plasmon induced hot electron QY in Ag-CdS icosapods can therefore be described as:

$$QY = \frac{\frac{\Delta S\ (Ag-CdS,550)}{1-10^{-OD\ (Ag-CdS,550)}}}{\frac{\Delta S\ (CdS,400)}{1-10^{-OD\ (CdS,400)}}}\ x\ \frac{\frac{\Delta S\ (Cd_3P_2,400)}{1-10^{-OD\ (Cd_3P_2,400)}}}{\frac{\Delta S\ (Cd_3P_2,550)}{1-10^{-OD\ (Cd_3P_2,550)}}} \tag{4}$$

where $\Delta S = \frac{\Delta A}{power}$, which can be obtained from the IR experiment. To ensure the linearity of ΔS, ΔA as a function of power was measured for each sample before the experiment, which can be seen in Figures 6.5. After linearly fitting the power dependence, the value of the slope was used for ΔS. All sample absorbances were between 0.2 and 0.8 OD. Since separately synthesized CdS NRs were used as controls and will be slightly different than the icosapods, we calculated the QY to the best of our ability.

The QY for Ag-CdSe icosapods were calculated the same way as shown below:

$$QY = \frac{\frac{\Delta S\,(Ag-CdSe,700)}{1-10^{-OD\,(Ag-CdSe,700)}}}{\frac{\Delta S\,(CdSe,400)}{1-10^{-OD\,(CdSe,400)}}} \; x \; \frac{\frac{\Delta S\,(Cd_3P_2,400)}{1-10^{-OD\,(Cd_3P_2,400)}}}{\frac{\Delta S\,(Cd_3P_2,700)}{1-10^{-OD\,(Cd_3P_2,700)}}} \tag{5}$$

Instead of 550 nm pump, 700 nm excitation was used, and the IR kinetics were traced at 3340 cm^{-1}, as before.

6.2.2 Multiexponential Fitting for PHET and Charge Recombination

The transient kinetics were fit to the following equation:

$$S(t) = IRF \otimes \left[-exp\left(-\frac{t}{T_f}\right) + \sum_1^3 A_i exp\left(-\frac{t}{T_i}\right)\right] \tag{6}$$

The instrument response function (IRF) used was determined by using a 1 mm silicon wafer under the same experimental conditions. The kinetics were well described by a Gaussian function where the FWHM was determined to be 177 ± 25 fs. T_f is the rising time constant while A_i and T_i ($i = 1, 2, 3$) are the amplitude and time constants for the multiexponential decay function (charge recombination), respectively. Since the kinetics are normalized, we hold the sum of the amplitudes to be 1.

6.3 Results and Discussion: Ultrafast Plasmon Induced Hot Electron Transfer

Both Ag-CdS and Ag-CdSe icosapods were synthesized with epitaxial interfaces and well-defined structures. High angle annular dark field scanning transmission electron microscopy (HAADF-STEM) was performed to obtain high resolution images of the icosapods and demonstrates the branched structure of the CdS NRs bound to a single Ag NP center (Figure 6.1).

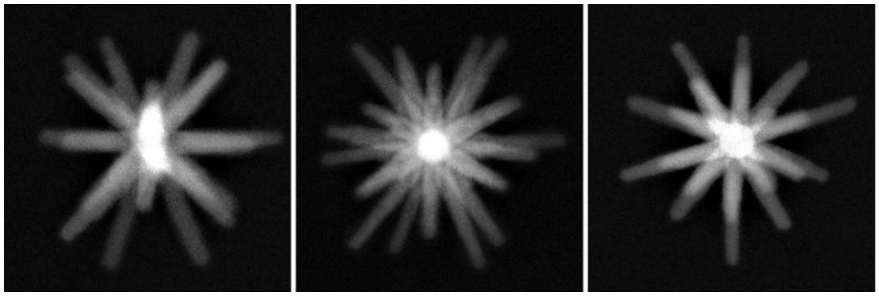

Figure 6.1. HAADF-STEM images of Ag-CdS icosapods taken by Zhai Li at Hong Kong City University. The icosapods are viewed from the C_2 (left), C_3 (middle), and C_5 (right) axes.

To understand the optical properties of these heterostructures, transient absorption and time resolved infrared spectroscopy were performed. The Ag LSPR band located at 548 nm, is offset from its SC counterparts. The CdSe and CdS 1S exciton bands are located at 462 and ~630 nm, respectively (Figure 6.2). The Ag plasmon band was selectively excited for both samples and probed with white light and mid-IR centered around 3340 cm^{-1}; Ag-CdS under 550 nm excitation, and Ag-CdSe pumped at 700 nm.

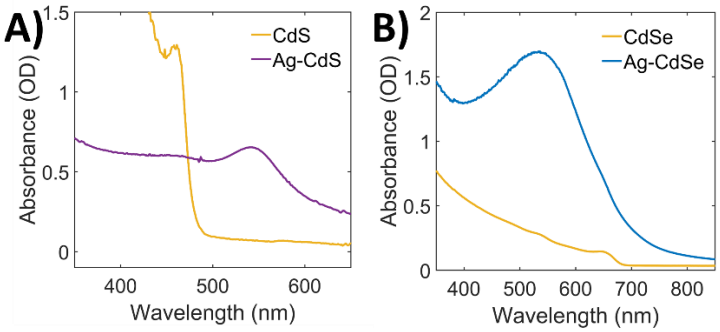

Figure 6.2. UV-Vis spectra of CdS (CdSe) NRs and Ag-CdS (CdSe) icosapods. A) CdS absorbance is centered at 462 nm in both samples while the Ag LSPR band is centered around 540 nm. B) CdSe absorbance is centered at 650 nm and Ag LSPR is once again centered around 540 nm.

In the TA, two bleaches are observed centered at ~480 and ~550 nm which can be attributed to bleaches of the Ag LSPR band and state filling in the CdS CB (Figure 6.3). Since the CdS is not excited we can attribute the CdS bleach to electron transfer from the Ag. The same is true for Ag-CdSe, with bleaches centered at ~530 and 650 nm.

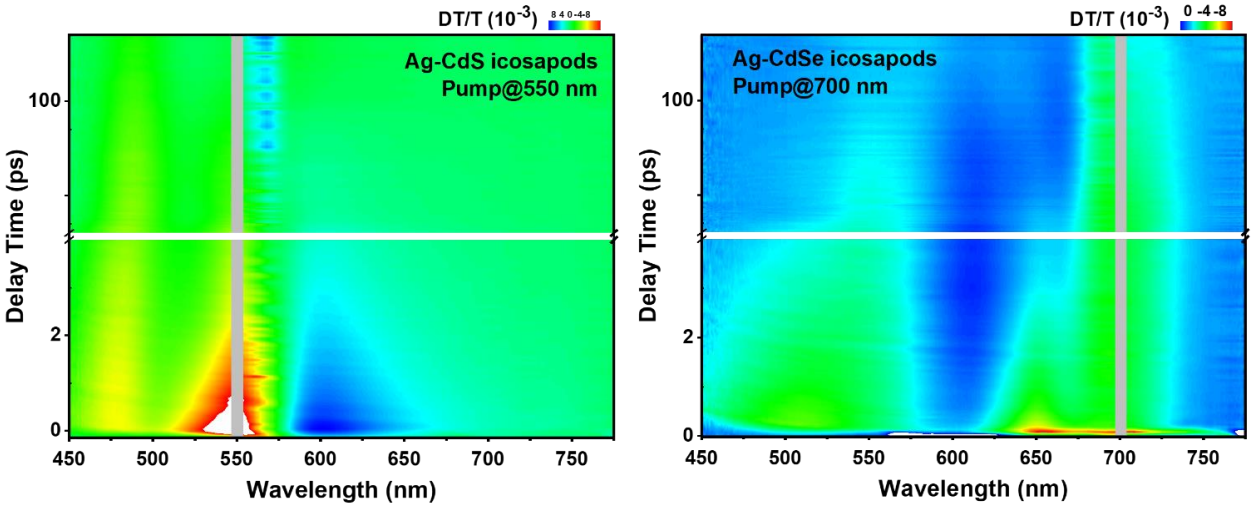

Figure 6.3. TA color spectra of Ag-CdS (left) and Ag-CdSe (right). Spectra show bleaching of both the Ag LSPR band and CdS (CdSe) exciton bands. Since neither SC is excited, the bleaching is due to electron transfer from the Ag.

For TRIR, we first investigate Ag-CdS. After excitation, the plasmon decays into an electron hole pair, after which the electron is injected into the semiconductor material through either PHET or indirect interfacial charge transfer. In the mid-IR spectra, upon electron transfer to CdS, a broad absorption is observed corresponding to the 1S to 1P transition in the conduction band (CB) confirming the electron transfer process (Figure 6.4a and b). By fitting the rising time and subsequent decay of the kinetics, we obtain a PHET time of approximately 18.0 ± 0.3 fs with a recombination time of 1.9 ± 0.16 ps.

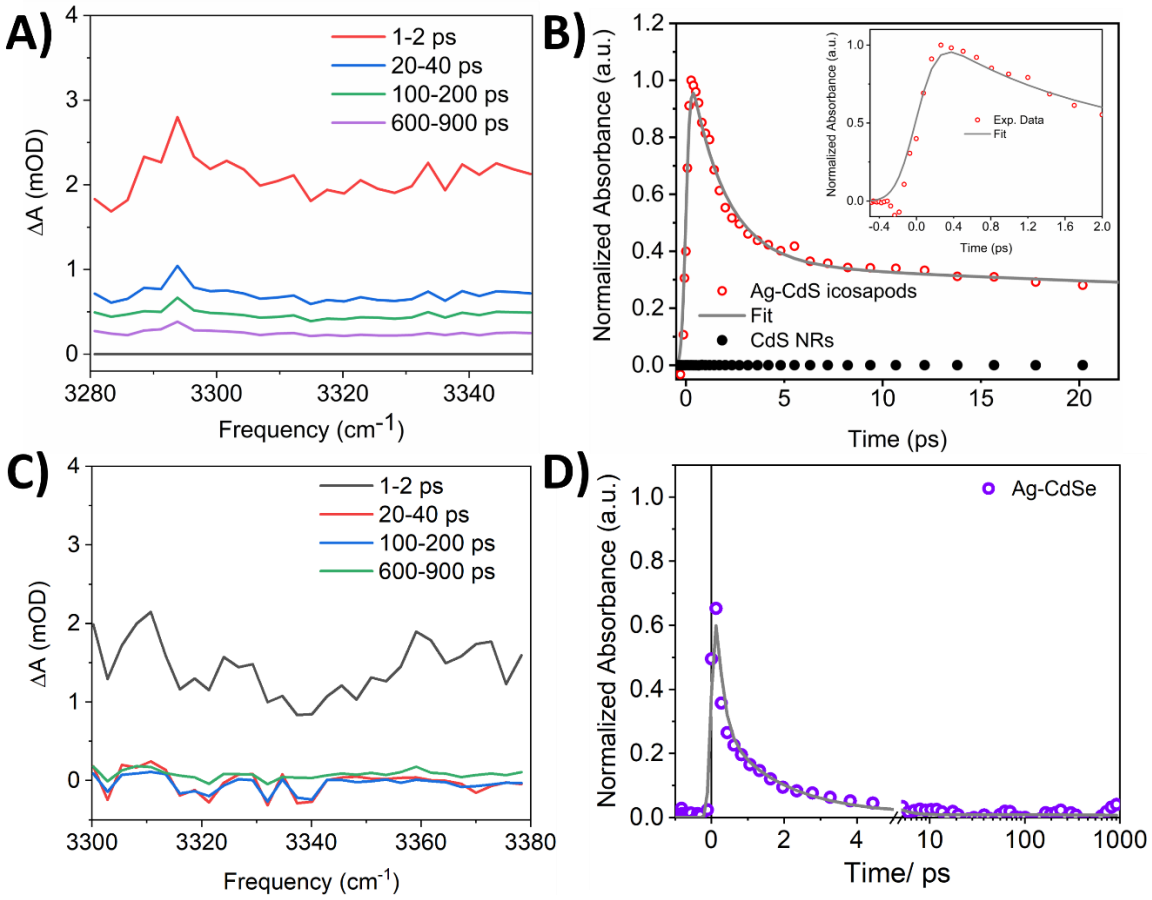

Figure 6.4. Time resolved IR data of Ag-CdS icosapods. A) TRIR spectra shows an absorption corresponding to the 1S to 1P transition within the CdSe CB band, indicating electron transfer. B) Normalized kinetics traced at ~3340 cm^{-1} with zoomed in kinetics (inset). The fast rising time indicates electron transfer to CdS (CdSe) while subsequent decay corresponds to recombination. C) TRIR spectra of Ag-CdSe. D) Normalized and fitted kinetics traced at ~3340 cm^{-1}.

We can also quantify the quantum yield using the initial amplitude of the IR absorption after excitation according to the experimental methods. We performed a power dependence study to ensure the maximum signal amplitude at different powers was linear, for the QY calculation (Figure 6.5). We find that the electron injection for Ag-CdS has a quantum yield of 18.1%, much higher than QY observed in nonepitaxial heterostructures.[21-23] A similarly high QY was observed for Ag-CdSe

under 700 nm excitation (Figure 6.4c and d), outside the CdSe exciton absorbance. Using the same method, a QY of 17.6% was obtained along with a charge transfer time of 7.5 ± 7.2 fs and a recombination time of 0.2 ± 0.1 ps.

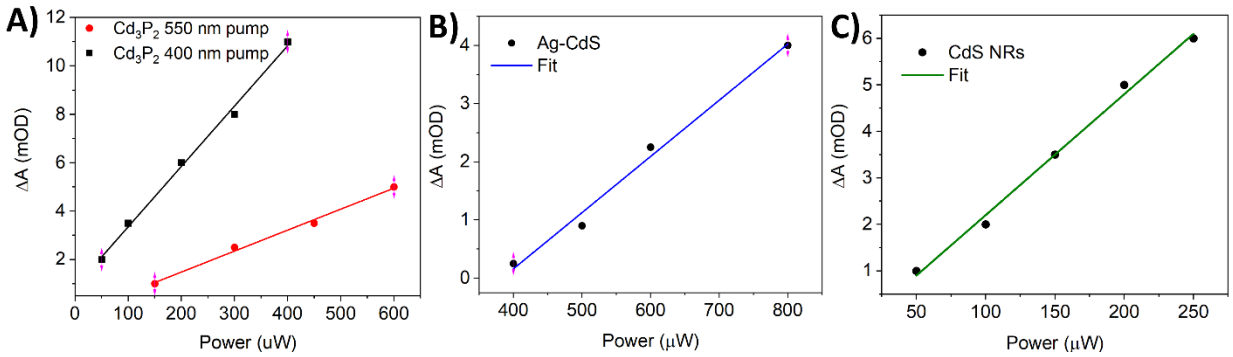

Figure 6.5. Linear fits of the maximum absorptions of samples for QY calculation. A) Cd_3P_2 B) Ag-CdS icosapods C) CdS NRs.

Based on the PHET transfer time constants, we can determine that the electron is directly injected into the SC (< 20 fs) and not indirectly, which commonly occurs on timescale of more than 100 fs (Figure 6.6). Unfortunately, we were not able to provide direct information on the effect of the metal-SC interfacial states on PHET and recombination processes because time resolved IR can only probe the electron after injection into the CdS CB.

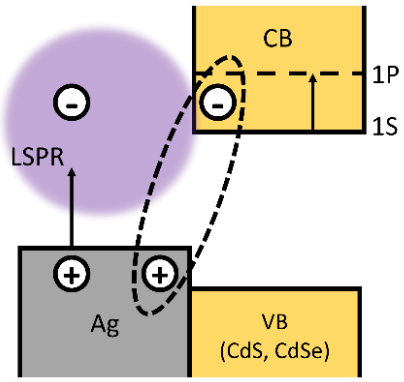

Figure 6.6. Schematic of plasmon induced hot electron transfer mechanism in Ag-CdS and Ag-CdSe icosapods.

6.4 Conclusions

In conclusion, we have achieved high QYs for electron injection in epitaxial Ag-CdSe and Ag-CdS heterostructures with fast electron injection lifetimes. We have demonstrated that epitaxial interfaces can enhance the QY and electron transfer in comparison to typical nonepitaxial heterostructure interfaces observed in literature. This presents an interesting new method of heterostructure synthesis for increasing the efficiency of PHET towards use in applications.

6.5 References

1. Atwater, H. A.; Polman, A., Plasmonics for improved photovoltaic devices. *Nature Materials* **2010,** *9* (3), 205-213.
2. Clavero, C., Plasmon-induced hot-electron generation at nanoparticle/metal-oxide interfaces for photovoltaic and photocatalytic devices. *Nature Photonics* **2014,** *8* (2), 95-103.
3. Knight, M. W.; Sobhani, H.; Nordlander, P.; Halas, N. J., Photodetection with Active Optical Antennas. *Science* **2011,** *332* (6030), 702-704.
4. and, S. L.; El-Sayed, M. A., Optical Properties and Ultrafast Dynamics of Metallic Nanocrystals. *Annual Review of Physical Chemistry* **2003,** *54* (1), 331-366.
5. Brongersma, M. L.; Halas, N. J.; Nordlander, P., Plasmon-induced hot carrier science and technology. *Nature Nanotechnology* **2015,** *10* (1), 25-34.
6. Zhang, Y.; He, S.; Guo, W.; Hu, Y.; Huang, J.; Mulcahy, J. R.; Wei, W. D., Surface-Plasmon-Driven Hot Electron Photochemistry. *Chemical Reviews* **2018,** *118* (6), 2927-2954.
7. Wu, K.; Chen, J.; McBride, J. R.; Lian, T., Efficient hot-electron transfer by a plasmon-induced interfacial charge-transfer transition. *Science* **2015,** *349* (6248), 632-635.
8. Nishijima, Y.; Ueno, K.; Yokota, Y.; Murakoshi, K.; Misawa, H., Plasmon-Assisted Photocurrent Generation from Visible to Near-Infrared Wavelength Using a Au-Nanorods/TiO2 Electrode. *The Journal of Physical Chemistry Letters* **2010,** *1* (13), 2031-2036.
9. Linic, S.; Chavez, S.; Elias, R., Flow and extraction of energy and charge carriers in hybrid plasmonic nanostructures. *Nature Materials* **2021,** *20* (7), 916-924.
10. Wolff, C. M.; Frischmann, P. D.; Schulze, M.; Bohn, B. J.; Wein, R.; Livadas, P.; Carlson, M. T.; Jäckel, F.; Feldmann, J.; Würthner, F.; Stolarczyk, J. K., All-in-one visible-light-driven water splitting by combining nanoparticulate and molecular co-catalysts on CdS nanorods. *Nature Energy* **2018,** *3* (10), 862-869.
11. Zhang, H.; Govorov, A. O., Optical Generation of Hot Plasmonic Carriers in Metal Nanocrystals: The Effects of Shape and Field Enhancement. *The Journal of Physical Chemistry C* **2014,** *118* (14), 7606-7614.
12. Brown, A. M.; Sundararaman, R.; Narang, P.; Goddard, W. A., III; Atwater, H. A., Nonradiative Plasmon Decay and Hot Carrier Dynamics: Effects of Phonons, Surfaces, and Geometry. *ACS Nano* **2016,** *10* (1), 957-966.
13. Tan, C.; Chen, J.; Wu, X.-J.; Zhang, H., Epitaxial growth of hybrid nanostructures. *Nature Reviews Materials* **2018,** *3* (2), 17089.
14. Habas, S. E.; Lee, H.; Radmilovic, V.; Somorjai, G. A.; Yang, P., Shaping binary metal nanocrystals through epitaxial seeded growth. *Nature Materials* **2007,** *6* (9), 692-697.
15. Kelso, M. V.; Mahenderkar, N. K.; Chen, Q.; Tubbesing, J. Z.; Switzer, J. A., Spin coating epitaxial films. *Science* **2019,** *364* (6436), 166-169.
16. Grundmann, M., Formation of epitaxial domains: Unified theory and survey of experimental results. *physica status solidi (b)* **2011,** *248* (4), 805-824.
17. Oh, M. H.; Cho, M. G.; Chung, D. Y.; Park, I.; Kwon, Y. P.; Ophus, C.; Kim, D.; Kim, M. G.; Jeong, B.; Gu, X. W.; Jo, J.; Yoo, J. M.; Hong, J.; McMains, S.; Kang, K.; Sung, Y.-E.; Alivisatos, A. P.; Hyeon, T., Design and synthesis of multigrain nanocrystals via geometric misfit strain. *Nature* **2020,** *577* (7790), 359-363.
18. Forticaux, A.; Hacialioglu, S.; DeGrave, J. P.; Dziedzic, R.; Jin, S., Three-Dimensional Mesoscale Heterostructures of ZnO Nanowire Arrays Epitaxially Grown on CuGaO2 Nanoplates as Individual Diodes. *ACS Nano* **2013,** *7* (9), 8224-8232.

19. Shi, E.; Yuan, B.; Shiring, S. B.; Gao, Y.; Akriti; Guo, Y.; Su, C.; Lai, M.; Yang, P.; Kong, J.; Savoie, B. M.; Yu, Y.; Dou, L., Two-dimensional halide perovskite lateral epitaxial heterostructures. *Nature* **2020,** *580* (7805), 614-620.
20. Jang, Y. H.; Jang, Y. J.; Kim, S.; Quan, L. N.; Chung, K.; Kim, D. H., Plasmonic Solar Cells: From Rational Design to Mechanism Overview. *Chemical Reviews* **2016,** *116* (24), 14982-15034.
21. Wu, K.; Rodríguez-Córdoba, W. E.; Yang, Y.; Lian, T., Plasmon-Induced Hot Electron Transfer from the Au Tip to CdS Rod in CdS-Au Nanoheterostructures. *Nano Letters* **2013,** *13* (11), 5255-5263.
22. Ratchford, D. C., Plasmon-Induced Charge Transfer: Challenges and Outlook. *ACS Nano* **2019,** *13* (12), 13610-13614.
23. Tagliabue, G.; DuChene, J. S.; Abdellah, M.; Habib, A.; Gosztola, D. J.; Hattori, Y.; Cheng, W.-H.; Zheng, K.; Canton, S. E.; Sundararaman, R.; Sá, J.; Atwater, H. A., Ultrafast hot-hole injection modifies hot-electron dynamics in Au/p-GaN heterostructures. *Nature Materials* **2020,** *19* (12), 1312-1318.

Chapter 7. Summary

In conclusion, both QDs and plasmonic SC heterostructures are useful for photocatalysis, photovoltaics, and photodetection. A crucial aspect of these materials' performance in these devices is their surface chemistry and interfacial structure. In QDs, control over surface structure and size can affect the ability to generate charge carriers and their lifetime while the size, shape, and interfacial structure of plasmonics and plasmonic-SC heterostructures affects the character of the LSPR band and the amount of generated charge carriers. Therefore, understanding the effects of surface and interfacial structure has become an important area of study for both types of materials.

In this dissertation, we have discussed the effect of surface bound species and interfacial structure on charge transfer as well as coupling that can occur between QDs and molecular catalyst complexes. In Chapter 3, we studied electron transfer between Cd_3P_2 and ReC0A with and without triethylamine (TEA), a hole scavenger necessary for performing CO_2 reduction with this system. We found that with TEA, electron transfer was ~4 times faster than without it due to the electron donating properties of TEA (L-type ligand). We can explain this phenomenon with three possibilities: (1) TEA can bind to the Cd_3P_2 surface and donate its electron density, (2) TEA can deprotonate the surface of Cd_3P_2, or (3) TEA can preferentially solvate the QD. Each of these would result in the Cd_3P_2 conduction band edge shifting to more negative potentials, making electron transfer to ReC0A more favorable. This trend was also evident in other QD-electron acceptor complexes, making this an interesting discovery as such hole scavengers are used throughout QD studies and suggests these molecules may have a secondary role beyond their typical use. In the next two chapters, we investigate Fano resonance coupling in CdSe-Re catalyst complexes under different experimental conditions. In Chapter 4, we vary the catalyst concentration and QD size and find that the Fano coupling increases with increasing ReC0A on the surface and

decreases with QD size. The concentration dependence is due to an increase in the overall oscillator strength of the catalyst complex resulting in a stronger interaction with the CdSe CB electron. As for the QD size trend, it is well known that the amplitude of the QD wavefunction and radial distribution of the electron decreases with increasing size. This implies that the wavefunction dissipates with increasing size, decreasing the overlap between the wavefunction and vibrational oscillator. Based on calculations performed by our collaborator's group (Ribiero), the Fano coupling is mainly due to a charge transfer interaction that leads to stronger transition dipoles. However, this is expected to decrease as the size increases, due to what is previously described. In Chapter 5, we further investigate Fano resonance coupling as a function of distance using various Re catalysts with different linker lengths (ReCxA) and varying the shell thickness of CdSe/ZnS core shell structures. We found that ReC2A and ReC3A had larger or similar coupling values as ReC0A, most likely due to the possibility of those complexes being able to bend in such a way that the CO modes would be closer to the surface than in the ReC1A case. In addition, with increasing ZnS shell thicknesses we found the coupling decreased due to the electron wavefunction being confined to the CdSe core and not being able to penetrate through the ZnS surface, decreasing the overlap with the ReS_2 vibrational CO modes. Once again, coupling occurs because of a charge transfer interaction, in which case the IR oscillator strength of the catalyst molecules would decrease with increasing distance. In the last chapter, we discuss the plasmon induced hot electron transfer in Ag-CdS and Ag-CdSe epitaxial heterostructures synthesized by our collaborators at Hong Kong City University. After selective excitation of the Ag LSPR band, we observed electron transfer in visible TA spectra and were able to observe the growth of an infrared signal corresponding to the CdS (CdSe) 1S to 1P CB transition. We were able to calculate the QY and charge transfer from Ag to the SCs and found a QY of 18.1% for Ag-CdS and 17.6% for Ag-CdSe, higher than typical nonepitaxially synthesized heterostructures. This demonstrated that epitaxially grown metal-SC heterostructures with large

lattice mismatches can be achieved with high QYs for plasmon induced hot electron transfer.

Besides the work detailed throughout this dissertation, there presents a multitude of related work that can still be done. While CO_2 reduction has been attempted with the ReC0A catalyst and Cd_3P_2 and CdSe, which is not described here, attempts to observe the reduced species of ReC0A to confirm the catalyst is ready for the reaction have not been successful because the catalyst's second reduction potential is more negative than the QD CB edge. However, our first study shows promise for being able to reduce CO_2 with Cd_3P_2 due to its exceedingly negative reduction potential in comparison to other QDs. A new catalyst would be needed with a more reasonable second reduction potential whereby the reaction can proceed. In addition, there is the potential of using Fano resonance coupling of a surface bound species to act as a probe of changes in the surface charge of a QD or other type of nanoparticle, which would be an interesting new direction for direct probing of changes in surface chemistry. We hope that this dissertation has highlighted the importance of nanoparticle surfaces in their chemistry and leads to a continued effort to understand the effect of QD surface chemistry on charge carrier behavior for their potential optimization in photovoltaics and photocatalysis.